UNIVERSITY OF OKLAHOMA

GRADUATE COLLEGE

EXPLORING TORNADO DEBRIS SIGNATURE HYPOTHESES USING

RADAR SIMULATIONS AND LARGE-EDDY SIMULATIONS

A THESIS

SUBMITTED TO THE GRADUATE FACULTY

in partial fulfillment of the requirements for the

Degree of

MASTER OF SCIENCE IN METEOROLOGY

By

RACHAEL N. CROSS
Norman, Oklahoma
2021

EXPLORING TORNADO DEBRIS SIGNATURE HYPOTHESES USING
RADAR SIMULATIONS AND LARGE-EDDY SIMULATIONS

A THESIS APPROVED FOR THE
SCHOOL OF METEOROLOGY

BY THE COMMITTEE CONSISTING OF

Dr. Robert D. Palmer, Chair

Dr. David J. Bodine

Dr. Phillip B. Chilson

Dedication

In loving memory of my Opa, who gave me my love of strawberry banana smoothies

and always brought a smile to my face.

Acknowledgments

Throughout my two years as a Masters student, there have been numerous people who have helped me along the way. First and foremost, a huge thank you to Dr. David Bodine, my advisor, for all of his feedback and helpful advice. Making the transition from social science research to radar wasn't easy for me, but his patience and guidance made it possible. It truly was a blast to work with him! Also, thank you to everyone in the NSF debris group: Dr. Boonleng Cheong, Dr. Robert Palmer, Dr. Caleb Fulton, Dr. Sebastián Torres, and Dr. Casey Griffin. Each one of you provided great comments and advice on my project, all of which were greatly appreciated and helpful. And of course, thank you to Dr. Robert Palmer and Dr. Phillip Chilson for taking the time to serve on my committee.

Another huge thank you goes to my friends and fellow co-workers, Emily and Morgan. Their encouragement helped me through the rough times, their amazing sense of humour constantly put a smile on my face, and their brilliance served as motivation to keep improving my own work. Thank you also to my two pups, Iza and Prince, for their constant distractions and reminders to sometimes take an afternoon nap. To my mom, dad, and sister, thank you always for your support and helping me achieve everything I set out to do. And finally, this work was made possible thanks to the support from the NSF through AGS-1823478.

Table of Contents

List Of Tables

List Of Figures

Abstract

Tornadoes can loft various types and sizes of debris, sometimes resulting in a polari-metric radar signature called the TDS (Tornado Debris Signature). The presence of a TDS in the radar data can help confirm the occurrence of a tornado, and provide information about the amount of damage occurring, making it a useful feature for operational forecasters. Past observational studies have suggested how the TDS evolves during a tornado's lifecycle, but few studies have related the polarimetric characteristics of a TDS to the tornado's wind field owing to the difficulty in obtaining three-dimensional wind data in tornadoes. This study aims to not only investigate the relationships between polarimetric weather radar variables in TDSs and the three-dimensional winds of tornadoes, but to also breakdown the relationship of the TDS debris size, type, and concentration.

A simulation-based framework is adopted since the tornado debris and wind characteristics are known, and thus these relationships proposed from observations can be explored in a more controlled manner. To accomplish this, simulations were performed using Large-Eddy Simulations of tornadoes and a dual-polarization radar simulator called SimRadar. Using SimRadar and a single-volume emulator, relationships between polarimetric variables and debris size, type, and concentrations are analyzed. Specifically, our study evaluates if reflectivity and correlation coefficient can provide information about debris size and concentration. Additionally, a dynamic, tornado-genesis simulation is used to allow for the analysis of the evolution of polarimetric variables in an intensifying tornado. Results from these simulations show how wind

characteristics of the simulated tornadoes, such as updraft intensity and area, magnitude of horizontal wind speeds, and vertical vorticity, are related to polarimetric variables. These findings can aid operational forecasters in tornado detection and potentially the categorization of damage severity using radar data.

Chapter 1

Introduction

Radar technology has made significant advancements since the genesis of the Weather Surveillance Radar 88 Doppler (WSR-88Ds) that are still critical to forecast operations to this day. In particular, the implementation of dual-polarization on the WSR-88Ds has proved significantly useful for precipitation estimation and severe hazard detection. Since dual-polarization radars transmit and receive pulses in both the vertical and the horizontal polarizations, this allows for the calculation of polarimetric variables such as differential reflectivity (Z_{DR}) — which is the ratio of the vertical polarization reflectivity over the horizontal polarization reflectivity — correlation coefficient (ρ_{hv}), and differential phase shift (ϕ_{DP}). These dual-polarization parameters highlight features such as the melting layer along with distinguishing diverse hydrometeor types, sizes, and shapes. In the context of severe weather, dual-polarization variables allow us to identify Z_{DR} arcs (Kumjian and Ryzhkov 2008), Z_{DR} columns, and the tornado debris signature (TDS; Ryzhkov et al. 2005), among other important features.

There have been numerous studies that have documented the TDS at various radar wavelengths using high-resolution, research radars and operational dual-polarization radars (e.g., Bluestein et al. 2007a; Kumjian and Ryzhkov 2008; Snyder et al. 2010; Snyder et al. 2013; Kumjian 2011; Palmer et al. 2011; Schultz et al. 2012a; Schultz

et al. 2012b; Tanamachi et al. 2012; Bodine et al. 2013; Griffin et al. 2017; Griffin et al. 2020). In Ryzhkov et al. (2005), the TDS was defined as a feature on radar with low Z_{DR} (< 0.5 dB), low ρ_{hv} (< 0.8), and a local maximum in Z_H (> 45 dBZ) which is co-located with a tornado vortex signature (TVS; Brown et al. 1978). They propose that the TDS can be used for remote tornado detection, and it has become an important component of operational warnings. Following Ryzhkov et al. (2005), studies have suggested that the Z_H threshold should be lowered to 20 dBZ or less to ensure TDS detection for lower amounts of debris (Van Den Broeke and Jauernic 2014; Griffin et al. 2020). Other ρ_{hv} thresholds have also been used when studying the TDS. For example, Bodine et al. (2013) used two thresholds ($\rho_{hv} < 0.82$ and $\rho_{hv} < 0.72$) which were based on precipitation effects on Z_{DR} and the 25th percentile of the lowest tilt data.

While the TDS can serve as real-time confirmation of the presence of a tornado, studies have shown that TDS characteristics such as TDS height, volume, and certain polarimetric statistics sometimes have a distinct relationship with the tornadic wind field. These relationships potentially expand the usefulness of the TDS from a confirmation tool to an aid in determining tornadic intensity from radar observations. For example, past observations have linked an increase in TDS width and height to an increase in tornado intensity or damage severity (Bodine et al. 2013; Van Den Broeke and Jauernic 2014; Kurdzo et al. 2015; Van Den Broeke 2015; Van Den Broeke 2017). Though, this is not always the case. In a study by Houser et al. (2017), the TDS width at low and mid-levels was more narrow when the tornado was at its strongest than during tornado dissipation. However, in this same case, TDS height and width

2

did increase at the onset of tornadogenesis, indicating that spatial TDS parameters can be correlated to an intensifying vortex, but can be complicated by debris fallout during tornado dissipation (Bodine et al. 2013). Because of this, the strongest relationship appears to be the relationship between TDS height and tornado intensity and damage severity (Van Den Broeke and Jauernic 2014; Van Den Broeke 2015).

Statistics of the polarimetric variables that define the TDS have also been shown to vary across tornadic intensity. An increase in 90th percentile Z_H and a decrease in ρ_{hv} and Z_{DR} correlate well with tornadic intensification while a decrease in 90th percentile Z_H correlates well with tornadic dissipation (Bodine et al. 2013). In a study of the Norman-Little Axe tornado (Griffin et al. 2020), it was found that, at all elevation angles, ρ_{hv} decreased and Z_H increased over time following tornadogenesis. Based on damage surveys, the tornado damage increased throughout the observation period, meaning the observed changes in polarimetric variables were likely due to the presence of more lofted debris (Griffin et al. 2020).

There are multiple different types, shapes, and sizes of debris that have been lofted by tornadoes, ranging from leaves to bricks to vehicles. It has been hypothesized that, as debris size increases, that Z_H increases and ρ_{hv} decreases (Bodine et al. 2014, 2016b). Likewise, it has also been hypothesized that, as debris concentration increases, Z_H increases and ρ_{hv} decreases as well (Dowell et al. 2005, Bodine et al. 2013). It might also be true that, at the onset of tornadogenesis, the distinction between debris types might be most obvious. This was hypothesized to be an explanation of heterogeneities in TDS height at the beginning of the tornado's life cycle in Houser et al. (2016).

3
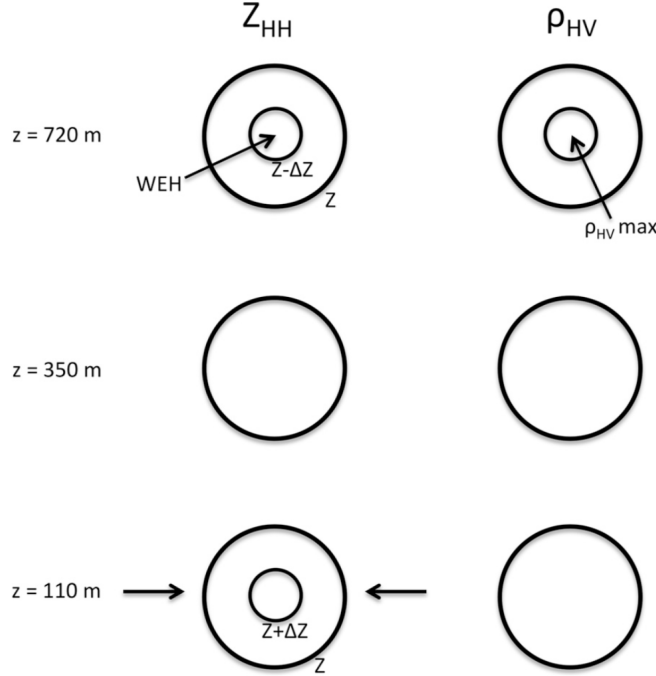
Figure 1.1: Schematic of the TDS as a function of height. Black arrows represent the inflow into the vortex. Near the surface, Z_H increases with range. At higher heights, Z_H is a WEH co-located with a maximum in ρ_{hv} that suggests a reduction in scatterer size at the center of the vortex (from Bodine et al. (2014).

A conceptual model of the TDS (Fig. 1.1) provided by Bodine et al. (2014) shows a weak echo hole (WEH; Dowell et al. 2005) in the Z_H values collocated with a maximum in ρ_{hv} at higher altitudes, likely due to a reduction in scatterer size. Dowell et al. (2005) also suggested that lofted debris and hydrometeors are centrifuged, resulting in a decrease in concentration in the center of the tornado, creating this WEH. Though, once light debris is lofted to higher levels in a tornadic storm, it takes some time (tens of minutes) for debris to sediment to the ground (Magsig and Snow 1998).

This smaller debris that is centrifuged can then be recycled back into the updraft and lofted (Bodine et al. 2013). Wakimoto et al. (2015) suggested that this smaller

debris can form what they called a "debris overhang" (Fig. 1.2). They defined this overhang as a region of $\rho_{hv} < 0.5$ that is co-located with a weak echo trench (a region of $Z_H < 35$ dBZ) and hypothesized that these features are associated with the storm's updraft. It has also been found that enhanced regions of Z_H in the TDS can be co-located with smaller, shear features within the broader circulation or the tornado (Wakimoto et al. 2016).

Centrifuging of debris can also affect the vertical structure and distribution of the TDS. A decrease in Z_H with height can be attributed to larger pieces of debris being centrifuged out from the center of the vortex (Bodine et al. 2014). It has also been found that ρ_{hv} decreases and Z_H increases with height throughout the tornado's life cycle in tandem with the tornado producing more damage (Griffin et al. 2020). However, over time the vertical profile of ρ_{hv} and Z_H of the TDS homogenized, perhaps due to the fact that large debris was finally lofted higher into the vortex or that debris fallout acted to homogenize the scatterer types in the tornado (Griffin et al. 2020).

Currently, forecasters use the TDS to make inferences about a tornado's intensity since real-time, accurate wind speed estimates are unavailable due to debris biasing the wind. Knowing how the polarimetric structure of the TDS evolves through a tornado's lifecycle is thus highly important as it is one of the few ways forecasters can obtain information about the tornado's intensity. Past studies have been able to relate TDS parameters to the tornadic wind field (e.g., Bodine et al. 2013), but looking at how specific debris types, sizes, and concentrations affect the polarimetric variables that define the TDS has not been explored in detail. Moreover, observational studies have largely speculated on these relationships owing to a lack of observational

information about the 3D distribution of debris characteristics and winds. To address these limitations, a polarimetric radar simulator is used to simulate tornadoes with varying types of debris and wind fields, enabling more concrete conclusions about these relationships through physically based modeling. These relationships are crucial because the tornado's 3D wind structure controls the 3D distribution of tornado debris (e.g., through lofting, centrifuging, and fallout), and the resulting 3D distribution of debris determines the polarimetric structure of the TDS. An improved understanding of debris characteristics can help scientists understand the 3D distribution of debris in tornadoes and will help forecasters identify a wide range of diverse TDSs encountered among different land surface types.

The goal of this study is thus twofold, exploring these interconnected relationships among the TDS, debris characteristics, and wind speeds as follows:

1. Determine how and if debris type, size, concentration, and orientation affects polarimetric variables in TDSs

2. Relate changes in polarimetric variables to changes in the tornadic wind field

Chapter 2 gives a background on the relevant polarimetric variables to this study along with a summary of basic tornado dynamics. Chapter 3 provides a detailed look into the methods used, while Chapters 4 and 5 contain the data and summary of the results of this project.
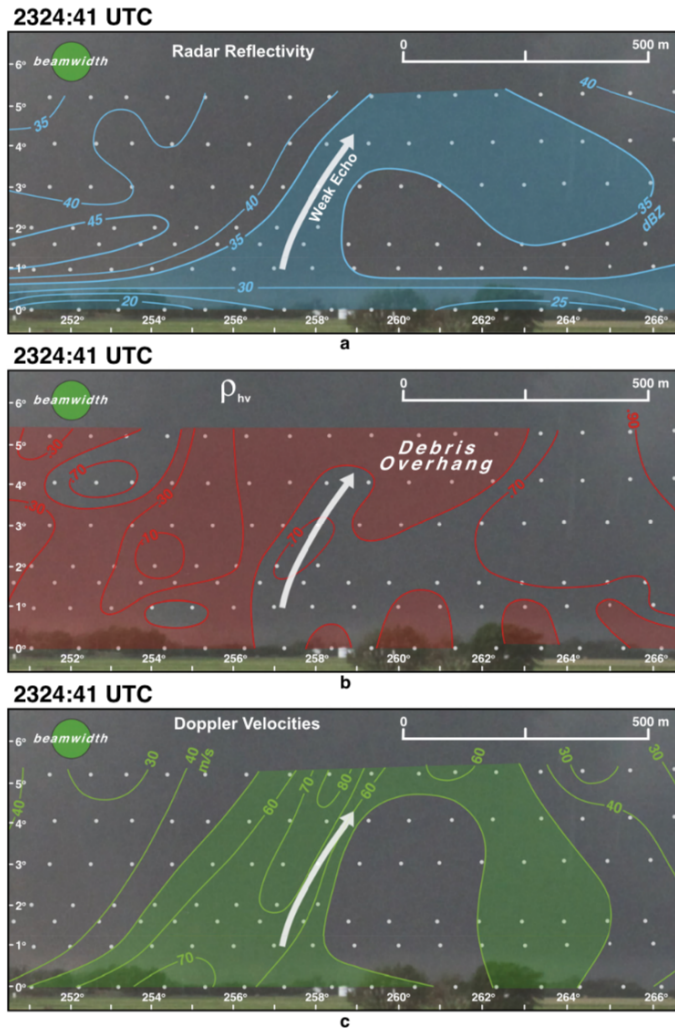
Figure 1.2: (a) Radar reflectivity (dBZ) with values < 35 dBZ shaded in blue, (b) correlation coefficient with values < 0.50 shaded in red, and (c) Doppler velocities (ms^{-1}) with values > 50 ms^{-1} shaded in green. White arrows represent the location of the weak-echo trench and the small dots represent raw data points from RaXPol (from Wakimoto et al. (2015)).

Chapter 2

Background

2.1 Dual-Polarimetric Variables

2.1.1 Reflectivity Factor

Radar reflectivity factor (Z_H) is a measure of range-corrected, returned power the radar receives and is mathematically given by:

$$Z = \int_0^\infty D^6 N(D) dD \tag{2.1}$$

where D is the diameter of the scatterer and $N(D)$ is the drop size distribution. From Equation 2.1, it is clear that Z_H is directly proportional to sixth power of the hydrometeor diameter and the concentration of scatterers in a unit volume. Values of Z_H will also depend on hydrometeor phase or the composition of the scatterer. However, Z_H is often displayed on a logarithmic scale with units of decibels of Z (dBZ):

$$\text{dBZ} = 10 log_{10} \left(\frac{Z}{1\,\text{mm}^6\,\text{m}^{-3}} \right) \tag{2.2}$$

Since Z_H is related to the returned power, it is affected by attenuation, which is the amount of transmitted electromagnetic energy lost due to scattering and absorption. Attenuation effects accumulate with range and are thus more prevalent at far
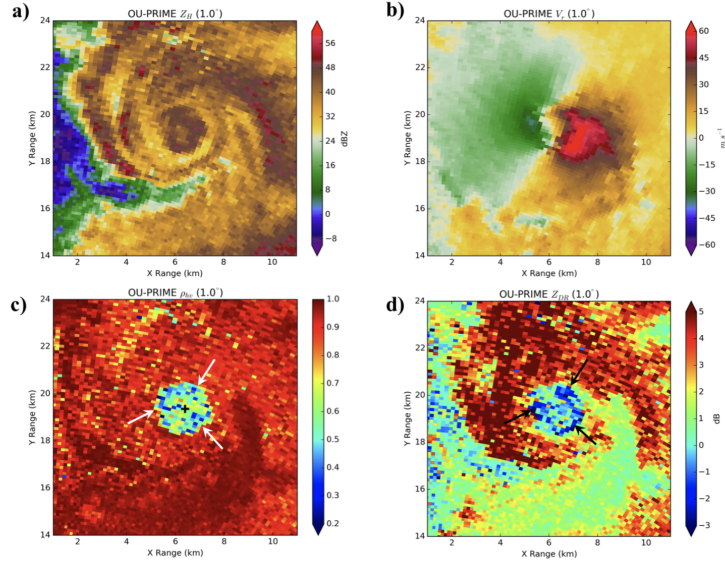
Figure 2.1: PPIs of a TDS from OU-PRIME (a) reflectivity (dBZ), (b) radial velocity (ms⁻¹), (c) correlation coefficient, and (d) differential reflectivity (dB) as seen in Griffin et al. (2017).

distances from the radar, especially down range from areas with a high concentration of scatterers. The effects of attenuation are reduced in radars with longer wavelengths (e.g., S-band) in contrast to shorter wavelengths (e.g., X-band).

In addition to providing information about scatterer size and concentration, Z_H can also be used to estimate rainfall rates if the number distribution of targets is known. Values of reflectivity are weighted towards the largest scatterers within a given unit volume. Thus, in a volume with small and large raindrops, the larger drops will dominate the return signal. This is also true for large, non-meteorological scatterers as well, such as debris. Larger debris (e.g., woodboards) will especially dominate the signal, sometimes creating a ring of high Z_H that is indicative of centrifuged debris (Dowell et al. 2005; Bodine et al. 2014) or a region of high Z_H that is associated with

the TDS (Ryzhkov et al. 2005). An example of this is shown in Fig. 2.1a where it can be seen that the location of the TDS is co-located with a region of higher Z_H values.

2.1.2 Differential Reflectivity

Differential reflectivity (Z_{DR}) is the the ratio of horizontal and vertical radar reflectivity factors, given by.

$$Z_{DR} = 10log_{10}\left(\frac{Z_H}{Z_V}\right) \tag{2.3}$$

A scatterers' aspect ratio contributes significantly to its Z_{DR} value. Positive values of Z_{DR} indicate that the scatterer is longer in the horizontal while negative value of Z_{DR} indicate the scatterer is longer in the vertical. Values near zero mean the target is spherical, or it is tumbling (e.g., randomly oriented) and returns equal power in the horizontal and vertical. Debris can have Z_{DR} values near zero, though negative Z_{DR} values can also be associated with debris due to Mie scattering or common debris alignment (e.g., Ryzhkov et al. 2005; Bluestein et al. 2007b; Bodine et al. 2011; Bodine et al. 2013; Wakimoto et al. 2018; Umeyama et al. 2018). In tornadoes, it has been shown by Umeyama et al. (2018) that debris do exhibit some common alignment which explains the negative Z_{DR} signatures seen in tornadoes. Fig. 2.1d shows near zero values of Z_{DR} in the TDS with regions where Z_{DR} is negative. Hail also commonly has values of Z_{DR} near zero, though how much liquid water is present on the hailstone will cause Z_{DR} to vary. The liquid water can reduce the amount of tumbling, thus causing the hailstone to have positive values of Z_{DR} (Kumjian 2013).

As for rain, larger drops are oblate, meaning they have higher, positive values of Z_{DR}. Regions with a high concentration of drops typically have more large drops, meaning Z_{DR} will often increase with values of Z_H in the presence of heavy rain. The exception to this is when size sorting occurs, which creates areas with a small concentration of large drops. This often occurs on the periphery of updrafts and along the leading edge of storms (Kumjian 2013). Because Z_{DR} is a ratio of the horizontal and vertical polarizations, it is independent of the concentration of targets and is not affected by the miscalibration of a radar's transmitter or receiver. Anisotropic scattering, which is the nonuniform scattering of electromagnetic waves, can bias values of Z_{DR} depending on which polarization is being muted (Kumjian 2013).

2.1.3   Correlation Coefficient

Correlation coefficient (ρ_{hv}) is the correlation between the horizontal and vertical received signals. Mathematically, it is represented by:

$$\rho_{hv} = \frac{\left| \int_{D_{min}}^{D_{max}} S_v(\pi, D) S_h^*(\pi, D) N(D) dD \right|}{\sqrt{\int_{D_{min}}^{D_{max}} |S_v(\pi, D)|^2 N(D) dD \int_{D_{min}}^{D_{max}} |S_h(\pi, D)|^2 N(D) dD}}, \qquad (2.4)$$

where S_h and S_v are the horizontal and vertical scattering amplitudes and D_{max} and D_{min} are the maximum and minimum diameters.

Since ρ_{hv} is a measure of the diversity of the physical characteristics of scatterers, the more diverse the field of targets is, the lower ρ_{hv} will be while a perfectly uniform field of targets will produce a ρ_{hv} value of one. Factors that contribute to the diversity of scatterers are the shape and orientation of targets along with the target's physical

composition. All these factors will change the amplitude of the scattered energy in the horizontal and vertical, and will thus effect the resulting ρ_{hv} value. Non-uniform beam filling, which is often caused by the broadening of the beam with distance from the radar picking up on multiple scatterer types, can act to reduce ρ_{hv}. Values of ρ_{hv} are not affected by attenuation, radar miscalibration, or differential attenuation.

In reality, ρ_{hv} is rarely exactly one due to the movement and wobbling of scatterers. For rain, ρ_{hv} will change across drop size as the shape varies across size while wet hail often produces values less than 0.95 (Kumjian 2013). Larger hail can have even lower ρ_{hv} values due to having an irregular shape created from wet growth. This makes ρ_{hv} a useful tool in distinguishing between storms with purely rain and a mixture of rain and hail. Melting snowflakes reduce ρ_{hv} by enhancing the variation in scatterer shape. This combined with the possible Mie scattering effects from melting snow reduce ρ_{hv}, enabling detection of the melting layer.

Since ρ_{hv} is sensitive to scatterer shape, debris typically has extremely low values of ρ_{hv}, otherwise known as the TDS (Fig. 2.1c). In addition, the large sizes of debris introduce non-Rayleigh scattering which also reduces ρ_{hv}. Another ρ_{hv} signature seen in severe storms is the ρ_{hv} ring, noted by Payne et al. (2010) and Kumjian and Ryzhkov (2008). This signature is associated with the vorticity maximum of a mesocyclone and is indicative of mixed phase or non-Rayleigh scatterers near the updraft. It is also thought that the ρ_{hv} ring could be attributed to size sorting from the circulation of the mesocyclone.
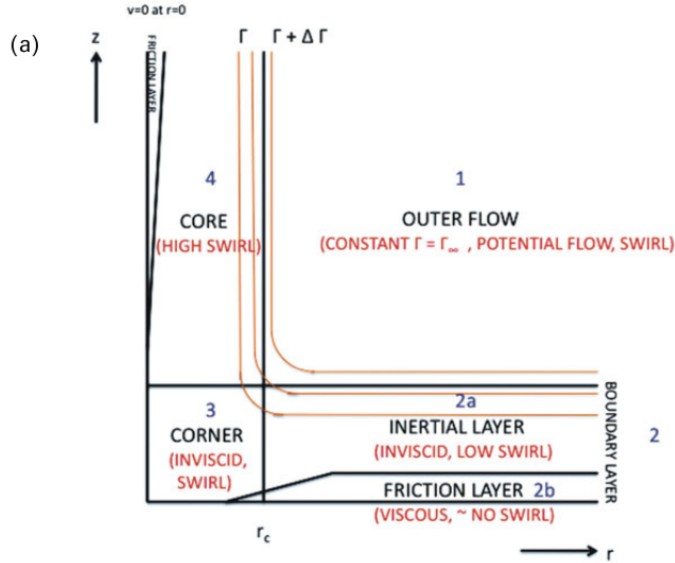
Figure 2.2: Vertical cross section of the four regions of a tornado (from Bluestein (2013)).

2.2 Tornado Dynamics

The structure of tornadoes is usually broken down into five regions: the outer region, the core region, the corner flow region, the boundary layer flow, and the rotating updraft (Fig. 2.2). The outer region is characterized by cyclostrophic balance, which is the balance of the pressure gradient force and the centrifugal force. In this region, the pressure gradient force drives the flow in the boundary layer below (Bluestein 2013). Finally, the outer region is characterized by constant angular momentum, similar to that of a potential vortex.

In the boundary layer of the tornado, the flow departs from cyclostrophic balance due to surface drag, resulting in a reduction in azimuthal velocities. The gradients in centrifugal force in this region result in a radial inflow near the bottom of the vortex (Lewellen 1976). The boundary layer flow can be split into two parts: the inertial

and the friction layer. In the friction layer, the pressure gradient force acts radially inward while friction acts to slow the flow. This results in acceleration that is directed away from the center of the vortex. The effects of surface friction from the friction layer are transported vertically to the inertial layer. In this layer, parcels become less-cyclostrophic with height as the effects of the vertically transported friction are lessened.

In the corner region, parcels continue to decelerate until they converge at the center of the vortex. From mass continuity, this means there must be strong vertical motion at the point of convergence. This vertical turning of the wind at the base of the tornado is called the secondary circulation. Vertical and radial variations in the flow are significant in this region along with very strong wind magnitudes. It is this region of the tornado that is most responsible for lofting debris. With this in mind, it might come as a surprise that the corner flow is assumed to be inviscid. Finally, the core of the tornado extends from the origin of rotation to the radius of maximum wind. This region is visually associated with the condensation funnel and is approximately in cyclostrophic balance. Thus, the core flow is centrifugally stable, indicating small radial displacement and little to no entrainment into the core of the vortex. It is often assumed that the core region is axisymmetric and the simplest solution of the angular momentum equation for this region is the Rankine vortex (Rankine and Miller 1888).

2.2.1 Swirl Ratio

There are many different definitions of the swirl ratio. In laboratory studies (e.g. Rotunno 1979), the swirl ratio is defined by:

$$S = \frac{R\Gamma}{2M} \tag{2.5}$$

where R is the radius of the updraft hole, Γ is the circulation at the edge of the updraft, and M is the volume flow rate of the updraft. Most commonly, the swirl ratio is defined as the ratio of the azimuthal velocity to the updraft velocity (Eq. 2.6).

$$S = \frac{v_0}{w} \tag{2.6}$$

For chamber studies, if the depth of the inflow layer is double that of the updraft hole, then the swirl ratio can then become:

$$S = \frac{v_0}{u_0} \tag{2.7}$$

where v_0 is the azimuthal velocity at the periphery of the circulation and u_0 is the radial inflow into the bottom of the tornado. Lewellen et al. (2000) defined a corner flow swirl ratio (Eq. 2.8):

$$S_c = \frac{\Gamma^* r^*}{M^*} \tag{2.8}$$

where Γ^* is the angular momentum, r^* is the radius of the upper-core, and M^* is the mass flux.

For extremely low swirl ratios, the acceleration is positive, meaning it is directed towards the center of the vortex. The pressure gradient force, however, acts in the opposing direction. This opposing force strengthens as the flow approaches the center of the tornado until the inflow is forced upwards at large radial distances from the vortex. This results in no convergence of angular momentum and thus no tornado. In a vortex chamber study by Rotunno (1979), the radial inflow was connected with boundary layer separation at low swirl ratios. It was this boundary layer separation that prevented a strong vortex from forming at the center of the domain. Looking at S_c, it was found that, at excessively low values of S_c, vortex intensification is minimal and occurs off the surface (Lewellen et al. 2000). Thus, the intensity and dynamics of the radial inflow largely determines whether or not a circulation evolves into a tornado (Lewellen et al. 2000).

For low or intermediate swirl ratios, the boundary layer remains attached, creating a radial acceleration directed towards the center of the vortex (Rotunno 1979). The radial wind is thus greater in magnitude than the tangential wind. The pressure gradient force still acts radially outward, but the radial distance at which the parcels turn upwards decreases and results in more intense tangential winds. This results in a one-cell vortex. Finally, when the swirl ratio is large, the tangential wind is greater in magnitude than the radial wind. In this case, the pressure gradient force is directed to the center of the vortex. In fact, the pressure in the center of the vortex can drop significantly enough to induce a central downdraft. At earlier stages, the downdraft may not reach the surface. The location where the updraft and central downdraft meet is called a vortex breakdown. With further increases in swirl ratio,

the downdraft impinges upon the surface resulting in a two-cell vortex. As the swirl ratio increases, multiple vortices can form as well. However, it was found by Lewellen et al. (2000) that too high corner flow swirl ratios can hinder near-surface velocities from reaching tornadic intensities.

Chapter 3

Methods

3.1   Single Volume Emulator

To provide a more constrained environment to detail relationships between polarimetric variables and debris concentration, type, and size, a single volume emulator was developed using equations as seen in Bukovcic et al. (2017). Radar reflectivity, differential reflectivity, and correlation coefficient are given in Eq. 3.1, 2.2, 3.2, and 2.4 respectively.

$$Z_{h,v} = \frac{4\lambda^4}{\pi^4 |K_w|^2} \int_{D_{min}}^{D_{max}} |S_{h,v}(\pi, D)|^2 N(D)dD. \tag{3.1}$$

$$Z_{DR} = 10log_{10}(\frac{Z_h}{Z_v}) \tag{3.2}$$

The emulator was set up to use a wavelength of 0.1 m to try and simulate an S-band radar with a volume size of 10^6 m^2. Scattering amplitudes for three different debris types – woodboards, rocks, and leaves – were obtained using T-matrix calculations (Mischenko et al. 1996; Mischenko 2000). The diameter ranges, axis ratios, dielectric constant values can be found in Table 3.1. The dielectric constant value for rocks was obtained from Ulaby et al. (1988) and the values for leaves were obtained from Senior et al. (1987). In addition to selecting different axis ratios for the leaves (Table

3.1), three different saturation percentages were used: 0% (dry leaves), 22% (leaves), and 100% (saturated leaves).

Table 3.1: Table of dielectric constant values for each debris type along with the respective axis ratios used in the T-matrix calculations

Debris Type	Dielectric Constant	Axis Ratio
Woodboards	1.416 + 0.0706i	0.33
Rocks	3.000 + 0.0300i	0.5
Saturated Leaves	32.75 + 40.90i	0.1
Leaves	23.39 + 23.12i	0.1, 0.25, 0.5
Dry Leaves	15.63 + 11.82i	0.1

It should be noted that the scattering amplitudes obtained using the T-matrix method assume the debris as some variation of a spheroid. The scattering amplitudes from the T-matrix method are thus a proxy of the scattering amplitudes of real debris which have more diverse and complex shapes. The T-matrix method was chosen for the single volume emulator over the more accurate High Frequency Structure Simulator (HFSS) data because the T-matrix method allows for the much faster calculation of the scattering amplitudes for a wide variety of debris sizes, allowing for easy comparison of large and small debris. For example, a single piece of realistic debris can take a day to complete with HFSS whereas these calculations run in seconds for T-matrix, thus allowing a much wider range of parameters to be examined.

Each debris type had 1296 different orientations. Different orientations are created by rotating spheroids first from the $+z$ axis and then around the $+y$ axis. Angles are varied in 5° increments to capture angle-dependent scattering effects. For each experiment run with the single volume emulator, the orientation of each piece of debris

was randomly selected. To account for debris concentrations above 1000, orientations were still randomly selected but the scattering amplitudes were multiplied by some factor of ten to obtain concentrations of 10000, 1000000, and so on.

3.2 Large-Eddy Simulations

Three different LES cases were analyzed in this project: a tornadogenesis case, a stronger tornadogenesis case, made stronger by a more intense updraft, and a strong tornado dissipation case. Each LES case is defined by a shallow inflow region and a selected value for angular momentum and updraft speed. Modification of the LES for simulations of tornados is outlined in Maruyama (2011) and Bodine et al. (2016a). The LES model used in this project is a stretched grid with horizontal spacing that varies from 2.6 to 16.8 m out from the center of the domain and vertical resolutions that vary from 2.7 to 98 m. The stretched grid allows for finer resolution near the surface and center of the vortex so that fine-scale features such as subvorticies might be resolved. In SimRadar, a subset of the model grid is used for computational efficiency. The full domain is 2 km x 2 km x 1.5 km in the x, y, and z directions while the included grid points in the x, y, and z dimension are 195, 195, and 99, respectively. The model output time interval is 1.2755 s.

The domain bounded by three different boundary conditions (BCs): the lower, upper, and horizontal BCs. The horizontal BCs approximately create an axisymmetric flow in the inflow region, which in the tornadogenesis (dissipation) simulations begins (ends) with a depth of approximately 500 m and ends (begins) with a depth

between 200 m - 300 m. A logarithmic flow is imposed on the horizontal BCs with a roughness length Z_0 of 0.1 m. On the lower BC, the flow is defined by a logarithmic wind profile (Eq. 3.3), where u^* is the friction velocity, k is Von Karman's constant, and V_h is the horizontal wind speed. The surface stress is then calculated using Eq. 3.4 and then split into its x and y components.

$$u_* = \frac{V_h z_1 k}{log(\frac{z_1}{z_0})}$$ (3.3)

$$\tau = \rho u_*{}^2$$ (3.4)

Above the inflow region, velocities are 0 ms^{-1} and the angular momentum is kept constant. Finally, the top BCs vary across the simulations used in this study. The mean updraft produced along the top BC and the mean angular momentum at a radius of 470 m change throughout the simulations. The starting values for these parameters for each simulation are given in Table 3.2.

Table 3.2: Initial boundary conditions for each simulation. The mean updraft is taken from the top of the simulation domain while the mean angular momentum is taken at a radius of 470 m.

LES Simulation	Mean Updraft (ms^{-1})	Mean Angular Momentum $(m^2 s^{-1})$
Tornadogenesis	15.00	2.0981×10^3
Strong Tornadogenesis	16.19	1.6093×10^3
Strong Dissipation	22.35	1.6308×10^4

Debris trajectories in the LES model are calculated using a Lagrangian approach which is mathematically given by:

$$\frac{du_{di,n}}{dt} = \frac{1}{2} \frac{\rho C_D A_n}{m_n} (u_i - u_{di,n}) |u_i - u_{di,n}| - g\delta_{i,3}, \qquad (3.5)$$

where C_D is the drag force coefficient, A_n is the debris area, ρ is the density of air, m_n is the debris mass, g is the gravitational acceleration, and u_i and $u_{di,n}$ are the air and debris velocities where $i = 1$, 2, and 3 represent the x, y, and z directions. Debris are assumed to be approximately spherical in each simulation, meaning they have isotropic drag coefficients. The drag coefficient, C_D is calculated using a formula from White (1991) and is given by:

$$C_D \approx \frac{24}{Re_p} + \frac{6}{1 + \sqrt{Re_p}} + 0.4, \qquad (3.6)$$

where Re_p is the particle Reynolds number. This number accounts for the variation in the drag coefficient for spherical scatterers and is given by:

$$Re_p = \frac{\rho d_n |u_i - u_{di,n}|}{\mu}. \qquad (3.7)$$

Trajectories for n debris are calculated using Eq. 3.5, 3.6, and 3.7 though the total number of trajectories computed throughout the simulation is limited to 10^6.
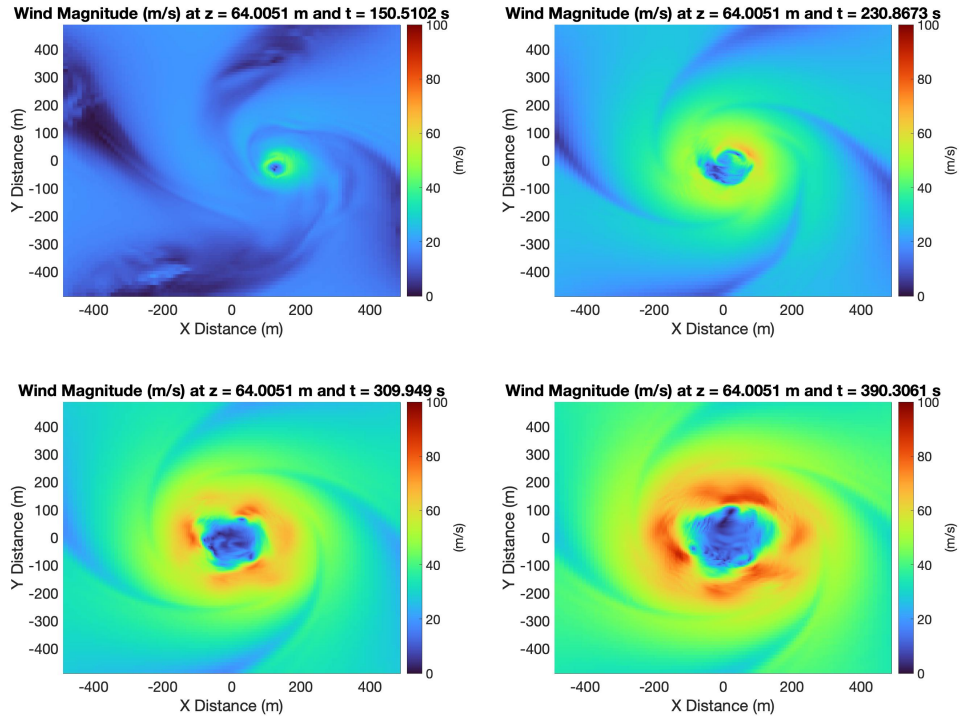
Figure 3.1: Plots of the horizontal wind magnitude for the weaker tornadogenesis simulation at a height of 64 m from the bottom of the simulation domain. Values of the wind speed are given in ms^{-1} for four times: a) 150 s, b) 230 s, c) 309 s, and d) 390 s.

3.2.1 Tornadogenesis Simulation

For the tornadogenesis case, the vortex meanders about the origin of the domain during the beginning of the simulation before a central downdraft is induced (Fig. 3.1). The tornado then experiences vortex breakdown and separates into four smaller vortices. As the simulation progresses, the downdraft widens and the strength of the wind magnitude increases. The length of this simulation is 408.16 s.
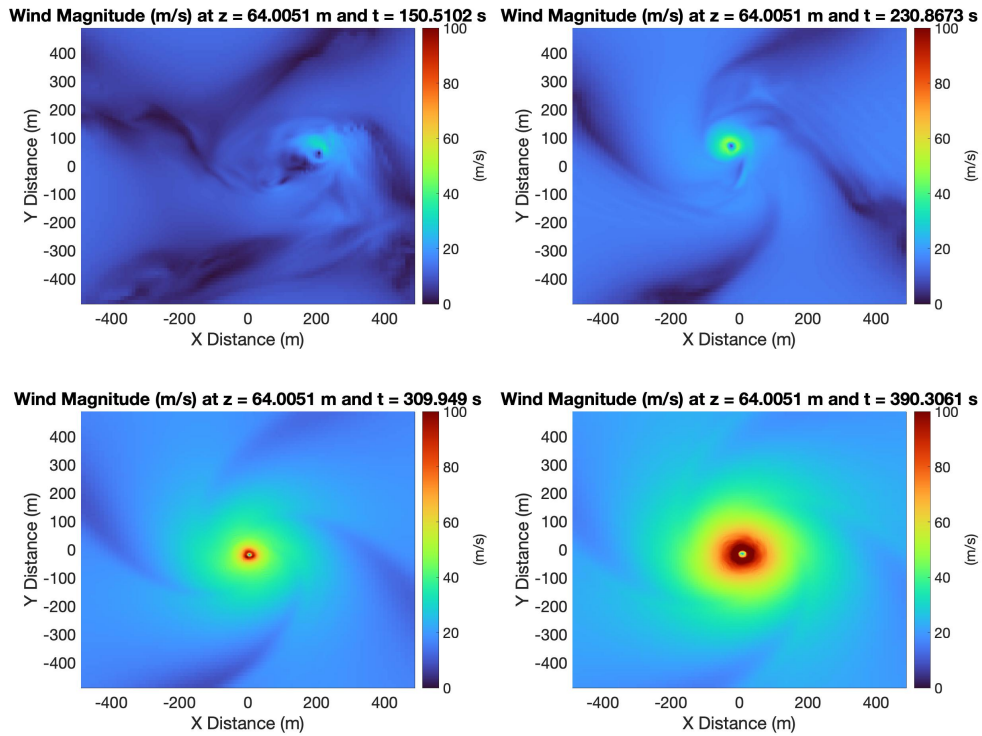
Figure 3.2: Same as in Fig. 3.1, but for the stronger tornadogenesis simulation.

3.2.2 Strong Tornadogenesis Simulation

In the stronger tornadogenesis simulation, the tornado also meanders about the origin of the domain much like in the tornadogenesis simulation. However, unlike before, this tornado does not breakdown into multiple vorticies as the simulation progresses (Fig. 3.2). Instead, the tornado remains a single cell vortex with a central downdraft as it intensifies. The wind magnitude also reaches values above 100 ms^{-1} and the length if the simulation is 408.16 s.
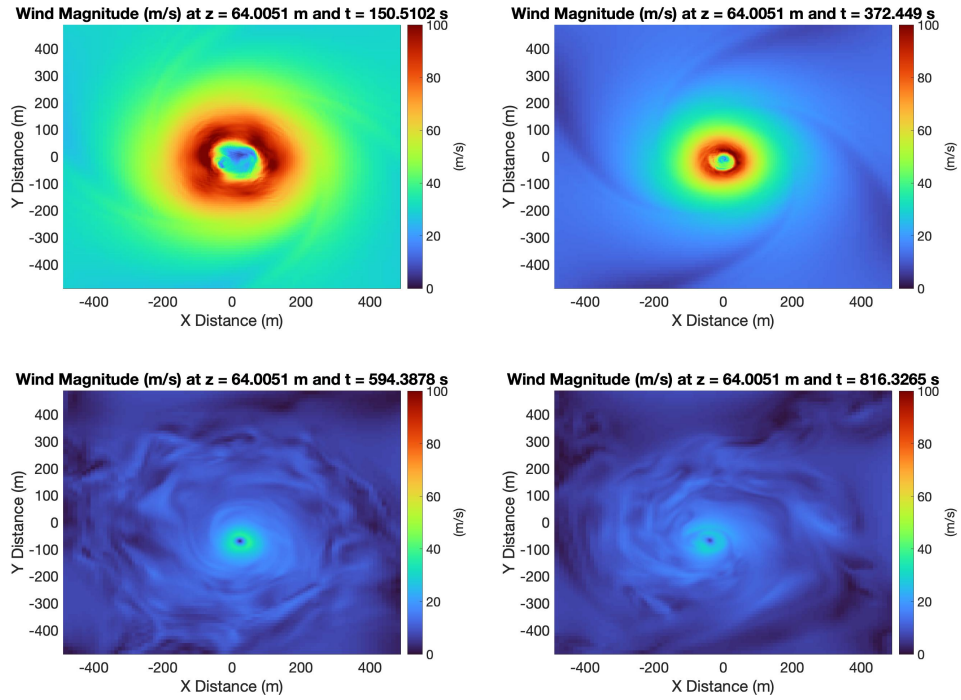
Figure 3.3: Same as in Fig. 3.1, but for the dissipation simulation.

3.2.3 Tornado Dissipation Simulation

The simulation begins with a strong vortex with a central downdraft (Fig. 3.3). As the simulation progresses, the vortex narrows and weakens. The tornado remains near the origin of the domain until the end of its lifecycle when it begins to cycle about the origin of the domain. The length of this simulation is 816.32 s, which is twice the length of the two tornadogenesis simulations. Even though the dissipation case takes longer to run, the rate of change of the BCs during the first half of the simulation is the same in the dissipation simulation as in the tornadogenesis simulations. During the second half of the simulation, the BCs remain constant and are the same as the initial conditions as the tornadogenesis simulations.

3.3 SimRadar

To analyze the relationship between the dynamic tornado-scale winds and the polari-
metric variables, SimRadar – a S-band, dual-polarization radar simulator developed
by Cheong et al. (2017) – was used. This radar simulator combines LES model data,
six degree-of-freedom model (6DOF) debris trajectories, and scattering data, provid-
ing an efficient way to relate polarimetric radar data to LES wind field parameters as
well as debris characteristics. More details about the SimRadar platform and debris
trajectory calculations can be found in Cheong et al. (2017) and Umeyama et al.
(2018). Unlike with the single volume emulator, the radar cross section (RCS) of
debris was calculated outside the simulation using HFSS data which capture electro-
magnetic effects from more complex shapes (Lujan 2016). In addition, 6DOF debris
trajectories provide realistic motions and orientations needed to calculate polarimet-
ric variables. These combined capabilities of realistic tornado winds, debris motions,
and electromagnetic scattering create a simulation tool for exploring more complex
TDS relationships where the true parameters are known in contrast to observations
where debris and 3D wind data are scarce. The three debris types used in this part of
the study are 2×4 woodboards, leaves, and metal sheets. The dimensions and details
about each debris type can be found in Table 3.3.

SimRadar emulates volume scattering by calculating the coherent summation of
backscattered signals from numerous point scatterers. This coherent summation of
targets is similar to the *Monte Carlo* method and, when there is a sufficient number of

Table 3.3: List of scatterer type, dimensions, and density for each debris type used in this study.

Debris Parameters	
Scatterer Type	Leaf
Dimensions (body)	0.1 cm × 8 cm × 6 cm
Dimensions (stem)	12 cm long
Density	350 kgm^{-3}
Scatterer Type	Woodboard
Dimensions	2 in × 12 in × 4 in
Density	500 kgm^{-3}
Scatterer Type	Metal Sheet
Dimensions	0.1 cm × 100 cm × 100 cm
Density	350 kgm^{-3}

these point scatterers, the summation of backscattered signals represents the return signal. Mathematically, the integration is given by:

$$x[n] = \sum_{i=1}^{N} A^{(i)} \exp\left(-j\frac{4\pi r^{(i)}}{\lambda}\right), \tag{3.8}$$

where $r^{(i)}$ is the range, λ is the wavelength, N is the number of point targets in the volume, and $A^{(i)}$ is the amplitude of the backscattered signal for i^{th} point target. The amplitude includes the effects of range-weighting and the antenna pattern and is given by:

$$A^{(i)} = \left(\frac{1}{r^{(i)}}\right)^4 Z^{(i)} W_a^{(i)} W_r^{(i)}, \tag{3.9}$$

where $r^{(i)}$ once again represents the range of the scatterer, $W_a^{(i)}$ is the weighting of the antenna pattern, $W_r^{(i)}$ is the weighting of the range-weighting function, and $Z^{(i)}$ is the scatterer's intrinsic reflectivity.

A visual summary of the process SimRadar goes through to obtain a radar sample is given in Fig. 3.4. After obtaining the scattering amplitudes from the RCS data,

Position : x, y, z
Velocity : u, v, w
Orientation : q_w, q_x, q_y, q_z
RCS : $S_{HH}, S_{HV}, S_{VH}, S_{VV}$

RCS Lookup & Projection $\quad\Leftarrow\quad \begin{bmatrix} S_{HH} & S_{HV} \\ S_{VH} & S_{VV} \end{bmatrix}$

Antenna Pattern Lookup $\quad\Leftarrow\quad W_a^{(i)}$

Range Pattern Lookup $\quad\Leftarrow\quad W_r^{(i)}$

$$x[n] = \sum_{i=0}^{N} A^{(i)} \exp(-j\frac{4\pi r^{(i)}}{\lambda}) \quad\Rightarrow\quad \text{I/Q sample}$$

Trajectory Calculation $\quad\Leftarrow\quad (u, v, w)^{(i)}$

Position Update
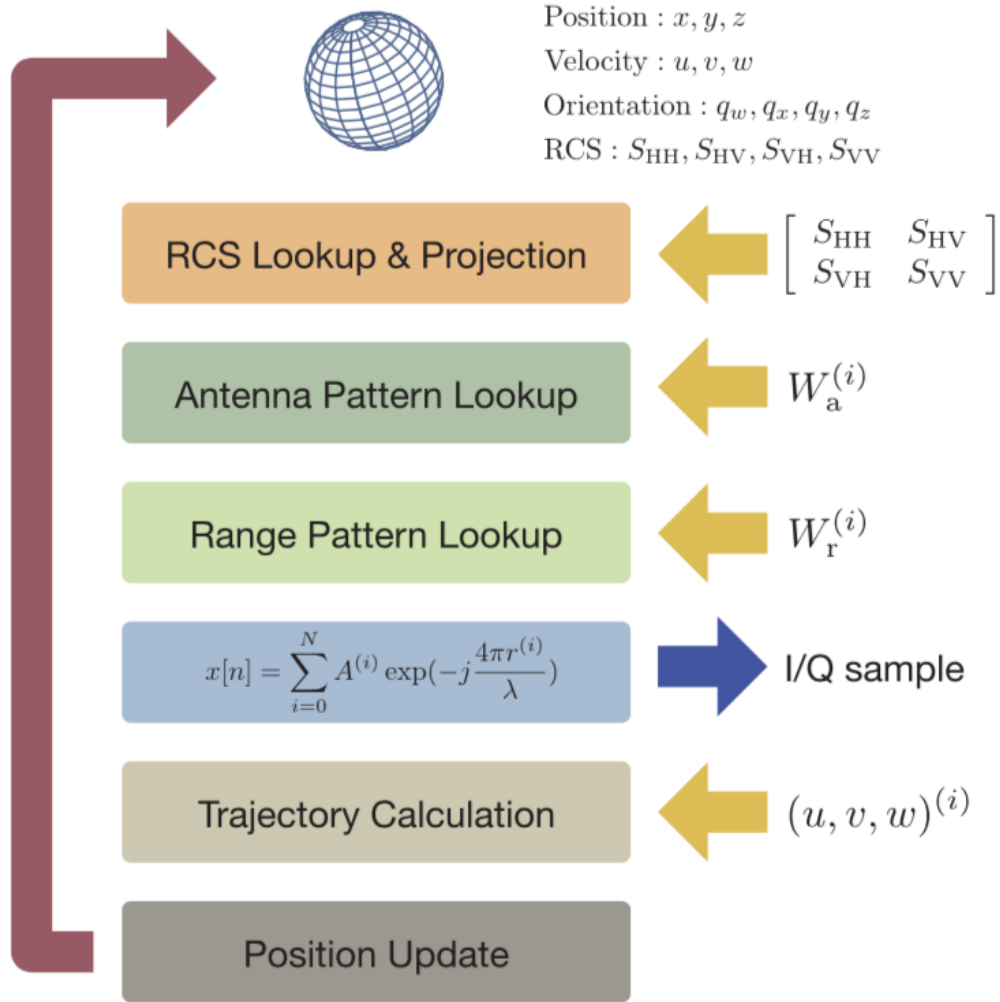
Figure 3.4: Flowchart of SimRadar from Cheong et al. (2017).

the antenna pattern, and the range pattern, the return signal (i.e. the I/Q sample) is calculated using Eqs. 3.8 and 3.9. Finally, the velocities of each point target are updated based on the scatterer's newly calculated trajectory.

For the simulations used in this study, a beam width of 1° and a pulse repetition time of 0.0005 s was used. Using the equation for range ambiguity (Eq. 3.10), range

Table 3.4: SimRadar parameters used for each simulation in this study.

Radar Parameters	
PRT	0.5 ms
Wavelength	10 cm
Peak Transmit Power	50 kW
Transmit Pulse Width	0.2 μs
Antenna Gain	50 dBi
Antenna Beamwidth	1.0°
Range Resolution	75 m
Gate Spacing	15 m
Samples per Dwell	100
Azimuthal Sampling	0.5°
Max Unambiguous Velocity	50 ms^{-1}

aliasing occurs at distances at or greater than 75 km. Velocity aliasing (Eq. 3.11) occurs at $\pm$ 50 ms^{-1}.

$$r \geq \frac{c}{2 \times PRF} \tag{3.10}$$

$$V_{max} = \frac{PRF \times \lambda}{4} \tag{3.11}$$

A comprehensive list of the radar parameters used for the simulations in this study is given in Table 3.4.

The lowest elevation angle analyzed was 2.5°, which corresponds to a height of 88.9 m from the bottom of the domain. Elevation angles were increased by 0.5° increments up to 9.0°, which is 318.2 m from the bottom of the domain. In most of the simulations run for this project, debris never exceeded the 318.2 m level, making this selection of elevation angles adequate for the sake of this study. This exception to this is the stronger tornadogenesis simulation. The vertical evolution of the TDS in this simulation will be discussed more in Chapter 5.

3.3.1   TDS Area Calculation

The TDS was defined by $\rho_{hv} < 0.95$ and points within a 200 m radius from the center of the vortex. Such a high threshold for ρ_{hv} was used because it was found that, for certain debris types, ρ_{hv} exceeded the 0.8 threshold used by Ryzhkov et al. (2005). Past observational studies speculated that this is in areas of light debris, such as leaves (Griffin et al. 2020). For the sake of consistency, the same ρ_{hv} threshold was used for all debris types to easily compare TDS area values. A semi-objective method is used to identify the vortex center. The center of the vortex was defined as the point of minimum pressure perturbation from the LES model. The exception was when the vortex was centered at the origin of the domain, during which the origin was used as the central point. This method was applied subjectively at the later times in the tornadogenesis case when the tornado split into multiple vortices and the minimum pressure perturbation no longer identified the vortex center. However, the tornado's center was subjectively determined to be the center of the domain.

Chapter 4

Polarimetric Variables vs. Debris Characteristics

In this chapter, the relationships between polarimetric variables (primarily Z_H and ρ_{hv}) and debris concentration, size, and orientation will be explored. Previously, these relationships have primarily been speculated in past work as it is nearly impossible to grasp the amount of debris present in observations. The use of simulations to confirm these speculations is thus imperative. That being said, the results outlined in this chapter are from a single volume emulator that uses electromagnetic scattering calculations for debris.

4.1 Effect of Debris Size

It has been hypothesized that, as debris size increases, ρ_{hv} will decrease and Z_H will increase (Bodine et al. (2014); Bodine et al. (2016b); Ryzhkov et al. (2005)). To test this theory, the single volume simulator was used to find Z_H and ρ_{hv} for each debris type. For this analysis, 100 experiments were run for each debris type. The polarimetric variables were then averaged across experiments, resulting in one value for each debris size. In this case, the size of the debris is changed by increasing or decreasing the equivalent volume diameter of the simulated object. A concentration of 100 pieces of debris per resolution volume was chosen for each debris type.

How ρ_{hv} and Z_H change with increasing debris size for each debris type is shown in Fig. 4.1. For woodboards, as debris size increases, ρ_{hv} generally decreases and Z_H increases (Fig. 4.1a and 4.1b). The relationship between these two parameters and debris size is approximately linear, though there is more variance in the ρ_{hv} values.

While the relationships between ρ_{hv}, Z_H, and debris size for woodboards confirm past hypotheses, the other debris types tell a different story. For increasing diameter for rocks, ρ_{hv} oscillates between values near 0.1 and 1 (Fig. 4.1c). The exception is the semi-consistent trend of ρ_{hv} up to a diameter of 22 mm that is followed by a sharp decrease in ρ_{hv} values. In this same range, Z_H increase (Fig. 4.1d). Near where ρ_{hv} decreases, Z_H begins to oscillate. It is likely that this represents a transition from the Rayleigh to the Mie Regime and the oscillations in Z_H are a result of resonance effects.

For a leaf with an axis ratio of 0.1 and a saturation of 22%, ρ_{hv} generally decreases with increasing debris size (Fig. 4.1e). At a diameter of about 10 mm, however, ρ_{hv} increases slightly. Overall, the ρ_{hv} values for the leaves do not change as drastically as the other two debris types as the values range from near 0.7 for the smallest debris and near 0.54 for the largest debris. The reflectivity values Z_H increase linearly with increasing debris size. It is likely the tapering off of Z_H as seen with the woodboards does not occur with the leaves as the rage of debris sizes is much smaller than the range of sizes of woodboards.
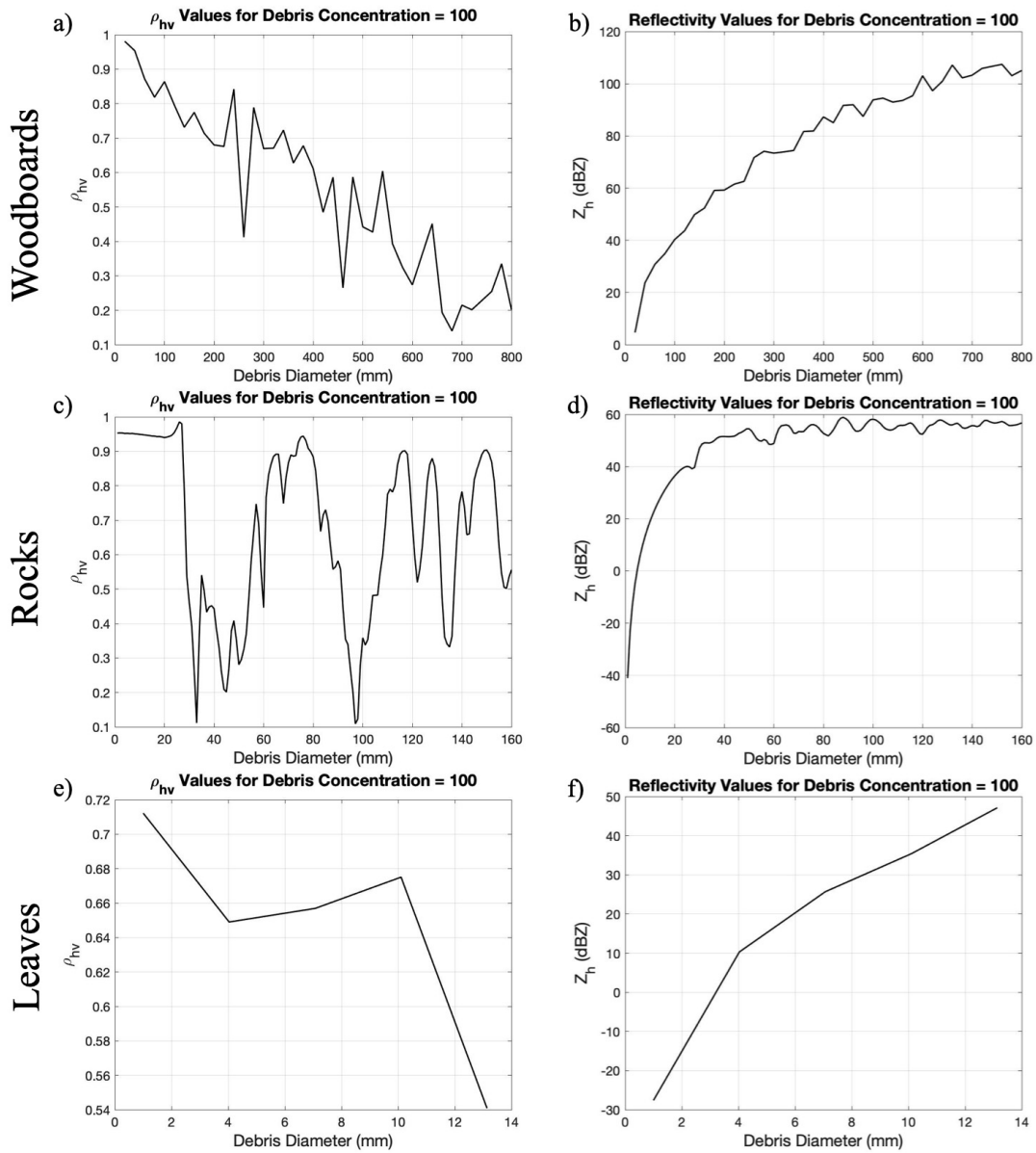
Figure 4.1: Plot of correlation coefficient and radar reflectivity versus debris size for (a) and (b) woodboards, (c) and (d) rocks, and (e) and (f) leaves for a debris concentration of 100. Values of correlation coefficient and radar reflectivity were averaged across 100 experiments.

4.2 Effect of Moisture

To see how the saturation of the leaf changes the ρ_{hv} and Z_H values, the same experiments were run with the same axis ratio but with saturations of 0% and 100%. The 0% saturation case resolved more debris sizes, but for the sake of comparison, only the sizes that were also resolved in the 100% saturation case are shown in Fig. 4.2. For the dry leaf case, ρ_{hv} initially decreases from 1 mm to 5 mm (Fig. 4.2a). The lowest value of ρ_{hv} for the dry leaves (approximately 0.68) is not as low as the partially saturated leaf. Between diameters of 1 mm and 5 mm for the partially saturated leaf, the minimum ρ_{hv} value is approximately 0.65 (Fig. 4.1e). The completely saturated leaf has a minimum ρ_{hv} value that is just lower than 0.65 (Fig. 4.2c). Thus, the ρ_{hv} values across changing saturation for leaves is very similar. For Z_H, values consistently increases with increasing size regardless of how saturated the leaf is (Fig. 4.2b and 4.2d). Comparing the partially saturated case to the saturated leaf case, the Z_H values are very similar. This indicates that, for leaves, the saturation does not change Z_H values.

4.3 Effect of Axis Ratio

Finally, the saturation was kept constant at 22% while the axis ratio of the leaf varied. The three axis ratios compared are 0.1, 0.25, and 0.5. There is not a definitive trend in ρ_{hv} for the 0.25 and 0.5 axis ratio case. It does appear that, at larger debris sizes, ρ_{hv} tends to increase, the exception being the 0.1 axis ratio case. The range of ρ_{hv} values, however, shows a more interesting trend. As the axis ratio increases,
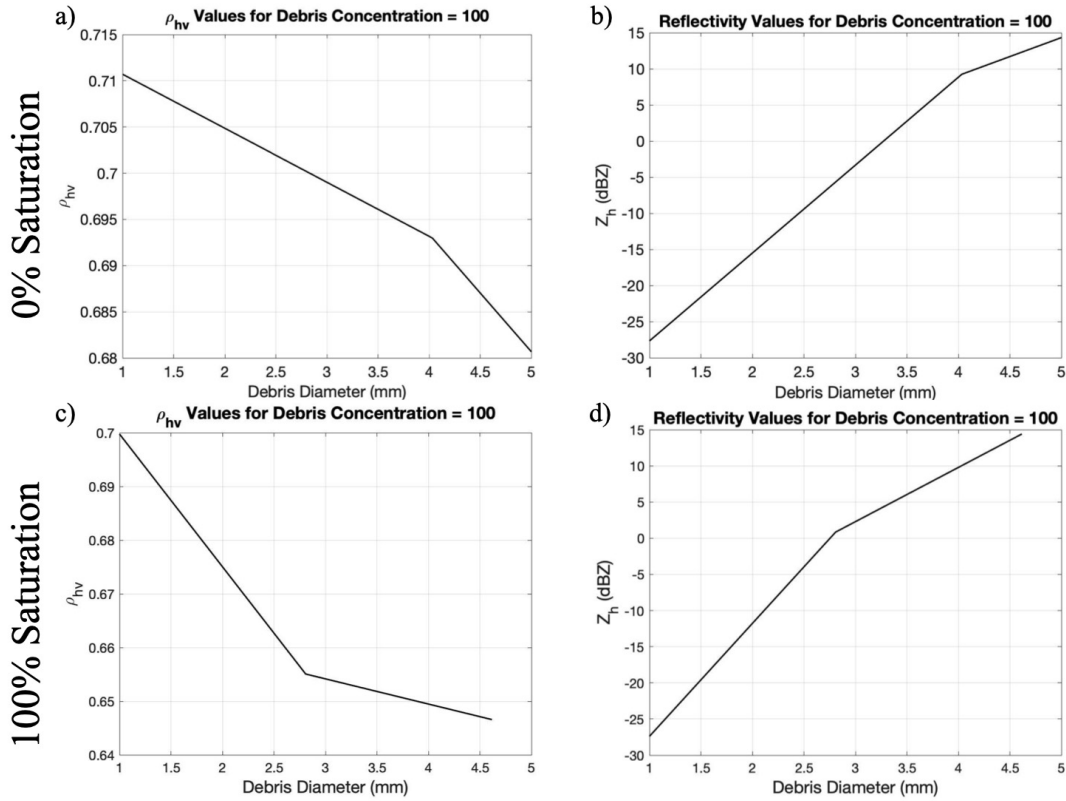
Figure 4.2: Values of correlation coefficient and radar reflectivity for (a) and (b) completely unsaturated leaves and (c) and (d) saturated leaves for a debris concentration of 100. Correlation coefficient and radar reflectivity values were averaged across 100 experiments.

the range of ρ_{hv} values also increases, going from approximately $0.7 - 0.53$ for the 0.1 axis ratio case to $0.92 - 0.97$ in the 0.5 axis ratio case. Thus, the axis ratio of debris heavily impacts the ρ_{hv} value, with higher axis ratios (i.e. more spherical-like targets) producing higher values of ρ_{hv}.

While the axis ratio does not appear to affect the trend of Z_H with increasing debris size, it does seem to affect the value of Z_H for a given debris size. For example, looking at a debris with a diameter of 5 mm, Z_H is approximately 15 dBZ for the 0.1 axis ratio case, 10 dBZ for the 0.25 axis ratio case, and 5 dBZ for the 0.5 axis ratio
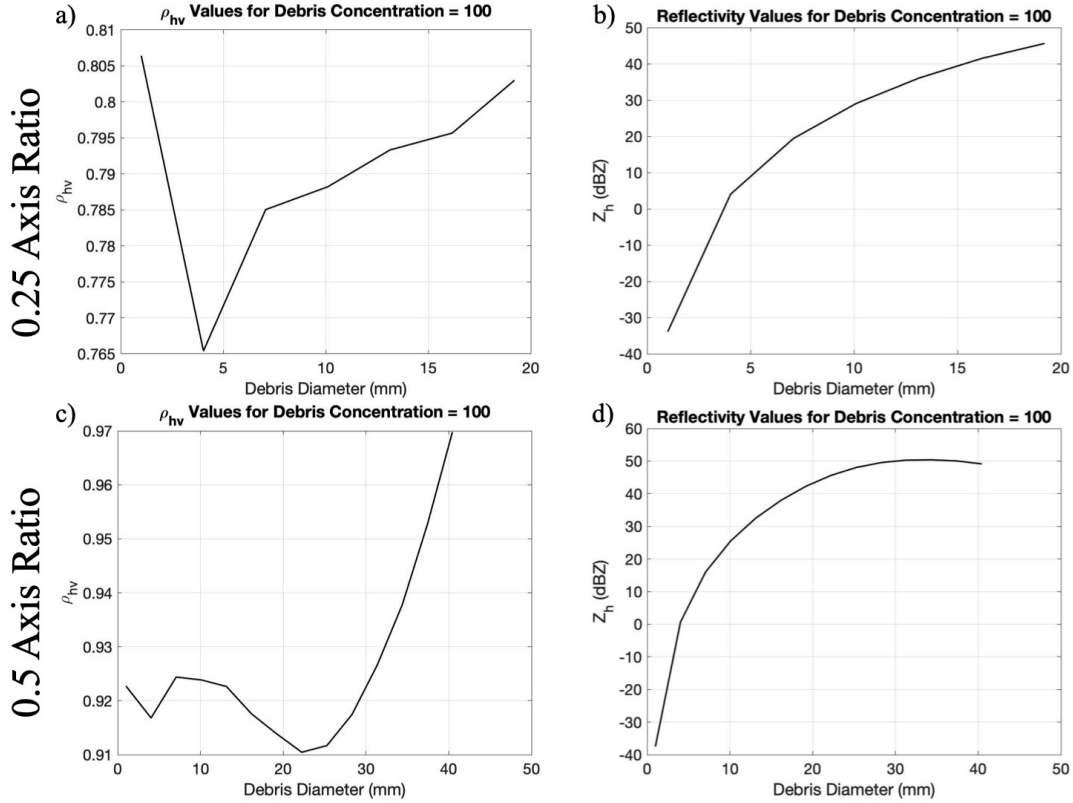
Figure 4.3: Values of correlation coefficient and radar reflectivity for (a) and (b) leaves with an axis ratio of 0.25 and (c) and (d) leaves with an axis ratio of 0.5 for a debris concentration of 100. Correlation coefficient and radar reflectivity values were averaged across 100 experiments.

case. Thus, an increase in axis ratio tends to decrease the Z_H value associated with a given debris size.

4.4 Effect of Debris Concentration

To see the effects of debris concentration on ρ_{hv} and Z_H, a similar experiment was used as in the previous section. However, instead of only averaging across the 100 experiments run, the polarimetric values were also averaged across all debris sizes. This provides an average sense of how ρ_{hv} and Z_H changes with an increase in debris

concentration. The concentrations chosen are 10, 100, 1000, and 10000 and the leaf case chosen was the axis ratio of 0.1 and saturation of 22%.

For the woodboards, ρ_{hv} decreases until a concentration of 1000 (Fig. 4.4a). The most drastic decrease occurs between debris concentrations of 10 and 100. It should be noted that the decrease in ρ_{hv} across concentration is approximately 0.08. Thus, while an increase in the concentration of woodboards in one unit volume does appear to have an impact on ρ_{hv}, the impact is not large. As for Z_H, values linearly increase with increasing debris concentration (Fig. 4.4b).

A similar relation between ρ_{hv} and debris concentration exists for rocks and leaves (Figs. 4.4c and 4.4e). Once again, the most drastic decrease occurs between concentrations of 10 and 100 pieces of debris per unit volume. Also, the decrease seemingly stops at a concentration of 1000, as seen with the woodboards as well. However, the amount ρ_{hv} decreases with the rocks and the leaves are significantly less than what was seen with the woodboards. The change of ρ_{hv} across concentration with the rocks is approximately 0.03 while the change of ρ_{hv} for the leaves is approximately 0.025. Thus, the average ρ_{hv} for the woodboards changes over twice as much compared to the other debris types. The reason for this could be attributed to the scattering properties unique to woodboards due to its dielectric constant. As for Z_H, it also increases linearly with increasing debris concentration for both rocks and leaves (Figs. 4.4d and 4.4f). Woodboards has the highest values of Z_H, followed by the rocks, and then the leaves.

To see which debris sizes are causing the decrease of ρ_{hv} with increasing debris concentration, an average was taken across the smallest 10 sizes and the largest 10
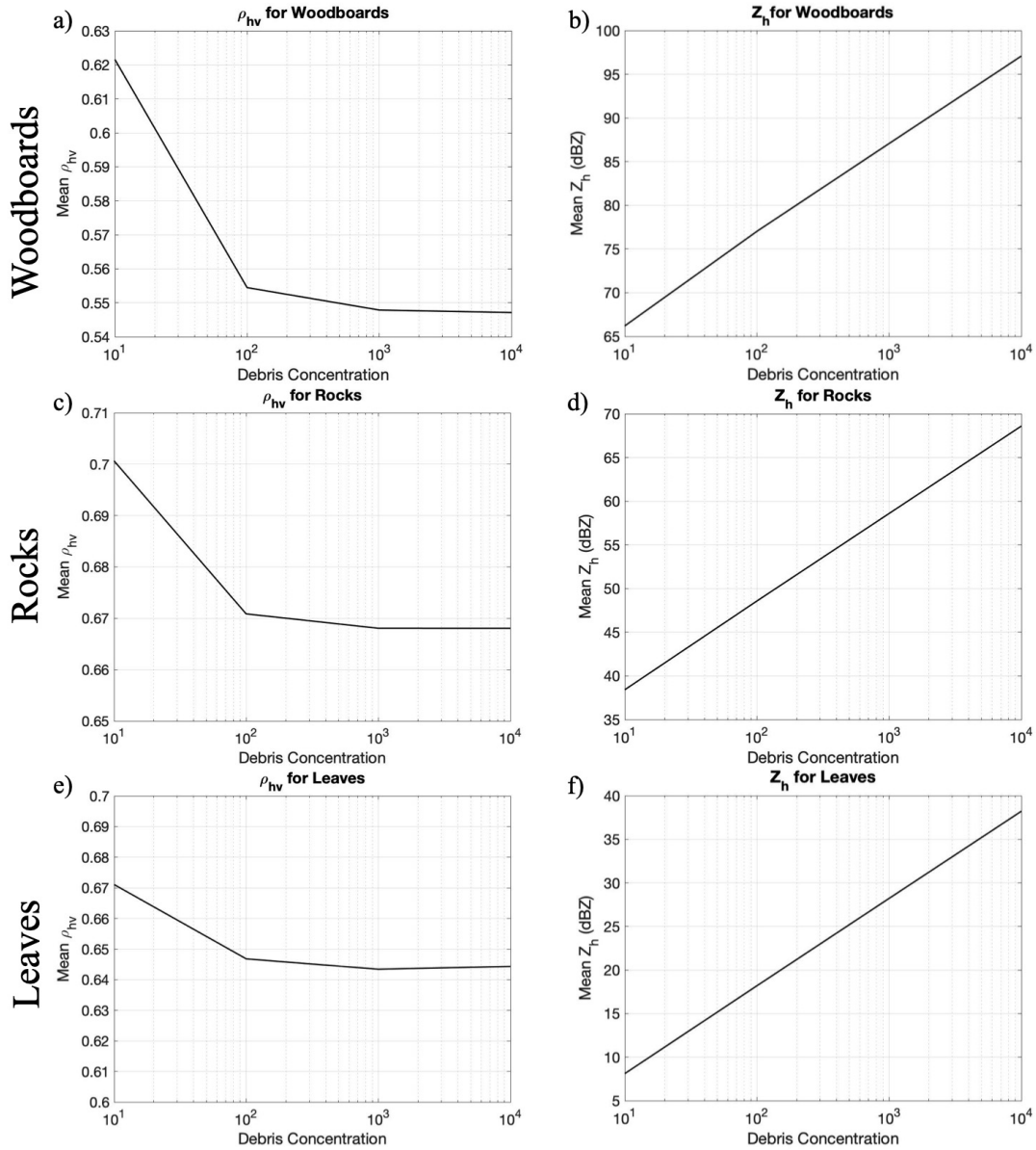
Figure 4.4: Mean values of correlation coefficient and radar reflectivity versus debris concentration for (a) and (b) woodboards, (c) and (d) rocks, and (e) and (f) leaves. Values were averaged across 100 experiments and all debris sizes.
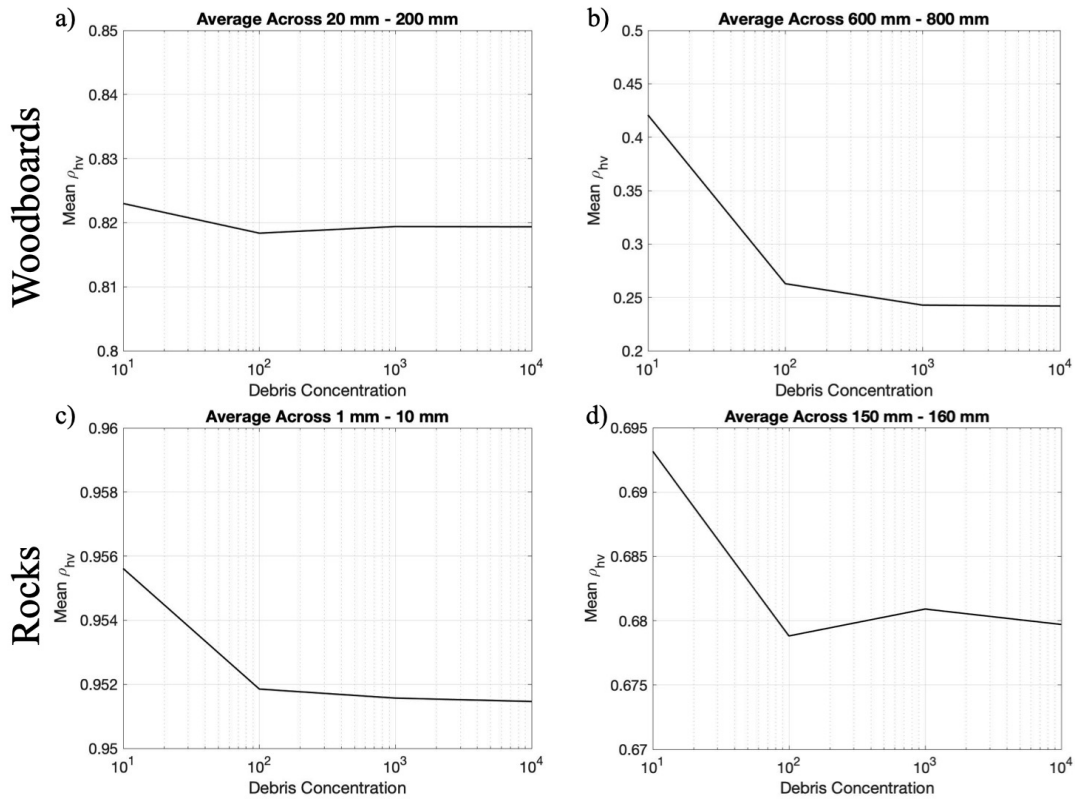
Figure 4.5: Mean values of correlation coefficient versus debris concentration for (a) smallest woodboards, (b) largest woodboards, (c) smallest rocks, and (d) largest rocks. Values were averaged across 100 experiments and then across a set bin of sizes.

sizes for the woodboards and the rocks. A similar average would have been taken for the leaves as well, but not enough sizes were resolved to warrant separating them out.

Looking at the average ρ_{hv} for the smallest sizes, ρ_{hv} is essentially constant with increasing concentration for both the woodboards and the rocks (Figs. 4.5a and 4.5c). For the larger sizes of woodboards (Fig. 4.5c), ρ_{hv} decreases more then the mean ρ_{hv} across all sizes as seen in Fig. 4.4a. This indicates that ρ_{hv} decreases more with increasing debris concentration for larger debris sizes than for smaller debris sizes. A similar result is seen with the rocks, though the change in ρ_{hv} is less drastic (Fig. 4.5d).

A consistent result across all debris types is that the mean ρ_{hv} stops decreasing around a concentration of 1000 pieces of debris per unit volume. It is known that a greater number of randomly oriented particles increases the diversity of the backscatter differential phase in the resolution volume, which in turn lowers ρ_{hv}. This explains the initial decrease in ρ_{hv} seen between a concentration of 10 to 1000 debris pieces per resolution volume. Values of ρ_{hv} decrease more for larger debris sizes because, as seen in Bodine et al. (2014), larger pieces of debris are more likely to have larger variations in the backscatter differential phase. The larger variation in the backscatter differential phase would decrease ρ_{hv}, which would explain the larger decrease in ρ_{hv} for larger debris seen in this study.

It was also seen that, for concentrations greater than 1000, ρ_{hv} values were essentially constant for all debris types. This could be so because, since the T-Matrix method was used to calculate the scattering amplitudes for each debris type and size, there were a total of 1296 different ways one piece of debris could be oriented. As mention in Chapter 3, orientations were selected randomly. Though, past a concentration of 1000, debris orientations would eventually start to repeat as there were no more unique orientations to choose from. Since ρ_{hv} stops decreasing at a concentration of 1000, the effect of repeating debris orientations could be contributing to the flattened mean ρ_{hv} curve past a concentration of 1000.

4.5   Effect of Debris Orientation

The same analysis was done as in the previous sections, but this time the orientation of each debris piece was kept constant. Only woodboards was used for this portion of the study as this debris type showed the most drastic changes in ρ_{hv} across size in the previous section.

The average ρ_{hv} across all experiments and sizes of woodboards barely deviates from unity as debris concentration increases. This indicates that, when presented with a field of scatterers with uniform orientation, ρ_{hv} will not change with increasing concentration. Since these ρ_{hv} values are also averaged across all debris sizes, the fact that the average value is consistently at or near 1 further indicates that, when orientation is constant, debris size also does not effect ρ_{hv}.

Finally, the same set of 100 experiments was run with the woodboards, but with two orientations too choose from for each debris piece. Which debris was assigned which orientation was randomly selected. Fig. 4.6 shows the results from this set of experiments. The same pattern as seen before with the leaves, woodboards, and rocks are shown, though the changes in the values of average ρ_{hv} are very minimal. This contradicts the initial theory that the number of unique orientations is what is driving the flattening of the curve around 1000 piece of debris per unit volume. Since there are only two orientations to choose from and the curve still flattens near a debris concentration of 1000, this means something else is causing this phenomenon. It is possible that the change in average ρ_{hv} decreases with increasing debris concentration due to the saturation of the signal. It could also mean that there is a threshold where
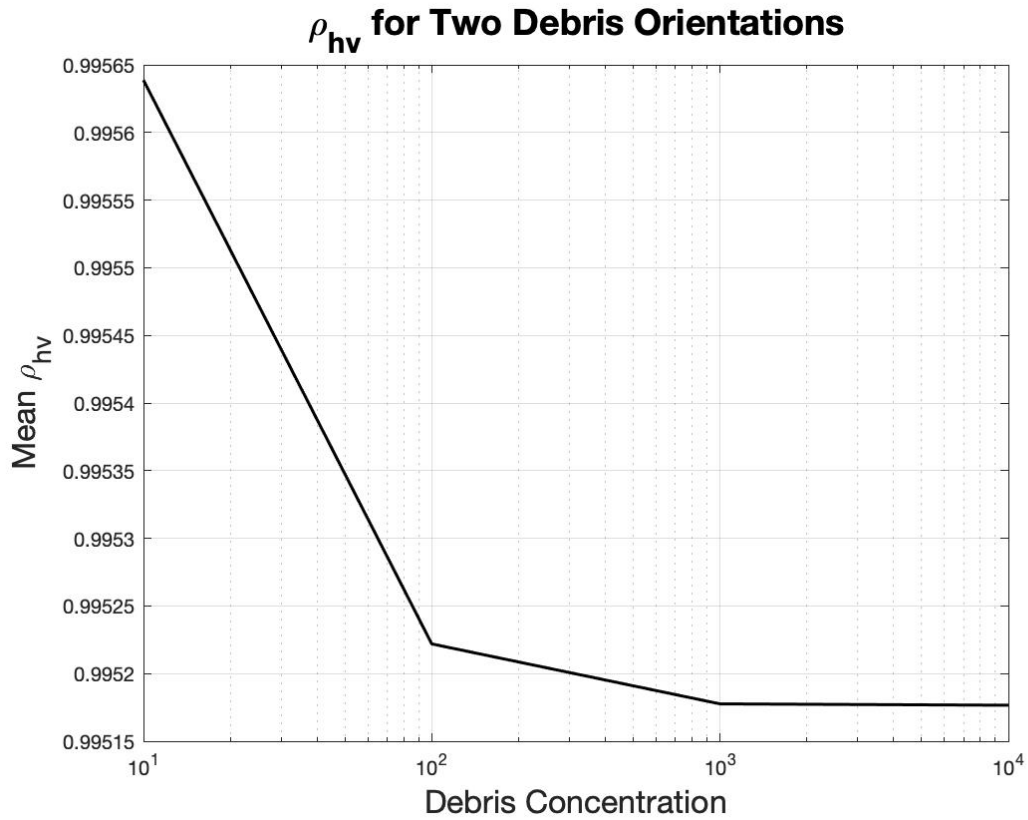
Figure 4.6: Mean ρ_{hv} for woodboards across debris concentration. Two debris orientations were repeated to obtain to various debris concentrations.

debris concentration no longer has significant effects on ρ_{hv}. From the results of this

study, that threshold is around 1000 pieces of debris per unit volume.

Chapter 5

Simulated Relationships Among Tornado Wind Speeds, Debris, and TDSs

5.1 Polarimetric Variables vs. 3D Wind Wield

To define the relationship between the polarimetric variables that define the TDS (primarily ρ_{hv} and Z_H) and the three-dimensional, tornadic wind field, SimRadar and Large-Eddy Simulations of tornadoes were used together to obtain both polarimetric radar data and data of the wind field. In the following section, time series of polarimetric variables and wind parameters are analyzed to see if changes in ρ_{hv} and Z_H can be indicators of increasing tornadic intensity.

5.1.1 Tornadogenesis

In this section, the evolution of ρ_{hv} and Z_H for multiple debris types is analyzed in a tornadogenesis simulation. The 99th percentile vertical velocity (W_{99}), 99th percentile horizontal velocity (V_{h99}), and 99th percentile vertical vorticity (ζ_{99}) for the tornadogenesis simulation are all plotted in Fig. 5.1. The maximum value each of these values reach in the simulation at an elevation angle of 2.5° are 45.5 ms^{-1}, 74.4 ms^{-1}, and 2.8 s^{-1} respectively. The vertical velocity increases first in this simulation, followed by the horizontal velocity and then the vertical vorticity.
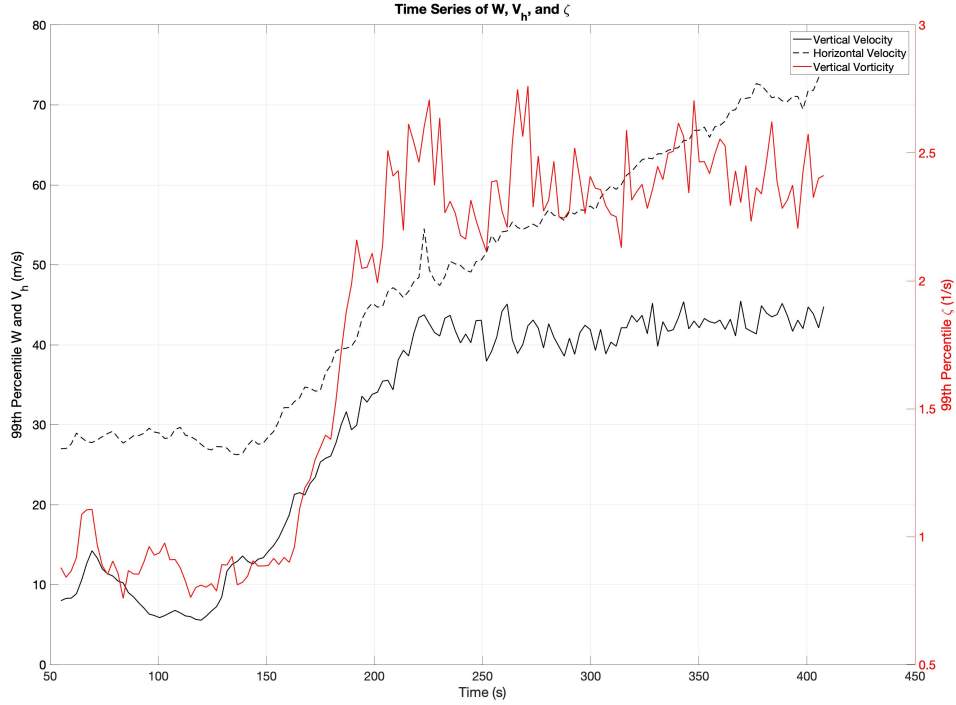
Figure 5.1: 99$^{\text{th}}$ percentile wind parameters for the tornadogenesis simulation.

To see how ρ_{hv} and Z_H evolved through the simulation, values of 10$^{\text{th}}$ percentile ρ_{hv} (ρ_{10}) and 90$^{\text{th}}$ percentile Z_H (Z_{90}) are plotted with W_{99}, V_{h99}, and ζ_{99} for each debris type at an elevation angle of 2.5°. Starting with the leaves, we see that ρ_{10} decreases for increasing values of W_{99}, V_{h99}, and ζ_{99} (Figs. 5.2a, 5.2c, and 5.2e). The time at which ρ_{10} begins to decrease (approximately at 100 s) is close to when W_{99} initially increases (approximately at 120 s). Meanwhile, the Z_H values do not change by more than 3 dBZ throughout the entire simulation (Figs. 5.2b, 5.2d, and 5.2f). Values of Z_{90} initially decrease at the beginning of the simulation before slightly increasing at approximately 200 s when W_{99} is constant (Fig. 5.2b). This is contrary

44

to what has been hypothesized as past studies have theorized that Z_{90} will increase in an intensifying tornado (Bodine et al. 2013).

To quantify how much delay there is in the decrease of ρ_{10} as you go up in elevation, the time at which ρ_{10} decreased by half (t_{rho}) and the time at which the updraft increased by half (t_w) were found. To do this, both the polarimetric data and LES wind data at each height were smoothed using a moving average filter. This removed a lot of the noise in the data, making it easier to find t_{rho} and t_w. Once these times were found, t_w was subtracted from t_{rho}. The result for leaves is shown in Fig. 5.3, where negative time differences indicate where t_w is larger than t_{rho} and positive values indicate that t_{rho} is greater than t_w. Thus, the positive values highlight the "lag" in response of ρ_{10} to an increase in updraft speed.

Looking at Fig. 5.3, there is a general increase of "lag" as height increases. Since lower values of ρ_{10} are associated with debris, the fact that it takes longer for ρ_{10} to decrease after an increase in W_{99} at higher elevations indicates that it takes longer for debris to be lofted to higher heights. This is consistent with what has been seen in observations in a study by Bodine et al. (2013). Of course, in Fig. 5.3 there are exceptions to this statement, especially at a height of 219 m. These exceptions could be due to the fact that, in this relatively weak tornadogenesis simulation, debris is not lofted to the higher elevation angles, thus making the results noisy.

The same parameters are plotted at the same elevation angle as in Fig. 5.2, but now the debris type is woodboards (Fig. 5.4). Again, the overall trend is that ρ_{10} decreases as each wind parameter increases. Compared to the leaves, the woodboard TDS reaches much lower values of ρ_{10} and changes by much more than the leaf TDS
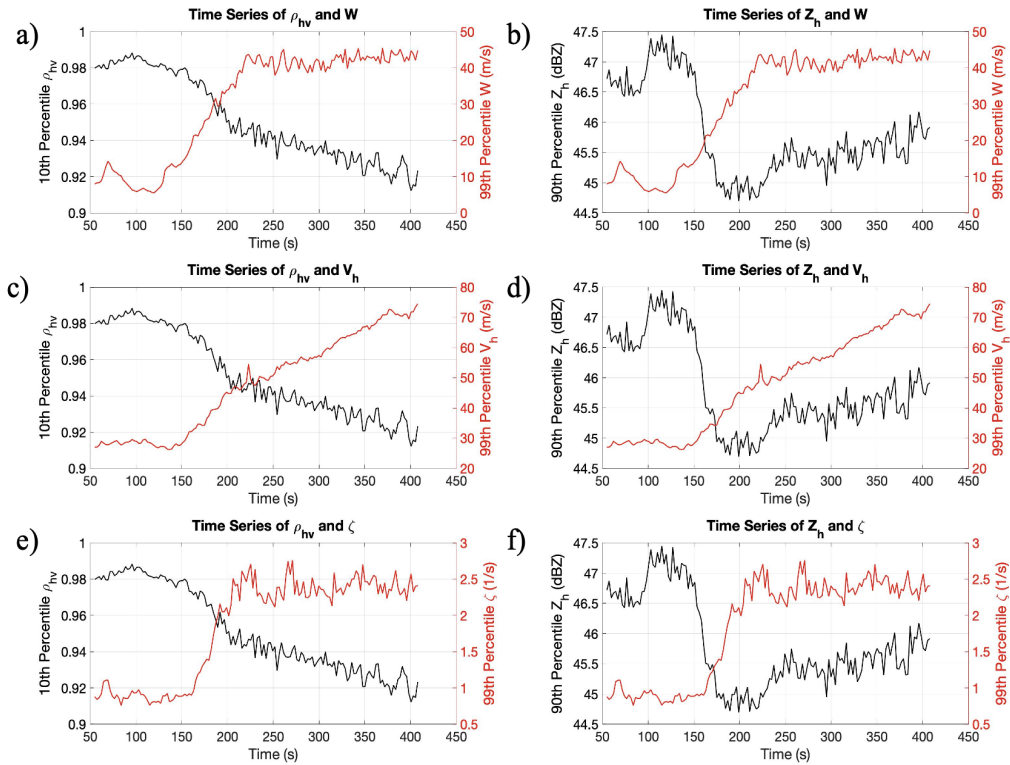
Figure 5.2: Time series plots of ρ_{10} and (a) W_{99}, (c) V_{h99}, and (e) ζ_{99}, and plots of Z_{90} and (b) W_{99}, (d) V_{h99}, and (f) ζ_{99}. All plots are at an elevation angle of 2.5° for the tornadogenesis case.
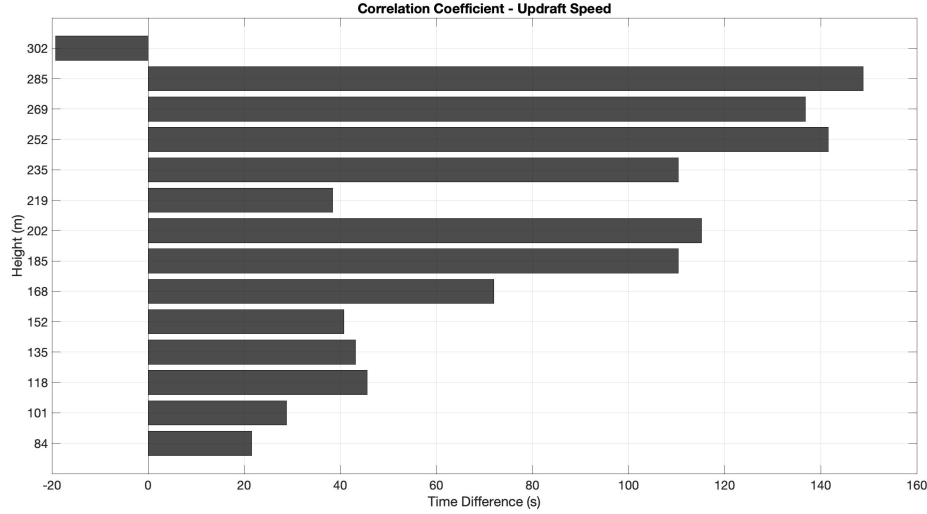
Figure 5.3: Plot of the difference of the time at which ρ_{10} reached half of its total change through the simulation and the time at which W_{99} reached half of its total change through the simulation.

with ρ_{10} dropping from about 0.95 to 0.2. Another notable difference from the leaf TDS is the time at which ρ_{10} begins to decrease more rapidly. For the leaf TDS, this occurred close in time to when W_{99} began to increase. However, for the woodboard TDS ρ_{10} values decrease slightly later into the simulation. This is likely due to the fact that the woodboards weigh more than the leaves, meaning it will take a stronger updraft to loft woodboards compared to leaves to a given height. Values of Z_{90} behave similarly as with the leaves; that is, Z_{90} initially decreases as the wind parameters begin to increase before gradually increasing throughout the rest of the simulation. Unlike ρ_{10} for the woodboard TDS, values of Z_{90} do not change drastically. In fact, the values are generally within the same 3 dBZ range as seen with the leaf TDS.

Like in Fig. 5.3, Fig. 5.5 shows the "lag" in the response of decreasing values of ρ_{10} to an increasing updraft. For each height (except 269 m and 285 m) there are

47
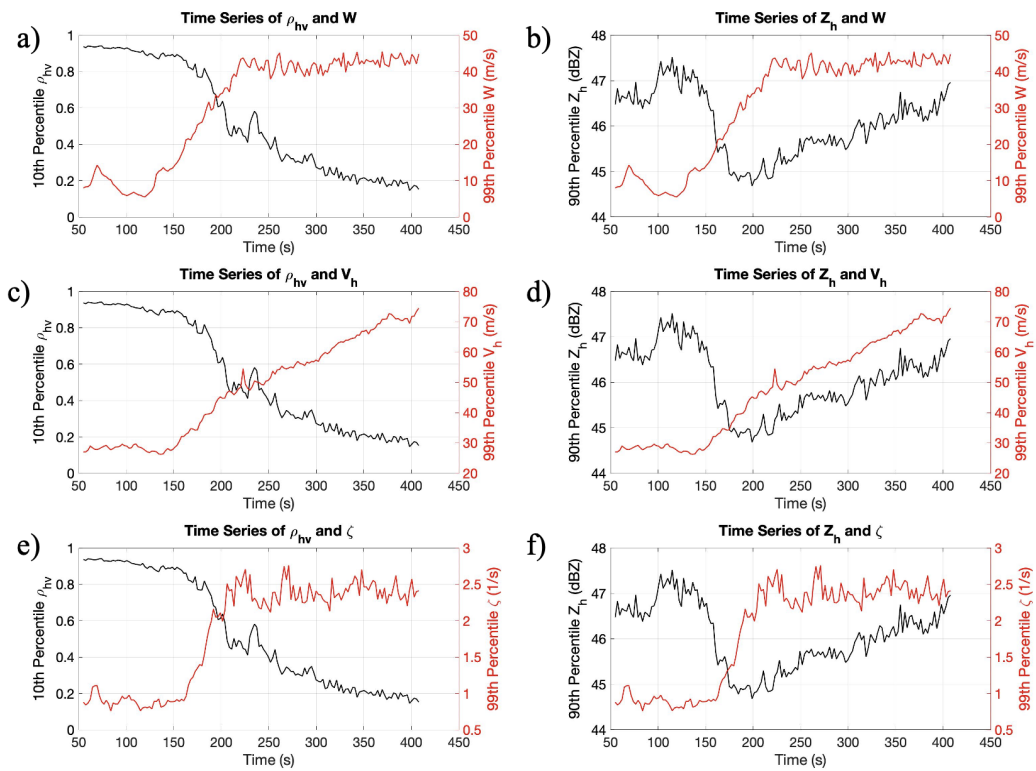
Figure 5.4: Same as in Fig. 5.2, but the debris type is woodboards.
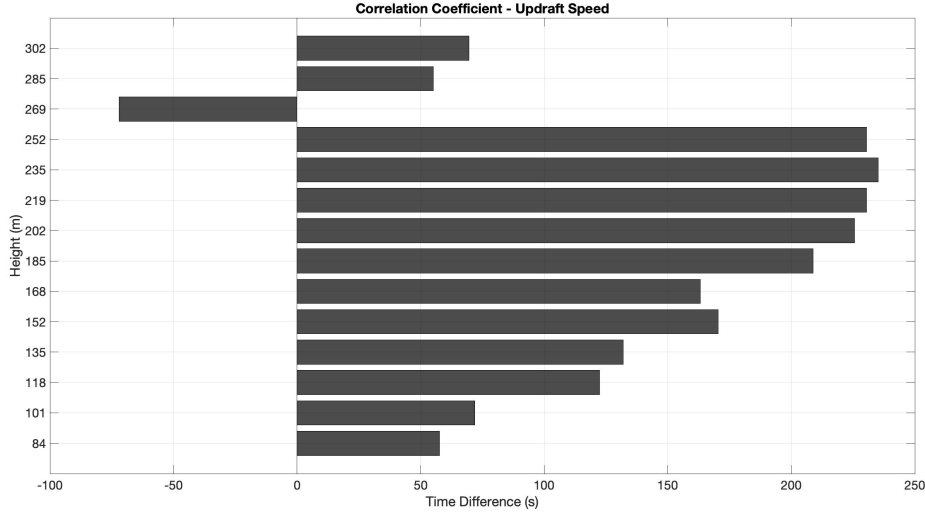
Figure 5.5: Same as in Fig. 5.3, but for woodboards.

larger, positive values of the difference between t_{rho} and t_w. As previously stated, this means that ρ_{10} decreases after W_{99} increases. The two heights where the difference in these two times is less for the woodboards than the leaves is likely due to the woodboards not being lofted as high as the leaves. This also explains why the time difference switches from being largely positive to negative at 269 m.

Finally, looking at values of ρ_{10} for the metal sheet TDS (Fig. 5.6), ρ_{10} changes by more than the leaf TDS but by less than the woodboard TDS. As shown in Chapter 3, ρ_{10} changes very little for debris concentrations past 1000. Since the concentration of the debris is 10000 in each of these simulations, the difference in the values of ρ_{10} across these three scatterers likely comes from intrinsic properties such as the dielectric constant and backscatter cross-section of the target. Of course, not all 10000 debris pieces are lofted in the simulation, so the different values of ρ_{10} for each debris type could also be dependent on how many of the 10000 targets have actually

49

been lofted by the vortex. However, since the heaviest debris type shows the most change in ρ_{10}, it is likely the intrinsic properties of each debris type that determines the range of ρ_{10} reached in the simulation.

The weight of the metal sheets is comparable to the leaves. With this in mind, it makes sense that ρ_{10} begins to decrease close in time to when W_{99} begins to increase (Fig. 5.6a). The other wind parameters, V_{h99} and ζ_{99}, increase after ρ_{10} begins to change (Figs. 5.6c and 5.6e). This occurs for each debris type, indicating that, at the onset of an intensifying vortex, W_{99} plays the largest role in changing the values of ρ_{10} in the TDS. Finally, we see Z_{90} changes similarly to the other two debris types with an initial decrease in values followed by gradual increase (Figs. 5.6b, 5.6d, and 5.6f). Overall, Z_{90} values for each debris type remain within the same 3 dBZ range, indicating that for a relatively weak, intensifying vortex, the debris type does not strongly impact the Z_{90} values in the TDS.

Looking at the lag in response of a decrease in ρ_{10} to an increase in updraft speed (Fig. 5.7), we see the smallest, positive time differences compared to the other debris types. This means that it takes the least amount of time for the metal sheets to be lofted for a given updraft speed. Since the weight of the leaves and metal sheets is comparable, the larger horizontal surface area of the metal sheets could have something to do with the decreased time differences.

5.1.2   Strong Tornadogenesis

The three wind parameters - W_{99}, V_{h99}, and ζ_{99} - are plotted in Fig. 5.8. The maximum value at an elevation angle of 2.5° of W_{99} is 86.4 ms^{-1}, V_h is 79.4 ms^{-1}, and ζ_{99}
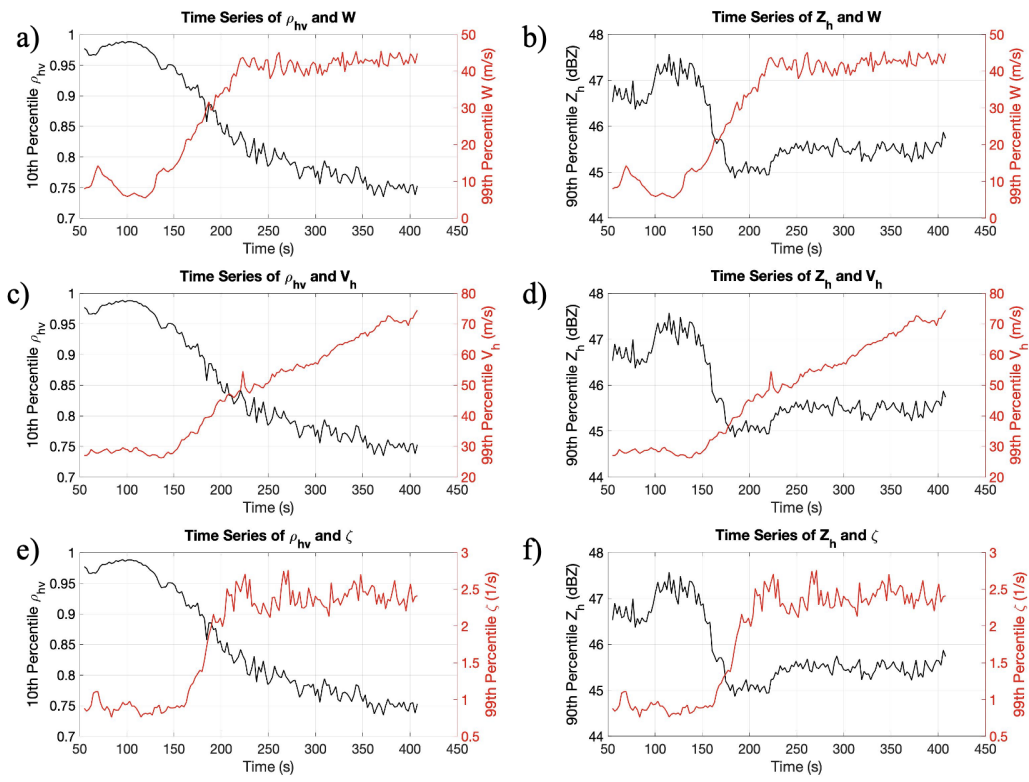
Figure 5.6: Same as in Fig. 5.2, but for metal sheets.
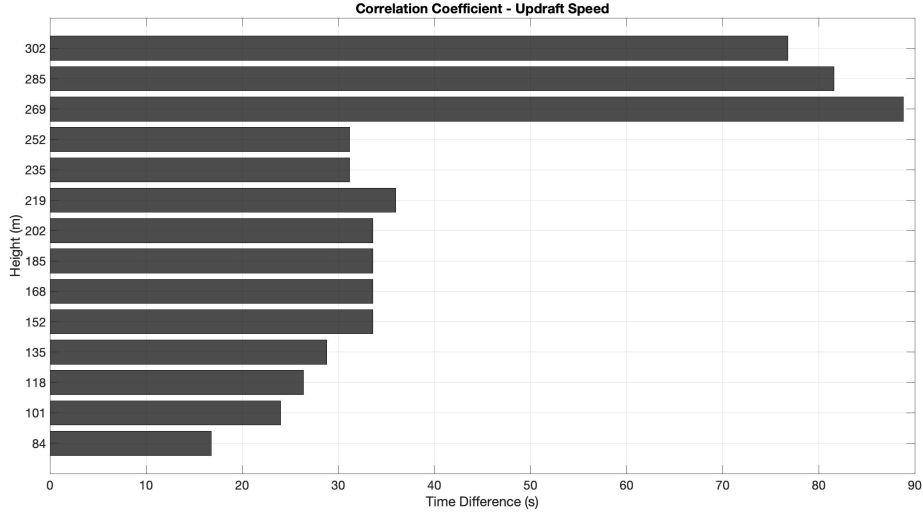
Figure 5.7: Same as in Fig, 5.3, but with metal sheets.

is 4.5 s^{-1}. Compared to the first tornadogenesis case, W_{99} and ζ_{99} are nearly twice as strong by the end of the strong tornadogenesis simulation. The three wind parameters also strengthen slightly later on in the simulation compared to the tornadogenesis case and continue to strengthen throughout the rest of the simulation (Figs. 5.1 and 5.8).

Both ρ_{10} and Z_{90} for leaves are plotted with W_{99}, V_{h99}, and ζ_{99} in Figs. 5.9. Once again, all values were taken at an elevation angle of 2.5°. Generally speaking, ρ_{10} decreases as W_{99}, V_{h99}, and ζ_{99} increase (Figs. 5.9a, 5.9c, and 5.9e). The time at which ρ_{10} begins to decrease is visually approximated to be 190 s. This lines up well with the increase in W_{99}, V_{h99}, and ζ_{99}, indicating that ρ_{10} values for leaves responds quickly to changes in the vertical and horizontal velocities and vertical vorticity. Between 200 and 300 s, the ρ_{10} curve flattens. In this time interval, both V_{h99} and ζ_{99} change less rapidly (Figs. 5.9c and 5.9e). This could indicate that

52
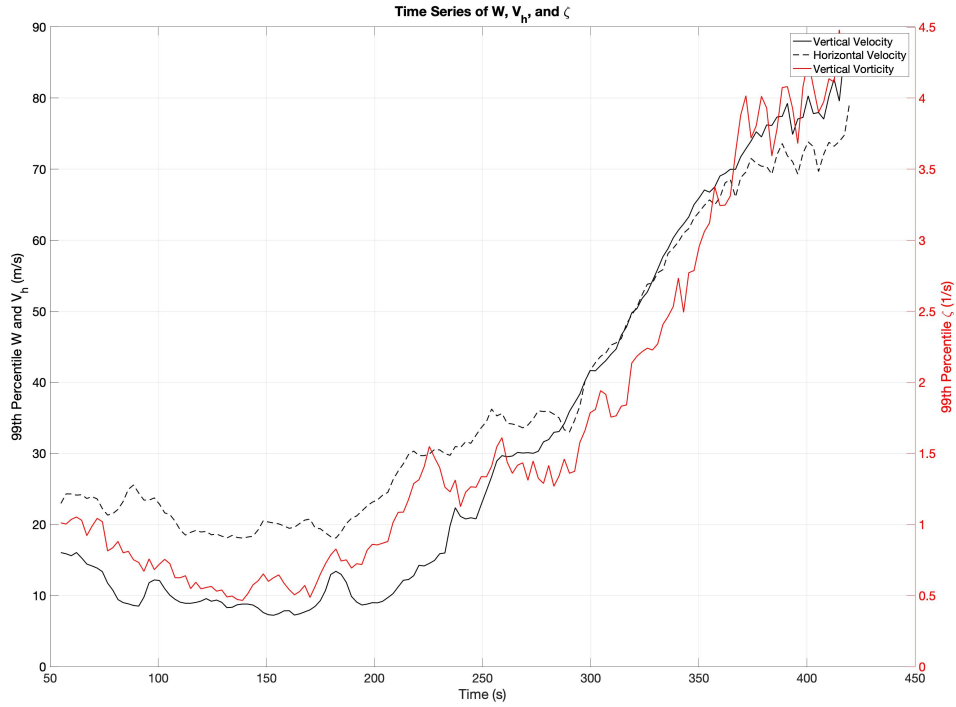
Figure 5.8: Plot of W_{99}, V_{h99}, and ζ_{99} for the stronger tornadogenesis simulation.

ρ_{10} for leaves is also sensitive to changes in V_{h99} and ζ_{99} along with W_{99}. Comparing the range of ρ_{10} values throughout the simulation to that in the initial tornadogenesis case, ρ_{10} begins and ends near the same values for both simulations (Figs. 5.2a and 5.9a). Since the stronger tornadogenesis case was initialized with 100000 pieces of debris compared to the 10000 in the weaker tornadogenesis case, the extra debris in the stronger case did not greatly alter the ρ_{10} values.

The overall trend for Z_{90} shows that Z_{90} increases with increases in the three wind field parameters (Figs. 5.9b, 5.9d, and 5.9f). The Z_{90} values begin to increase near the same time as W_{99}, V_{h99}, and ζ_{99} begin to increase (this occurs near 200 s). In the same time interval where the ρ_{10} values remained more constant (between 200 and 300 s),
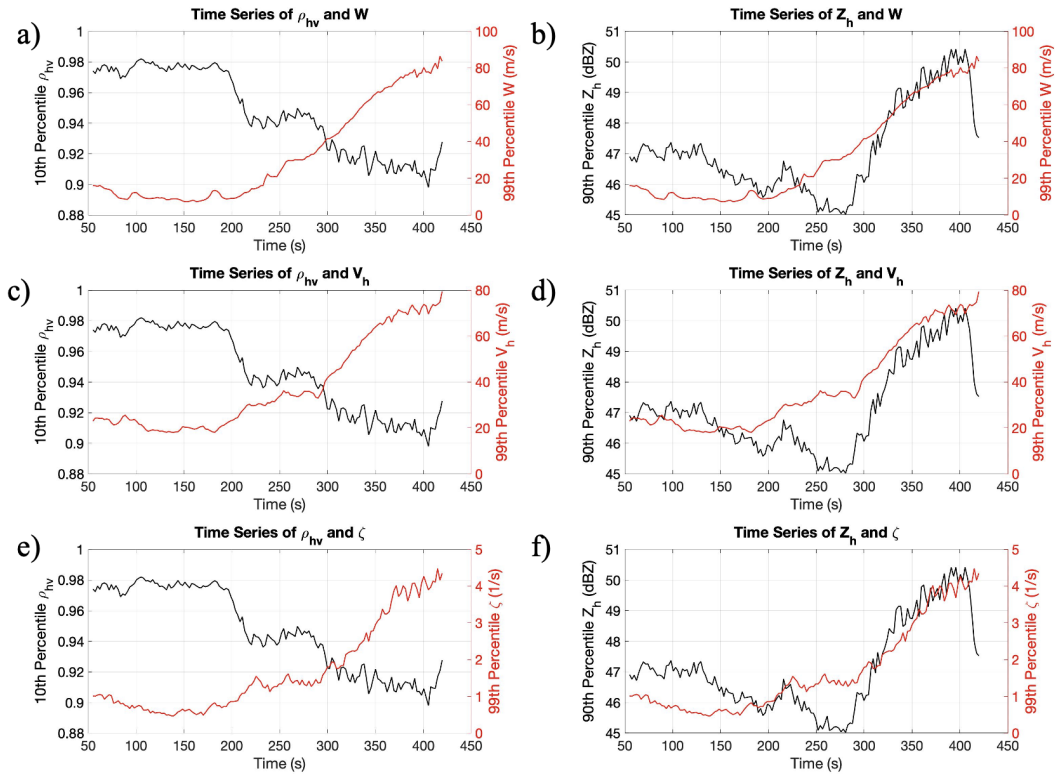
Figure 5.9: Time series plots of ρ_{10} and (a) W_{99}, (c) V_{h99}, and (e) ζ_{99}, and plots of Z_{90} and (b) W_{99}, (d) V_{h99}, and (f) ζ_{99}. All plots are at an elevation angle of 2.5° for the stronger tornadogenesis case.

Z_{90} decreases. This decrease in Z_{90} could be caused by the semi-constant horizontal wind speed or vertical vorticity during this time. It could also be that the debris that was initially lofted was lifted to a higher elevation by the intensifying updraft, leaving less debris at the 2.5° elevation. At the end of the simulation, Z_{90} increases much more drastically than in the weaker tornadogenesis case with Z_{90} increasing from about 45 dBZ to 50 dBZ (Fig. 5.2b). The larger increase in Z_{90} in the stronger tornadogenesis case could be due to more debris being lofted compared to the weaker tornadogenesis case or the stronger updraft lofting more debris to the 2.5° elevation.

Looking at the same parameters but for the woodboards, it is clear that ρ_{10} decreases as each wind parameter increases (Figs. 5.10a, 5.10c, and 5.10e). The most obvious difference between the woodboards and the leaves is that the ρ_{10} values for the woodboards is much lower than that for the leaves. The change in ρ_{10} for the woodboards is also much more drastic, as ρ_{10} drops from near 0.8 to below 0.2 for the woodboards while ρ_{10} for the leaves does not change more than 0.1 throughout the whole simulation. Another difference occurs between 200 and 300 s. During this time interval, the ρ_{10} for the leaves remained semi-constant. The ρ_{10} values for the woodboards actually increases during this time. This increase in ρ_{10} could be because woodboards are heavier than leaves, meaning they are likely to fallout of the updraft faster than lighter debris (Magsig and Snow 1998).

Compared to the weaker tornadogenesis case, ρ_{10} begins at a lower value (Figs. 5.4a and 5.10a). Values of ρ_{10} also decrease more gradually than in the weaker tornadogenesis case, likely due to the more gradually increasing updraft during the first half of the simulation. One similarity across the two tornadogenesis cases for the

woodboards is that ρ_{10} for woodboards decreases later into the simulation than the lighter debris types.

The Z_{90} values show an almost identical trend to that for the leaves. During the 200 to 300 s interval, Z_{90} decreases as V_{h99} and ζ_{99} change less drastically (Figs. 5.10d and 5.10f). Otherwise, Z_{90} increases with increases in all three wind parameters. Also, Z_{90} for the woodboards shows a more prominent increasing trend at the end of the simulation compared to the weaker tornadogenesis case (Figs. 5.4b and 5.10b).

Finally, looking at the metal sheets reveals the same overall trend as seen with the previous two debris types. As ρ_{10} decreases, the three wind parameters increase (Figs. 5.11a, 5.11c, and 5.11e). The amount by which ρ_{10} decreases for metal sheets is more than the leaves but less than seen with the woodboards, similar to the weaker tornadogenesis case. The range of ρ_{10} in this simulation is also similar to the weaker tornadogenesis case.

In the interval between 200 and 300 s, ρ_{10} increases. It is interesting to note that, looking at the Z_{90} values, Z_{90} increases within the same time interval (Figs. 5.11b, 5.11d, and 5.11f). However, the increase occurs earlier within this interval than the increase in ρ_{10}. The change in Z_{90} is relatively small, never exceeding 4 dBZ. In fact, the overall, increasing trend in Z_{90} throughout the simulation is much more subtle than the other debris types. Both the leaves and woodboards had values of Z_{90} increasing at the end of the simulation. Meanwhile, values of Z_{90} for the metal sheets remain relatively constant from the beginning of the simulation to about 120 s. This overlaps when ρ_{10} is also constant, though this parameter remains constant until 200 s. Values of Z_{90} then decrease from 120 s to about 200 s. After the 200 and
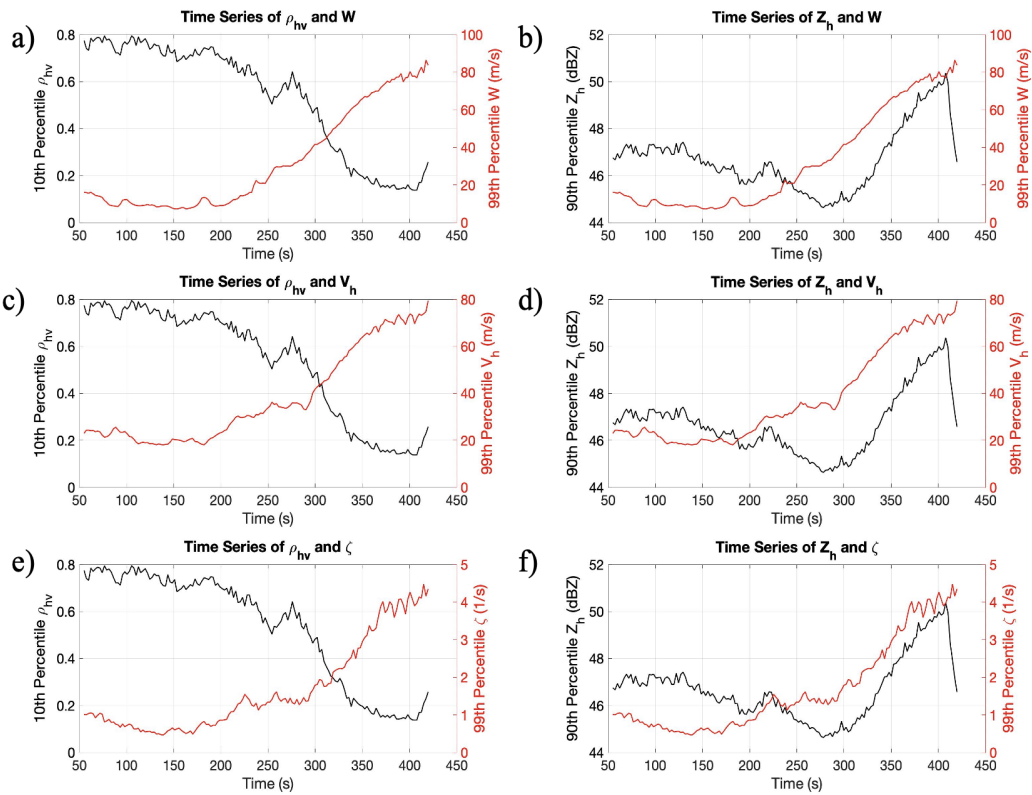
Figure 5.10: Same as in Fig. 5.9, but with woodboards.

300 s interval, Z_{90} then increases as the simulation ends. The variability in Z_{90} for the metal sheets could indicate that other factors are contributing to the change in these values outside the increase of the wind field parameters (i.e. debris fallout).

To see how the difference in ρ_{10} and W_{99} change with height, the same analysis as done in the previous section was performed for the woodboards. Only this debris type was analyzed here because data from all elevations was obtained only for the woodboards due to time constraints on the project. Like before, t_{rho} and t_w were found by taking the time at which each parameter reached half of the difference between its starting and ending value.

Table 5.1: Table of time differences for both the weak and strong tornadogenesis cases. The asterisk implies the values are from the strong tornadogenesis simulation for that debris type.

Height (m)	Leaves	Woodboards	Metal Sheets	Woodboards*
84	21.6 s	57.6 s	16.8 s	-9.6 s
118	45.6 s	122.4 s	26.4 s	21.6 s
152	40.8	170.4	33.6 s	38.4 s

As seen in Fig. 5.12, the difference in time becomes more and more positive with height. This indicates the time it takes for woodboards to be lofted increases with increasing height. Thus, for a given updraft speed, it will take longer for ρ_{10} to decrease the higher above ground the observations are taken from. Comparing this with the height analysis done for the weaker tornadogenesis case (Fig. 5.5), the time difference for the stronger tornadogenesis case is shorter than the weaker case. The difference in times can be more easily seen in Table 5.1. Here is can be seen that the time it takes woodboards to be lofted in the stronger tornadogenesis simulation is
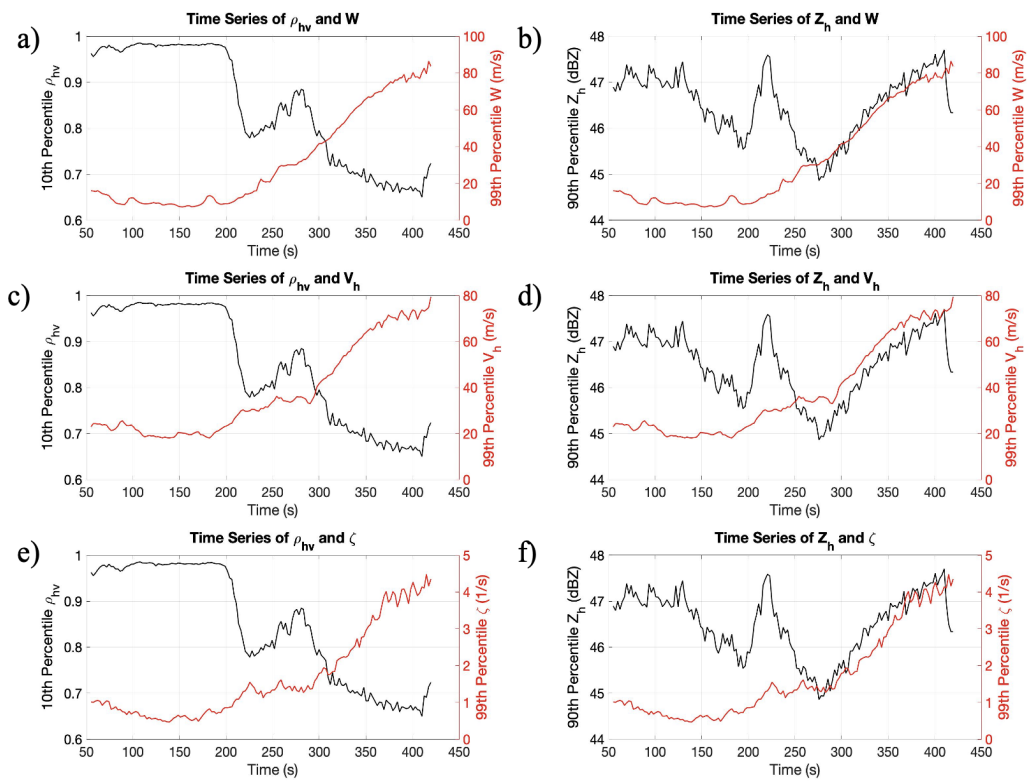
Figure 5.11: Same as in Fig. 5.9, but for metal sheets.
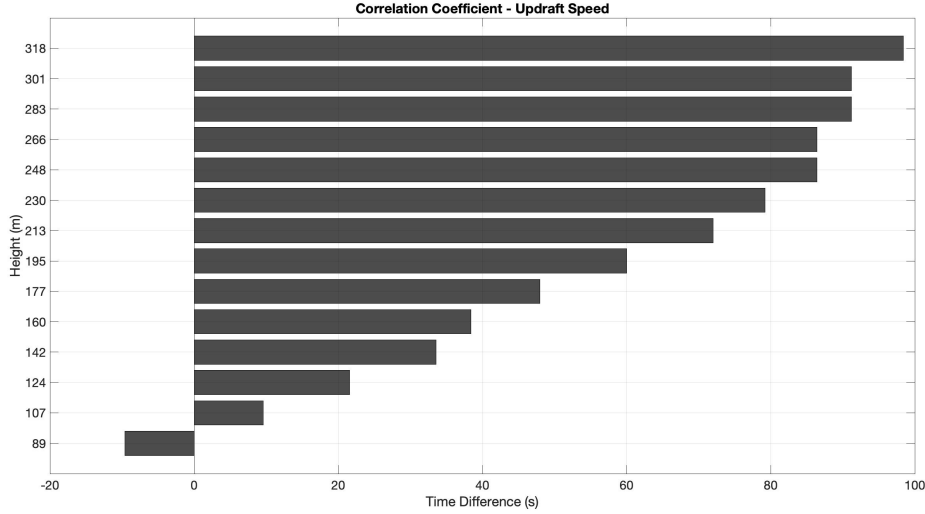
Figure 5.12: Same as in Fig. 5.3, but for woodboards and the stronger tornadogenesis case.

less than all debris types in the weaker tornadogenesis simulation. This is likely due to the stronger updraft speeds lofting debris to higher heights faster than the weaker updraft in the weaker tornadogenesis case.

5.1.3 Tornado Dissipation

In Fig. 5.13, W_{99}, V_{h99}, and ζ_{99} are plotted across time. W_{99} has a max value of 65.9 ms^{-1} and reaches a minimum value of 5.1 ms^{-1} near the end of the simulation. V_{h99} has a max value of 97.7 ms^{-1} and a minimum value of 27.7 ms^{-1}. Finally, ζ_{99} has a maximum value of 3.7 s^{-1} and a minimum value of 0.9 s^{-1}. Near the end of the simulation, W_{99} increases while ζ_{99} decreases.

Using the same debris concentration as the strong tornadogenesis case, the tornado dissipation case was also analyzed with the same three debris types. Looking first at the leaves, ρ_{10} generally increases as W_{99}, V_{h99}, and ζ_{99} decrease (Figs. 5.14a,

60

Figure 5.13: Plot of W_{99}, V_{h99}, and ζ_{99} for the dissipation simulation.

5.14c, and 5.14e). Values of ρ_{10} begin to increase after W_{99}, V_{h99}, and ζ_{99} begin to increase (Figs. 5.14a, 5.14c, and 5.14e). There is thus a delayed response of ρ_{10} to a decreasing wind field. In the last 200 s of the simulation, ρ_{10} actually decreases while W_{99} increases. The increase in W_{99} is not drastic at this time as it only changes by about 10 ms^{-1}. Since ρ_{10} changed in response to a relatively small change in W_{99}, this indicates that ρ_{10} for leaves is sensitive to changes in W_{99} rather than V_{h99} and ζ_{99}.

As for Z_{90}, values of Z_{90} decrease along with the three wind parameters (Figs. 5.14b, 5.14d, and 5.14f). At the end of the simulation, Z_{90} increases in response to the increase in W_{99}. It is also interesting to note that ζ_{99} slightly decreases as W_{99} increases, which shows how interconnected ζ_{99} is with W_{99}.
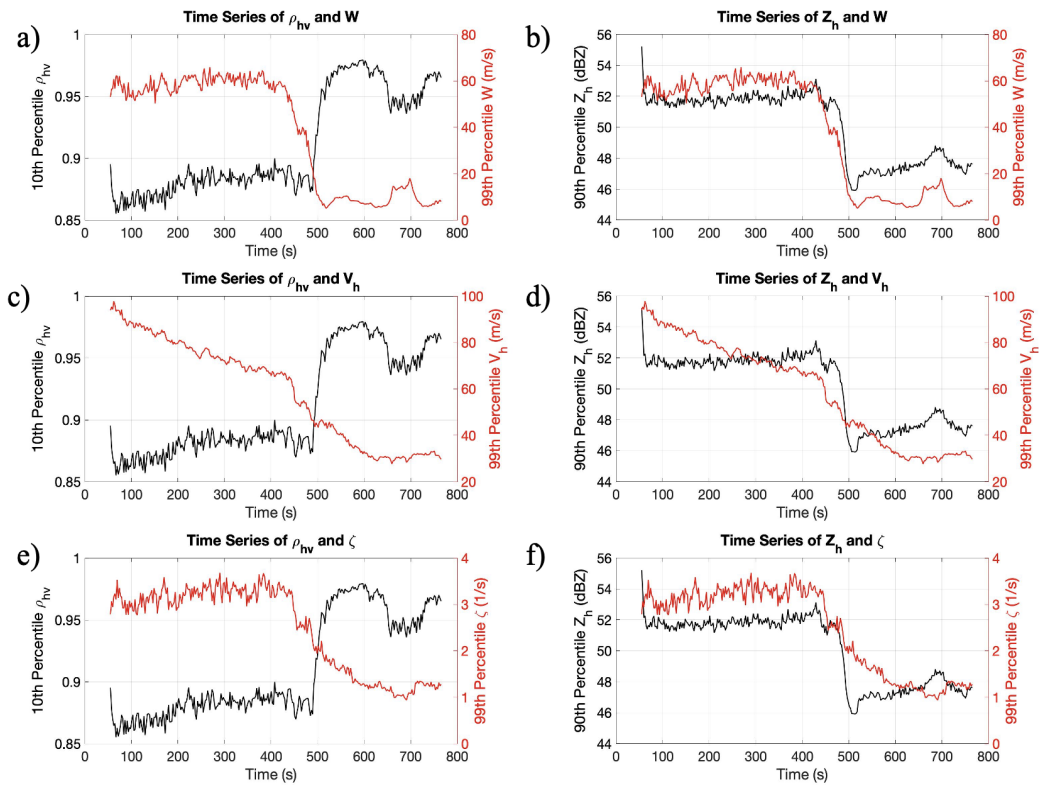
Figure 5.14: Time series plots of ρ_{10} and (a) W_{99}, (c) V_h99, and (e) ζ_{99}, and plots of Z_{90} and (b) W_{99}, (d) V_h99, and (f) ζ_{99}. All plots are at an elevation angle of 2.5° for the dissipation case.

The values of ρ_{10} for the woodboards show the same trend as with the leaves – ρ_{10} increases as W_{99}, V_{h99}, and ζ_{99} decrease (Figs. 5.15a, 5.15c, and 5.15e). The change in ρ_{10} occurs abruptly as it occurs within a 100 s time interval. Before and after this change, ρ_{10} is relatively constant. Again, ρ_{10} changes by more for the woodboards than the leaves; however, another notable difference occurs in this tornado dissipation case. As the updraft increases at 650 s, ρ_{10} does not decrease as drastically as with the ρ_{10} for the leaves. This indicates that woodboards – a heavier object – does not respond to small changes in the wind field.

While ρ_{10} does not respond drastically to small changes in W_{99}, Z_{90} does increase with increasing values of W_{99} at the end of the simulation (Fig. 5.15b). Other than this instance, Z_{90} decreases with decreasing values of all three wind parameters in this simulation (Figs. 5.15b, 5.15d, and 5.15f).

Finally, ρ_{10} for the metal sheets increases by more than the leaves but less than the woodboards throughout this simulation (Figs. 5.16a, 5.16c, and 5.16e). For each debris type, ρ_{10} appears to not change in response to V_{h99} and ζ_{99} as much as W_{99}. This is so as ρ_{10} for each debris type decrease at the end of the simulation as W_{99} increases. While the woodboards had the least amount of response to the increase in W_{99}, the metal sheets have the most prominent response with ρ_{10} decreasing by almost half of the total change of ρ_{10} throughout the simulation (Figs. 5.16a, 5.16c, and 5.16e). Likewise, Z_{90} also increases by near half the total change of Z_{90} across the simulation (Figs. 5.16b, 5.16d, and 5.16f). Again, other than this instance, Z_{90} decreases with decreases in the three wind parameters. Since the woodboards and the metal sheets have the same density, the difference in their response to the
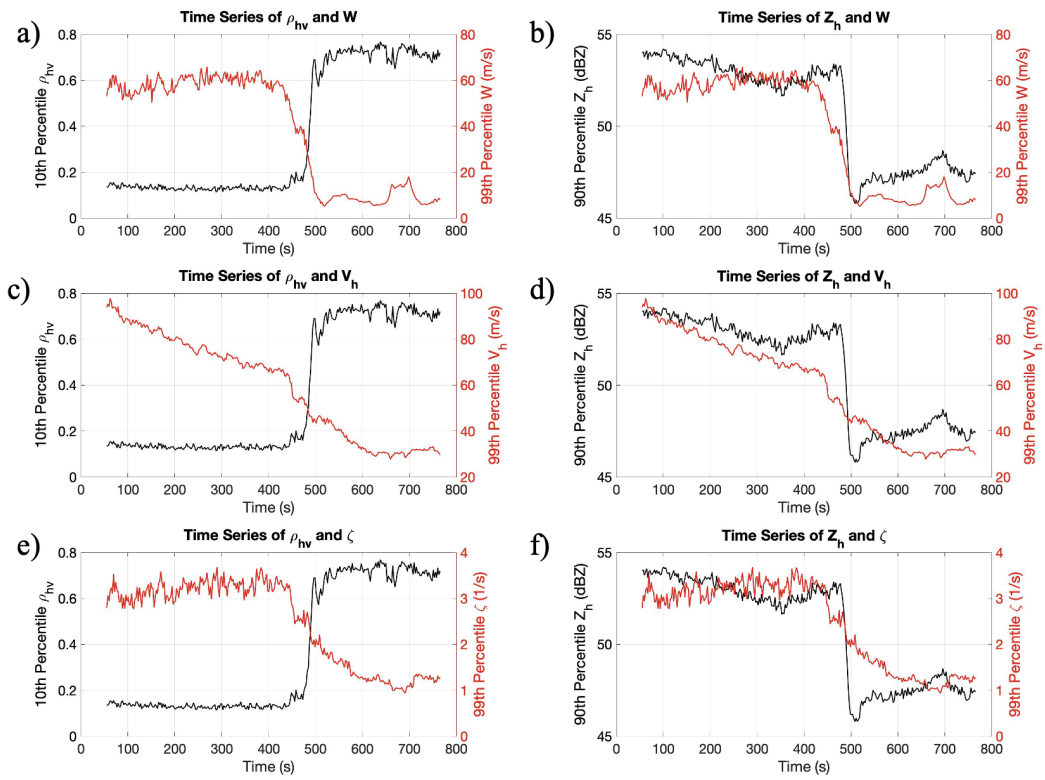
Figure 5.15: Same as in Fig. 5.14, but for woodboards.

same change in W_{99} is more likely due to the aerodynamics of the metal sheets versus the woodboards.

5.2 Horizontal Development of the TDS

5.2.1 Strong Tornadogenesis

In this simulation, the updraft at an elevation angle of 2.5° does not reach more than 10 ms^{-1} until 172 s into the simulation. Looking at plan-position indicator plots of the TDS for leaves, the shape of the TDS at 230 s is largely determined by the location of the updraft (Fig. 5.17a). At this time, the TDS has an appendage extending from its western side. This appendage lies just outside of the updraft, indicating that the appendage is debris being lofted into the swirling vortex. It is also worthy to note that the horizontal velocities on the western side of the vortex at this time are stronger than the eastern side (Fig. 5.17b). The appendage is thus dictated both by the local maxima in the updraft and the stronger horizontal velocities on the western side of the vortex.

As the tornado strengthens, the TDS begins to split into two lobes (Figs. 5.17d - 5.17f). The upper lobe is located just to the west of the central updraft and near the vorticity maximum, while the more southern lobe more closely follows the southward dip in the vertical velocity contours (Figs. 5.17e and 5.17f). As time progresses, this southern lobe becomes more detached from the northern lobe, with the northern lobe remaining just to the west of the updraft and vorticity maximum (Figs. 5.17g - 5.17i). In fact at 340.6 s into the simulation, the southern lobe has mostly fallen
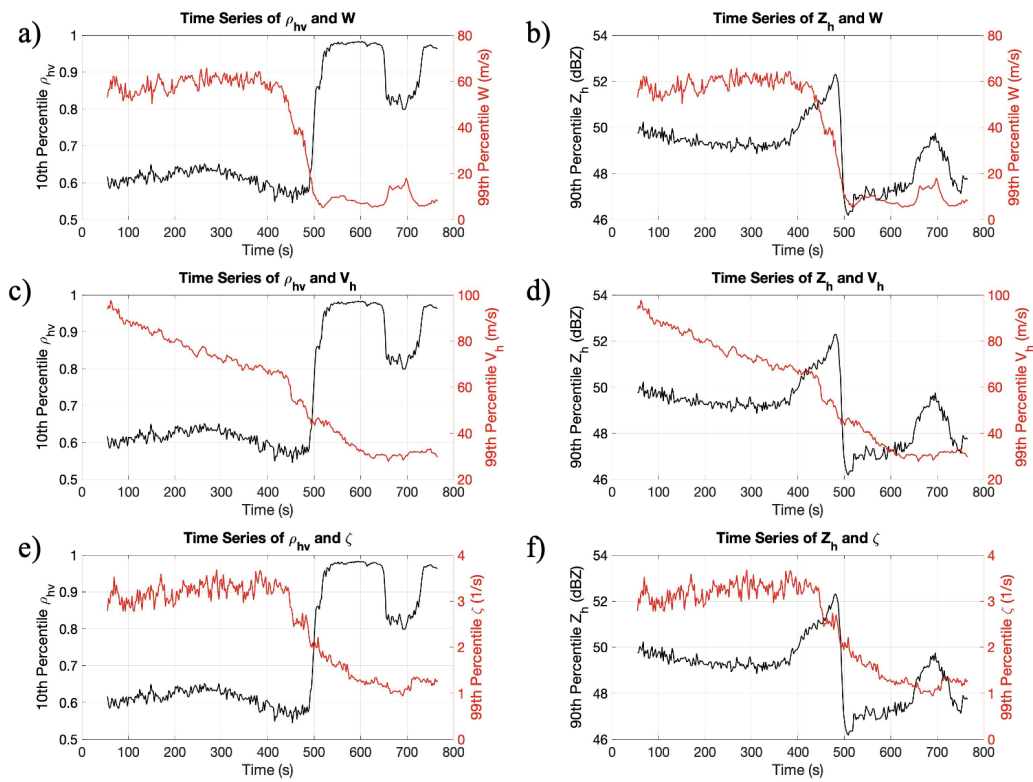
Figure 5.16: Same as in Fig. 5.14, but with metal sheets.
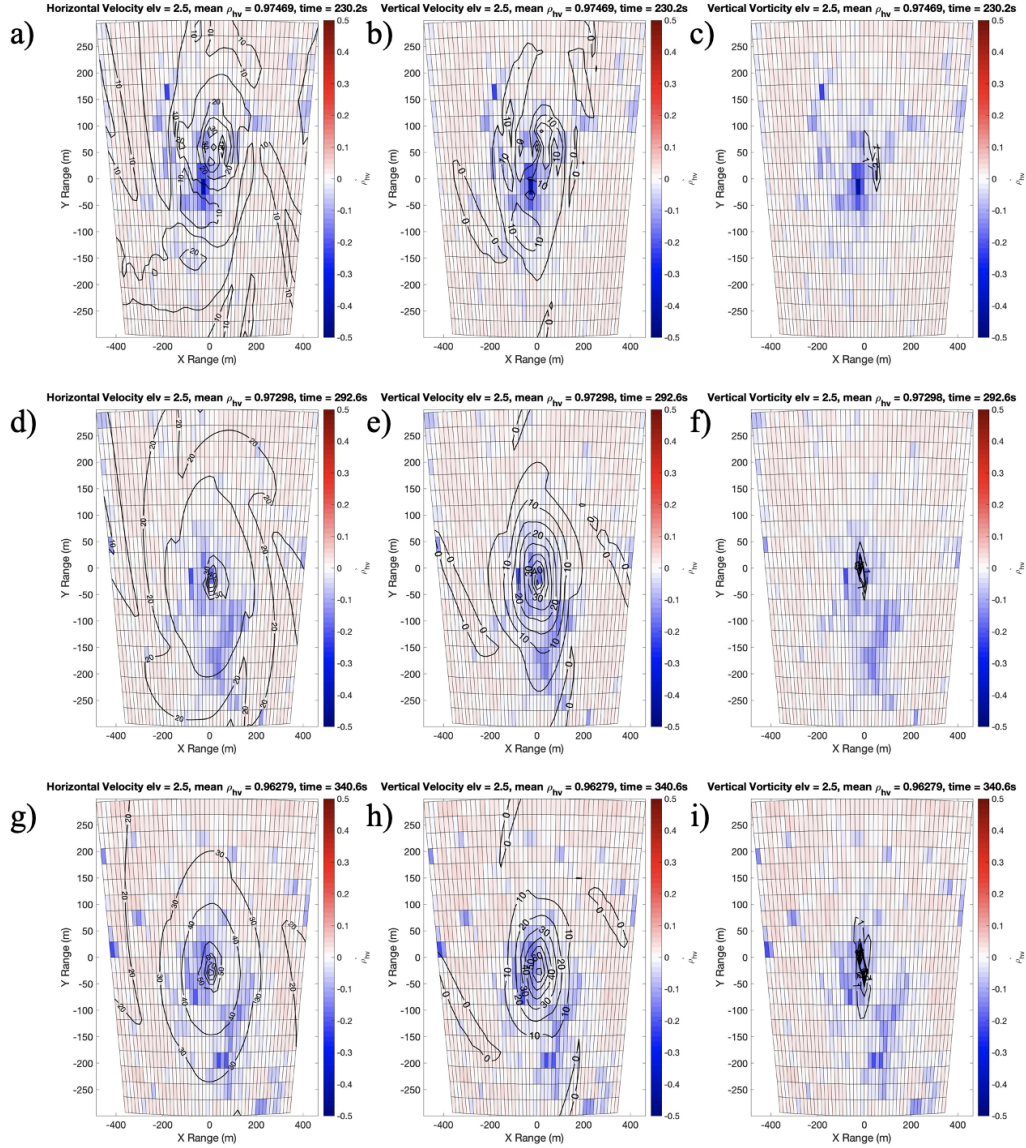
Figure 5.17: PPIs of leaves at an elevation angle of 2.5°. Figs. (a) through (c) are taken at 230.2 s, (d) through (f) are at 292.6 s, and (g) through (i) are at 340.6 s. Black contours, from left to right, are of $V_{h gg}$, W_{gg}, and ζ_{gg}.

away from the 10 ms^{-1} updraft contour. Since this southern lobe is so detached from the updraft, it likely represents debris that has fallen out of the updraft from higher heights. This is different than the debris ejection seen in Kurdzo et al. (2015), where a comma tail of debris formed off of the main TDS from the influence of rear-flank gust front (RFGF) surges. Since the simulations used in this study do not include the parent supercell, the RFGF is not responsible for the features seen in Fig. 5.17.

We can also look at how the area of the TDS evolves over time at an elevation angle of 2.5°. As described in Chapter 3, the TDS area was calculated by filtering out points outside of a 200 m radius from the center of the vortex and only including points with $\rho_{hv} < 0.95$. One of the most notable differences across the three debris types is that the TDS area for the leaves is smaller than that of the metal sheets and woodboards (Fig. 5.18). A possible explanation for this is that the ρ_{hv} values for leaves can exceed 0.95. If the ρ_{hv} threshold was removed, it is possible that the TDS area would increase and more closely resemble that of the other debris types.

The TDS area for leaves increases at about the same time as V_h and W (Figs. 5.18a and 5.18b). As we saw in Fig. 5.17, the shape of the TDS was defined by both the updraft and the horizontal wind. The areal extent of the leaf TDS increases with increases in both the horizontal and vertical velocities as it is the updraft that lofts debris, thus increasing the TDS area at one elevation. After the debris has been lofted, however, some debris falls out of the updraft, thus increasing the TDS area at lower elevations.

Looking at the woodboards, there is a small appendage on the west and south side of the TDS (Fig. 5.19). The western appendage is similar to that seen in Figs.
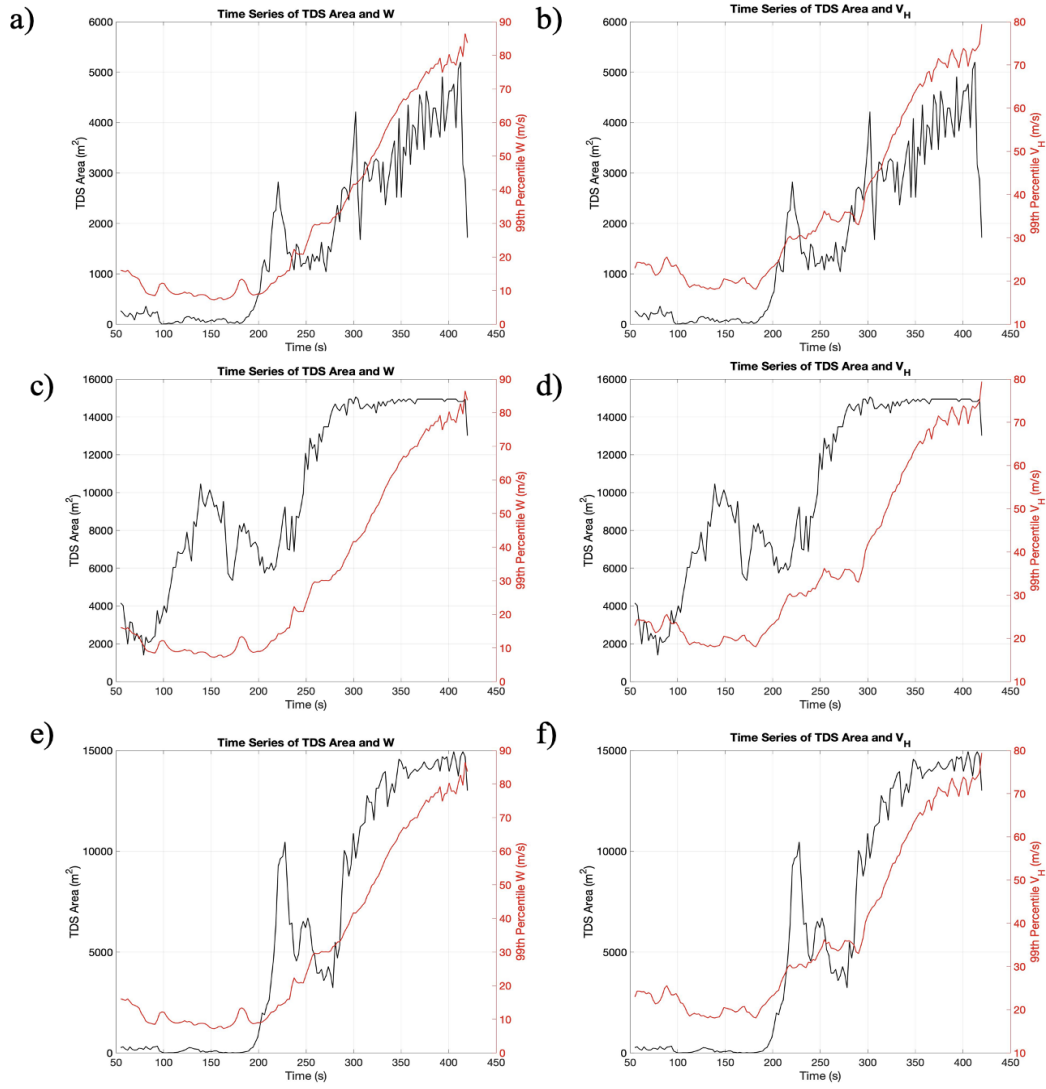
Figure 5.18: Plot of TDS area across time for the stronger tornadogenesis case for (a) and (b) leaves, (c) and (d) woodboards, and (e) and (f) metal sheets.

5.17a - 5.17c, though this appendage does not extend as far to the north. Similarly to the leaf TDS, the western appendage is located near a local maxima in W and right outside the stronger values of V_h. The southern appendage is not co-located with a local-maxima in the updraft speed. Thus, this appendage could be a result of debris being ejected from the vortex.

At 292 s, the updraft of the tornado begins to intensify (Fig. 5.19e). Though, the debris that had previously been lofted by the disorganized updraft in Figs. 5.19a - 5.19c now lies to the south of the newly strengthening updraft. Thus, at 292 s, the TDS is situated to the south of the maximum in both vertical and horizontal wind speeds (Figs. 5.19d and 5.19e). The mean ρ_{hv} values have dropped to 0.79 as more debris has been lofted by the now stronger updraft. At 340 s, the vortex continues to strengthen as seen by the increase in updraft speed and the horizontal velocity (Figs. 5.19g and 5.19h). The areal extent of the 30 ms^{-1} contour for V_h has increased greatly from Fig. 5.19d to Fig. 5.19g. Meanwhile, the area of the TDS has not only increased, but it has also developed into a ring-like shape with higher values of ρ_{hv} in the center. This structure has been seen before in Griffin et al. (2017), though in this study the ring-like structure was evidence of a two-cell vortex. In this simulation, the tornado is a single-cell vortex at 340 s, indicating the ring-like structure might be a by-product of the dynamics of the woodboards.

Quantitatively Figs. 5.18c and 5.18d show how the woodboard TDS evolves along with the intensifying wind field. Overall, the TDS increases as the tornado strengthens. However, initially the TDS area does begin to increase before both W and V_h intensify. This likely means a lower threshold of ρ_{hv} should be used to quantify the
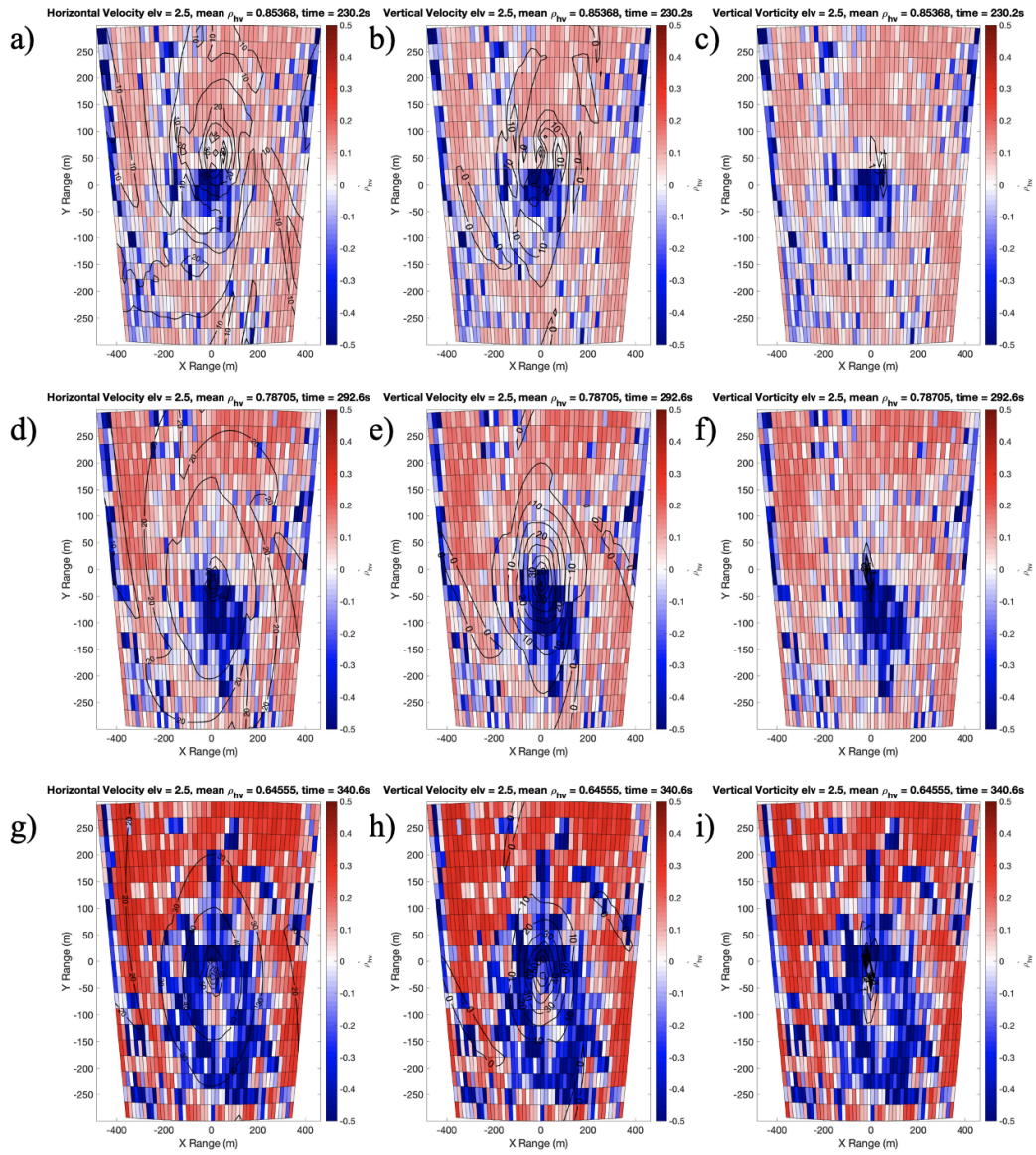
Figure 5.19: Same as in Fig. 5.17, but for woodboards.

71

TDS area for woodboards. At the end of the simulation, the TDS area remains constant. This could be because, while debris was still being lofted, it was also being centrifuged out of the 200 m radius used to calculated the TDS.

Finally, we can look at the same times but for a TDS comprised entirely of metal sheets. At 230 s, there is once again an appendage on the western side of the TDS, though this time it extends much further to the north than either the woodboard or leaf TDS (Figs. 5.20a - 5.20c). Again, the shape of the updraft and the stronger values of V_h on the western side of the vortex are likely responsible for this appendage. At the point where the vortex begins to intensify, the TDS is to the south of the strengthening winds (Figs. 5.20d - 5.20f). The southern shift in the TDS is seen in each debris type, though it is unknown exactly why this is the case.

At 340 s, the TDS resembles that of the previous debris types. That is, it is situated at and to the south of the central updraft (Figs. 5.20h - 5.20i). As the areal extend of the stronger horizontal wind speeds expand from 292 s to 340 s, the TDS widens. Unlike with the woodboard TDS, we do not see higher values of ρ_{hv} at the center of the TDS. The mean ρ_{hv} values are much higher than that of the woodboards as well at the end of the simulation, though they are not as high as what was seen with the leaf TDS.

Looking at Figs. 5.18e and 5.18f, the TDS area for the metal sheets increases with increasing wind speeds. There is a large spike in the TDS area right as the updraft increases. The second drastic increase in TDS area occurs near 270 s. At 292 s – which is near the end of this sharp increase in area – the TDS has been elongated to
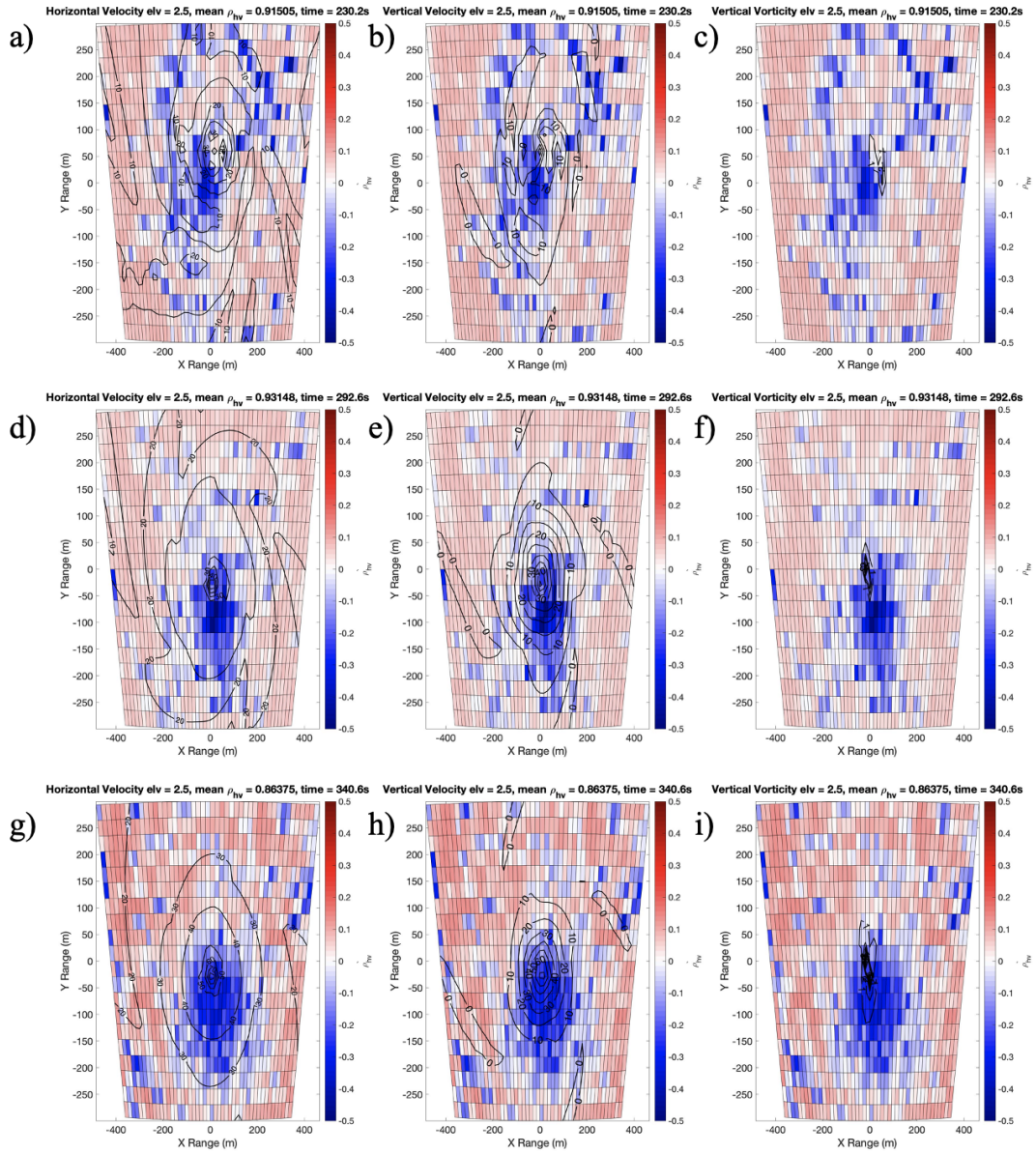
Figure 5.20: Same as in Fig. 5.17, but for metal sheets.

73

the south. This is likely why the TDS area values increased so drastically near this time.

5.2.2 Tornado Dissipation

Figs. 5.21a and 5.21b show the evolution of the TDS area for 100000 leaves. During the first 450 s of the simulation, the area decreases in tandem with V_h. However, it is when W begins to rapidly weaken where we see the TDS area begin to drastically change (Fig. 5.21a). In fact, between 600 and 800 s, the updraft strengthens again, causing the TDS area to increase. We can see this visually in Fig. 5.22. At 220 s, the TDS is situated at the central downdraft and in the middle of multiple vorticies (Figs. 5.22a - 5.22c). Jumping forward to 508 s, the mean ρ_{hv} has increased to 0.98 (Figs. 5.22d - 5.22f). This means that less points are considered as a part of the TDS given the 0.95 threshold used. We also see that the TDS is more organized, likely due to the presence of only one vortex versus the multiple vorticies in Fig. 5.22c. Finally, looking at when the updraft increases at the end of the simulation, the TDS has expanded in size as more debris has been lofted (Figs. 5.22g - 5.22i). Since the leaf TDS area responds so quickly and directly to changes in the updraft, light debris are very sensitive to small changes in the updraft intensity. The horizontal wind speed also plays a roll in dictating the size of the TDS area, but it appears that the updraft is what causes the more drastic changes.

Unlike with the leaves, we do not see the early correlation between the initial decrease of V_h and the TDS area (Fig. 5.21d). In fact, the TDS area is completely constant until just after W begins to weaken (Fig. 5.21c). The updraft weakens by

Figure 5.21: Plot of TDS area across time for the tornado dissipation case for (a) and (b) leaves, (c) and (d) woodboards, and (e) and (f) metal sheets.
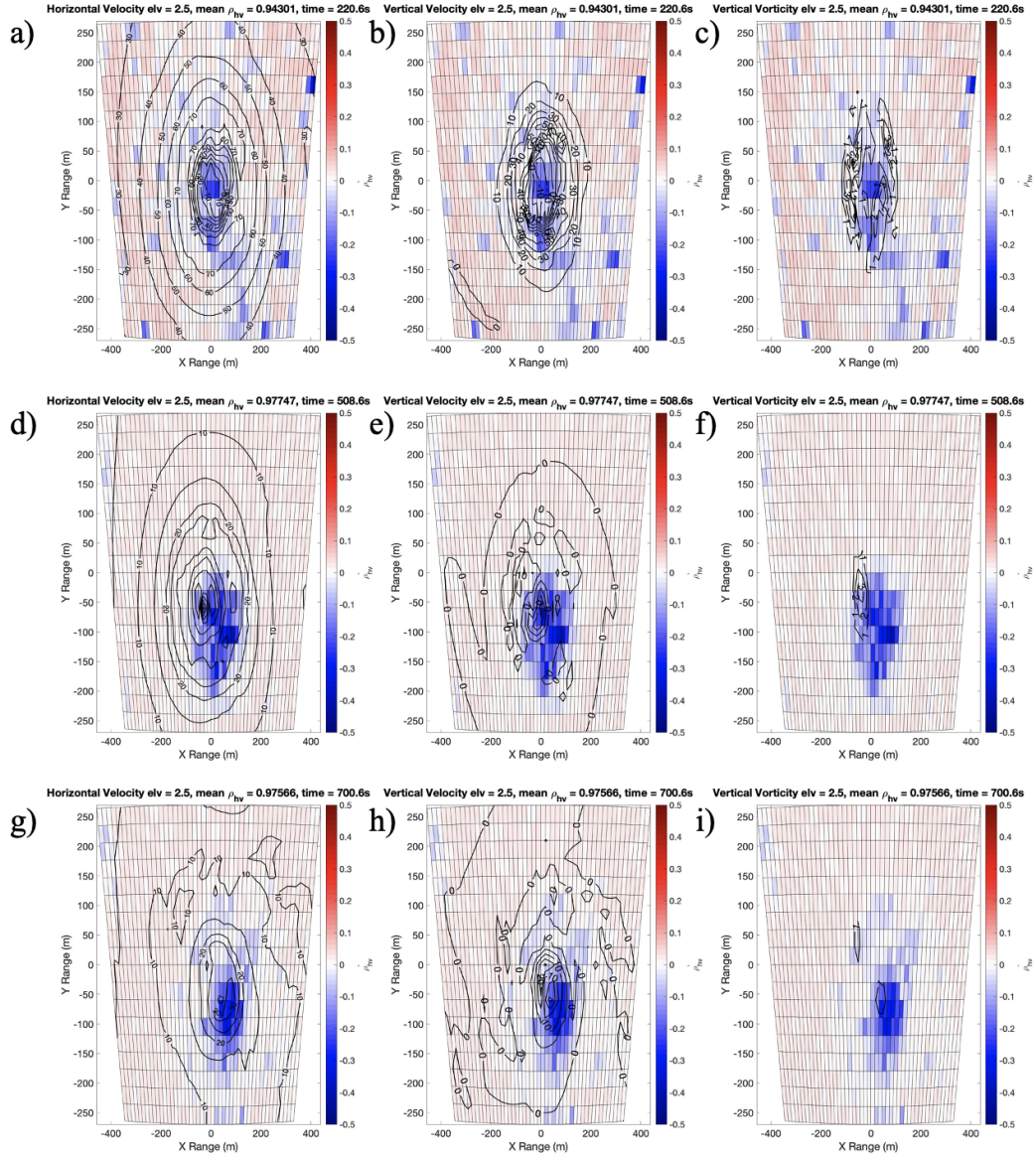
Figure 5.22: PPIs of leaves at an elevation angle of 2.5°. Figures (a) through (c) are taken at 230.2 s, (d) through (f) are at 292.6 s, and (g) through (i) are at 340.6 s. Black contours, from left to right, are of V_{hgg}, W_{gg}, and ζ_{gg}.
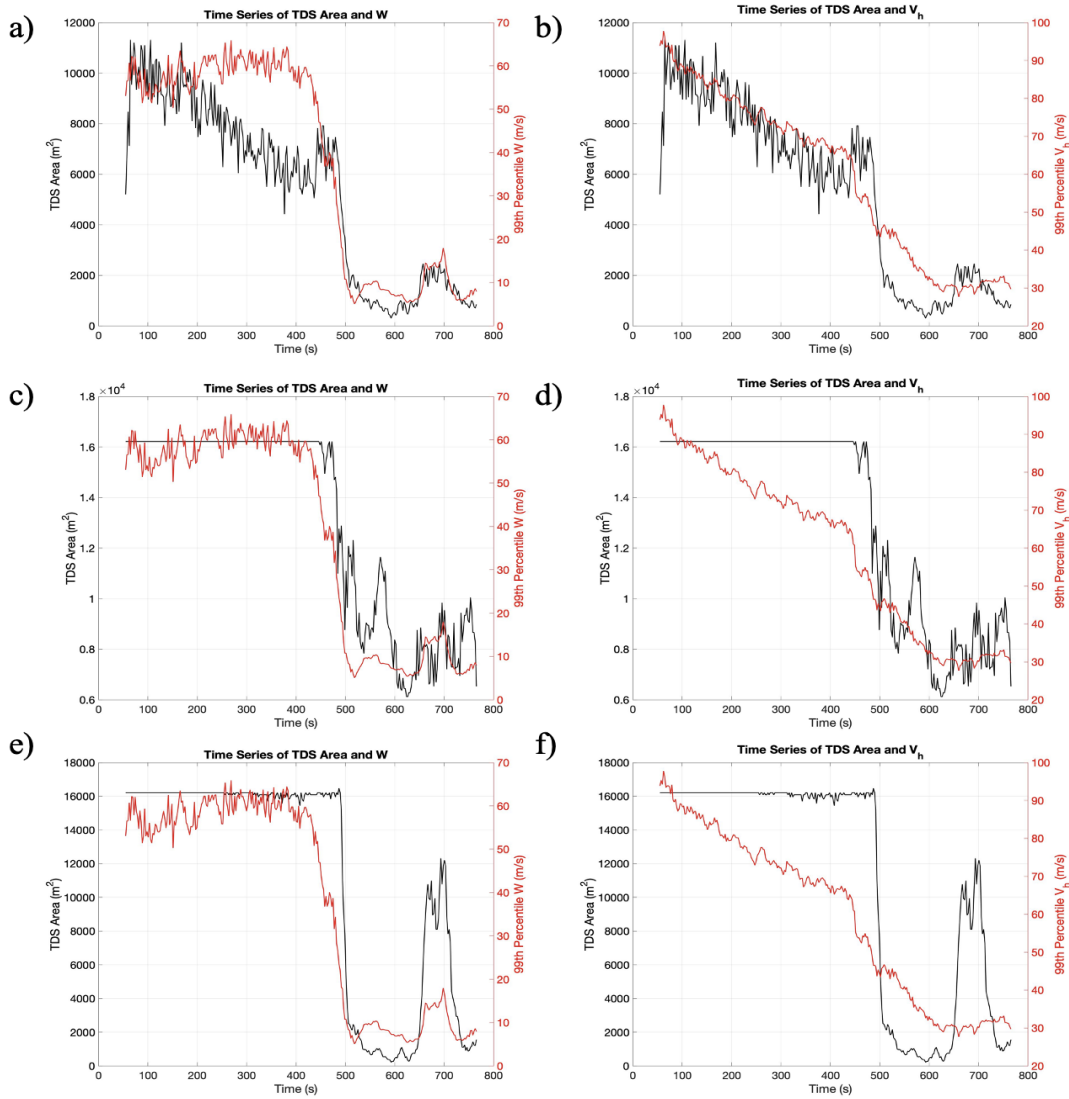
about 20 ms^{-1} before the woodboard TDS area drastically decreases. Thus, the value of W required to keep woodboards at an elevation angle of 2.5° is approximately 40 ms^{-1}. At the end of the simulation, the values of the TDS area become more noisy. This is likely due to complications of debris fallout from higher elevation angles.

Visually, we see the TDS at 220 s have a ring-like shape as seen at the end of the strong tornadogenesis simulation (Figs. 5.23a - 5.23c). This ring is situated outside of the 70 ms^{-1} contour for V_h and lies to the outside of each sub-vortex. At 508 s, the area has significantly decreased and the effects of centrifuging are still present (Figs. 5.23d - 5.23f). Finally, towards the end of the simulation, the TDS area continues to decrease. However, there is debris fallout to the southeast of the main TDS, thus increasing the TDS area despite the main TDS decreasing in size (Figs. 5.23g - 5.23i). Comparing Figs. 5.23d and 5.23g, we do not see the main TDS size increasing, meaning the woodboard TDS does not respond to the increase in the updraft that occurs at about 700 s into the simulation. Unlike the leaf TDS, this could mean that woodboards are less sensitive to small changes in the updraft intensity.

The pattern for the metal sheet TDS area is similar to that of the woodboards. The area remains constant until W decreases (Fig. 5.21e). What is slightly different is the delay between the decrease in W and the decrease in the TDS area. For the woodboard TDS, the decrease in the TDS area occurred slightly sooner to when W began to decrease than the metal sheet TDS. Between 600 and 800 s when W intensifies, the TDS area for metal sheets increases drastically. The metal sheets thus seem to be very sensitive to changes in W.
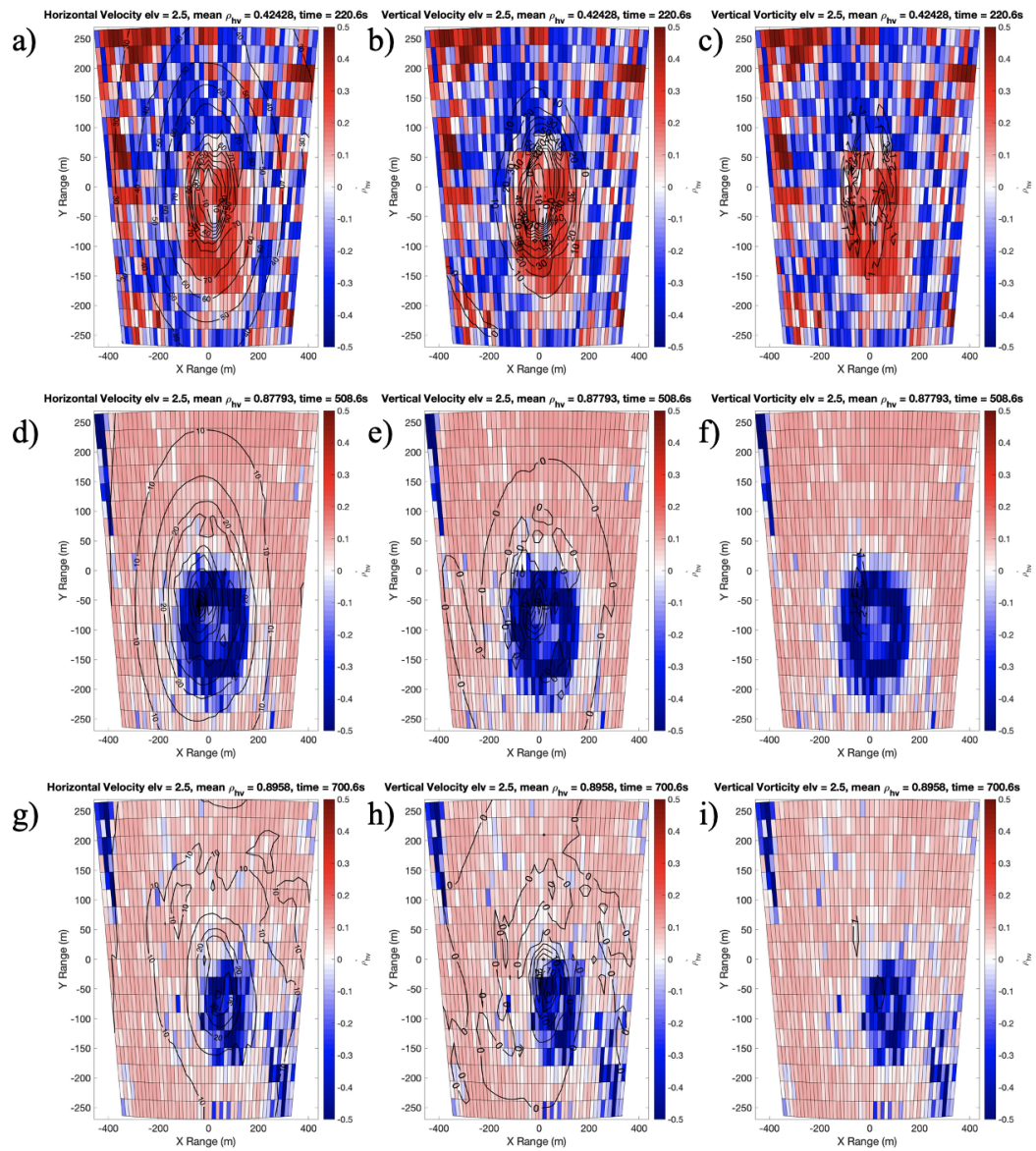
Figure 5.23: Same as in Fig. 5.22, but for woodboards.
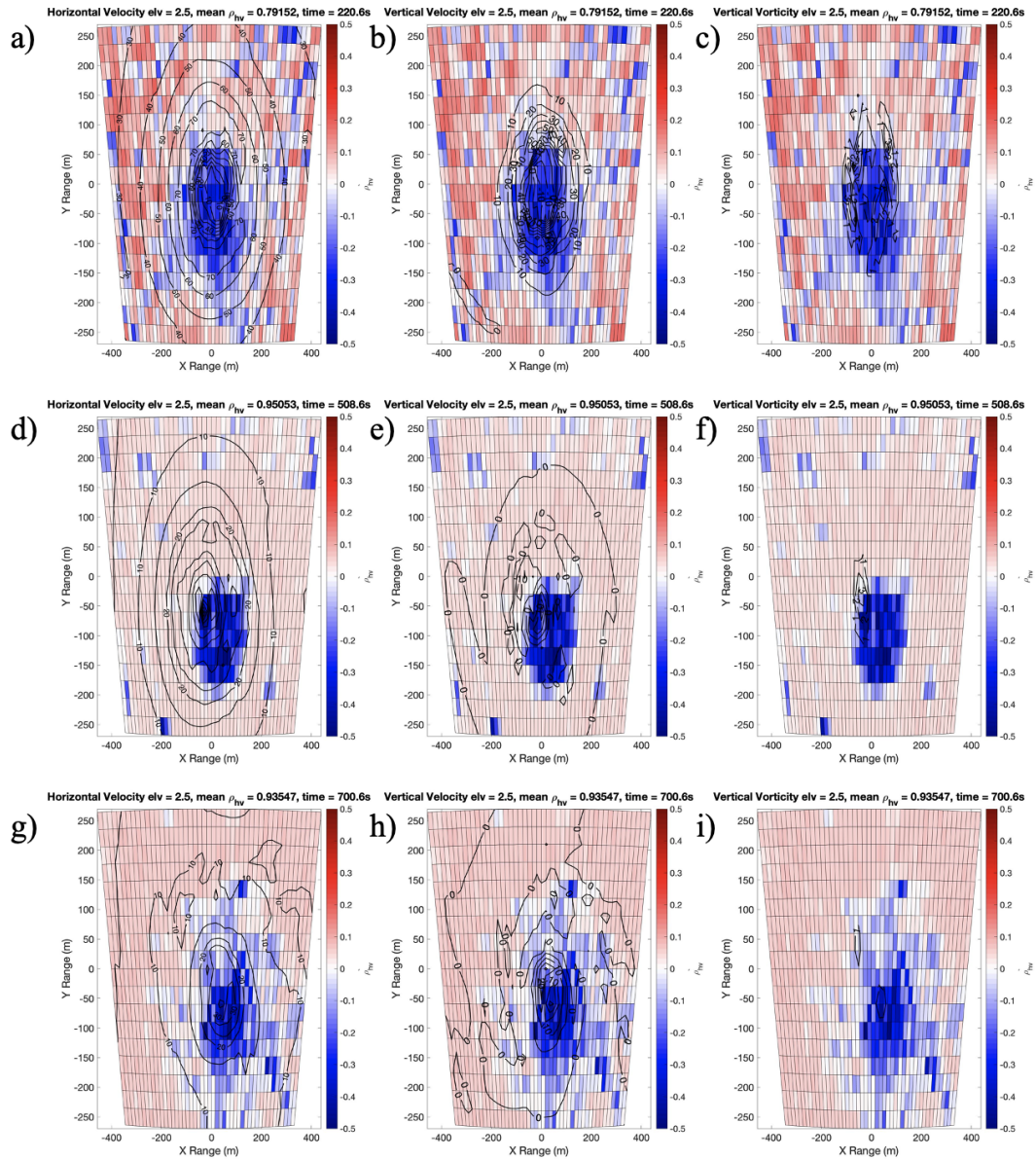
Figure 5.24: Same as in Fig. 5.22, but for metal sheets.

To visually see the TDS area development for the metal sheets, PPIs are plotted in Fig. 5.24. At 220 s, we see the TDS primarily bounded by the 20 ms^{-1} W contour and 70 ms^{-1} V_h contours (Figs. 5.24a and 5.24b). There is not a ring-like shape to the TDS, indicating debris is not being centrifuged by the vortex as strongly as the woodboards. As the updraft weakens, the TDS area shrinks and shifts to the southeast (Figs. 5.24d - 5.24f). Finally, at 700 s the updraft briefly intensifies, lofting more debris and causing the TDS area to increase. The TDS is much more disorganized than before, with debris existing in regions with no updraft and weak horizontal velocities (Figs. 5.24g and 5.24h).

5.3   Vertical Development of the TDS

5.3.1   Tornadogenesis

Fig. 5.25 provides a look at the vertical structure of the TDS at the onset of tornado-genesis for each debris type. Each TDS is located near the developing updraft, which is at about 100 m along the y-axis. The metal sheets are initially lofted the highest and each TDS is situated on the right side of the vortex within the 30 ms^{-1} contour of V_h.

The woodboard TDS has the lowest values of ρ_{hv}, with a semi-circle of very low ρ_{hv} values with higher ρ_{hv} values within the half circle. There are also lower points of ρ_{hv} located across the lowest height in Figs. 5.25c and 5.25d. This is so because, for the woodboards, most of the debris would not initially be lofted by the vortex, leaving debris lying at the bottom of the simulation. An elevation angle of 2.5° was chosen

80
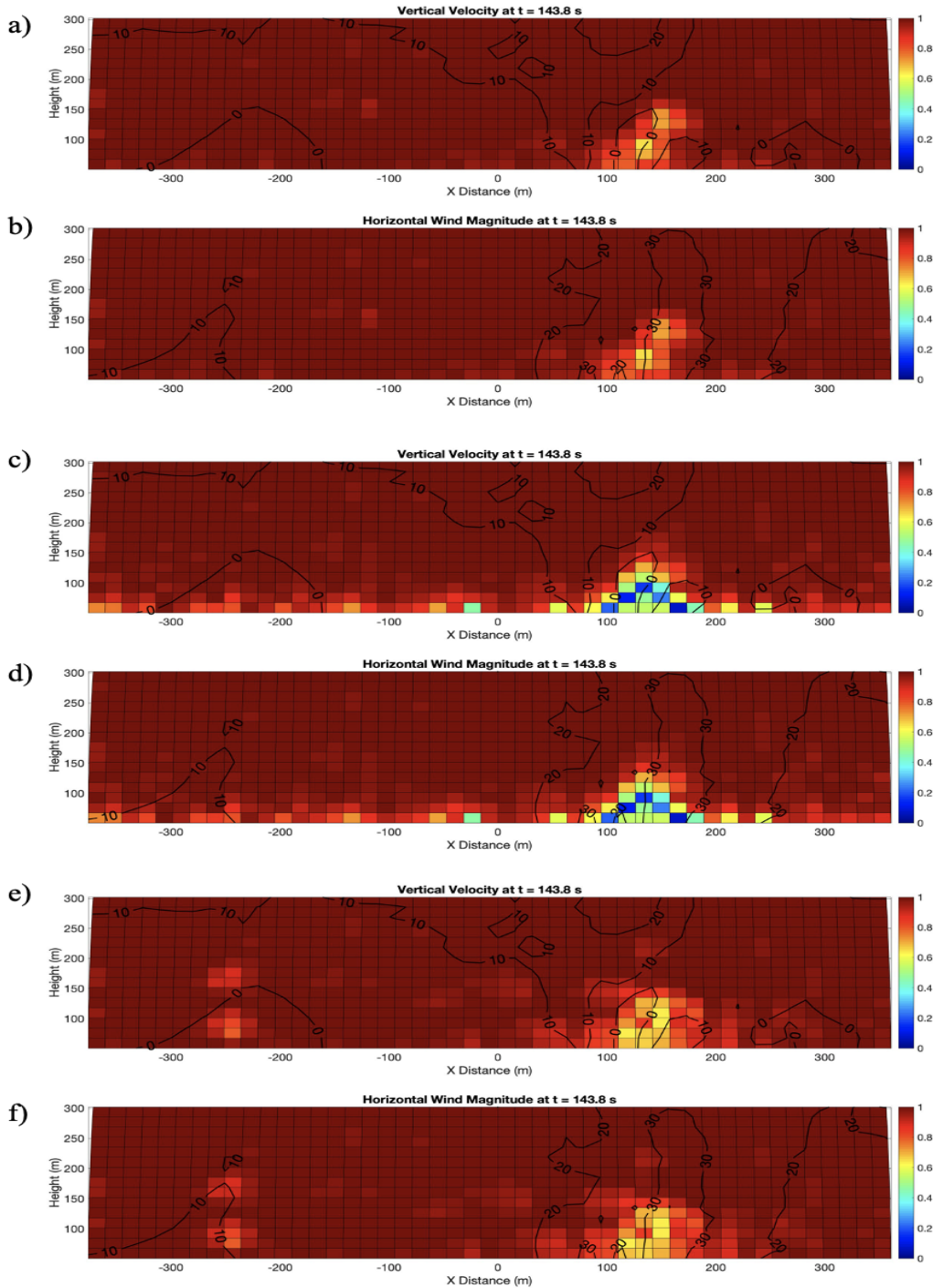
Figure 5.25: Vertical cross sections through the center of the tornado taken along the x-axis. All cross sections are taken at a time of 143 s into the weak tornadogenesis simulation. The leaf TDS is shown in (a) and (b), the woodboards TDS is shown in (c) and (d), and the metal sheet TDS is shown in (e) and (f). Black contours are values of (a), (c), and (e) vertical velocity in ms^{-1} and (b), (d), and (f) horizontal wind speed in ms^{-1}.

as the lowest tilt to try and avoid retrieving data from the motionless debris lying on the ground. Meanwhile, the metal sheet and leaf TDS have the lowest ρ_{hv} values in the center of the TDS. The metal sheet TDS is much wider than the leaf TDS. In fact, the leaf TDS is the smallest TDS of all the debris types at the beginning of the simulation.

At the end of the simulation when the tornado has strengthened and split into multiple vorticies, each TDS has increased in size. Starting with the leaves, the ρ_{hv} values are generally the highest out of each debris type (Figs. 5.26a and 5.26b). The TDS itself has a v-like shape, with the lower values of ρ_{hv} lying within the maximum updraft and within the strongest gradient of V_h. There are also lower ρ_{hv} values outside the maximum updraft. This is likely debris that has been centrifuged out from the vortex and is now falling back down to the ground. Overall, the TDS is rather diffuse in nature, with a TDS that is not overly well-defined and concentrated at one specific location.

The woodboard TDS also has this same v-like shape, though the TDS is much more defined and wider than the leaf TDS (Figs. 5.26c and 5.26d). Since woodboards are heavier than the leaves, they will fallout of the vortex faster, hence why the woodboard TDS is so much wider than the other debris types. Lower values of ρ_{hv} are much closer in space to the maximum updraft and V_h than with the leaf TDS. There is also some debris fallout, especially on the left side of the domain. However, there is much less debris being lofted from the concentrated TDS as seen with the leaf TDS.

Finally, the metal sheet TDS once again has the v-like shape as seen with the other debris types (Figs. 5.26e and 5.26f). This shape is indicative of debris being

a)

b)

c)

d)

e)

f)
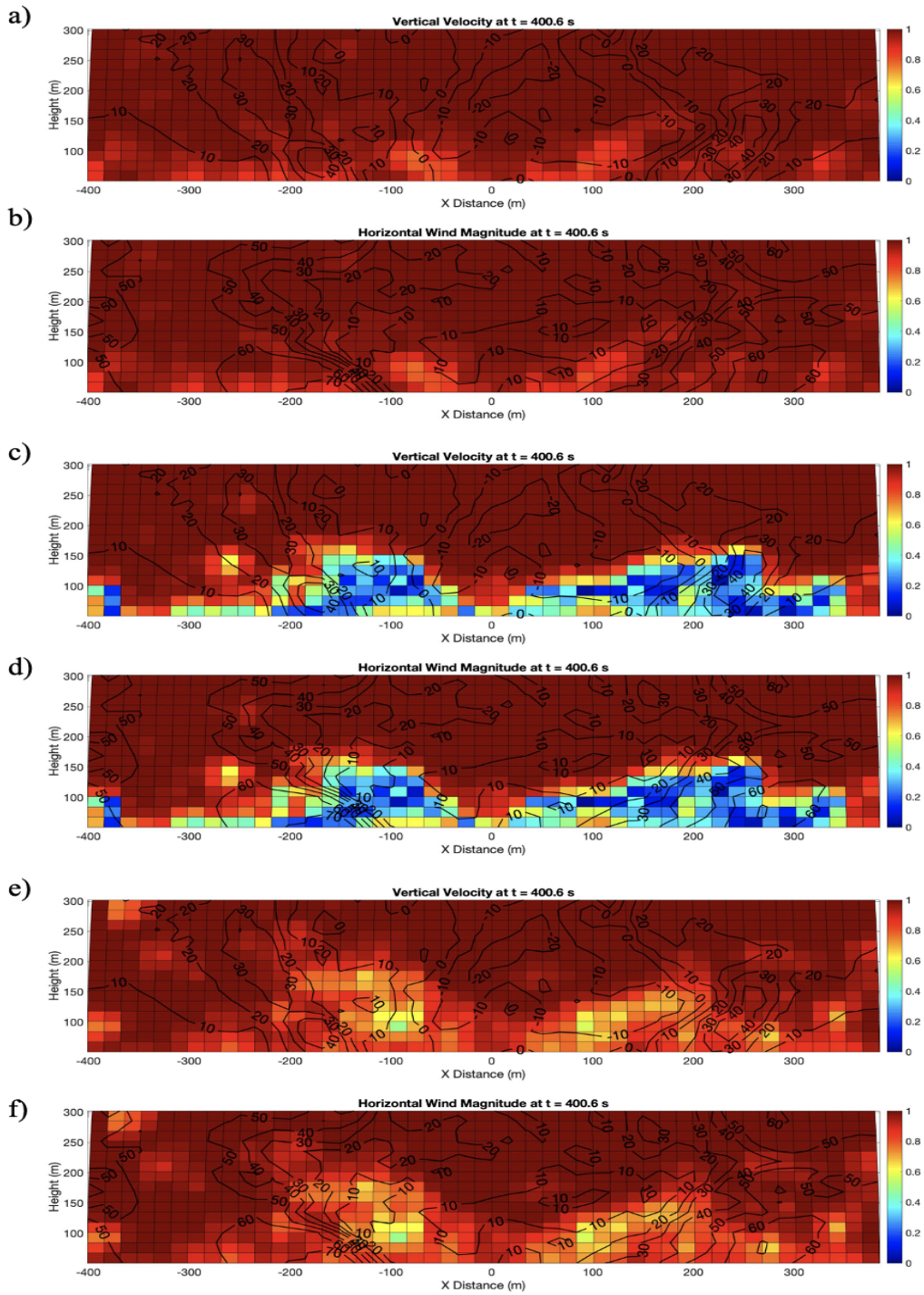
Figure 5.26: Same as in Fig. 5.25, but taken at a time of 401 s.

centrifuged away from the center of the vortex. Like at the beginning of the simulation, the metal sheet TDS reaches the highest elevation angle. The TDS mostly lies within the maximum updraft and the maximum in V_h. The TDS is also much more diffuse than the woodboard TDS, resembling the leaf TDS other than the values of ρ_{hv}.

To quantify the vertical statistics of each TDS, 10th percentile ρ_{hv} and 90th percentile Z_H were taken at each height for each debris type and plotted in Fig. 5.27. The two times analyzed are the same times shown in Figs. 5.25 and 5.26. As can be seen at 143 s, ρ_{hv} for the woodboards reaches the lowest values near the ground (Fig. 5.27a). However, ρ_{hv} for the metal sheets remains relatively low up to a height of 150 m while the other two debris types increase much more rapidly with height, indicating the metal sheet TDS reaches the highest height. This decrease of ρ_{hv} with height has been seen in previous studies (e.g., Bodine et al. (2014)). The woodboard TDS has the most change in ρ_{hv} values at 401 s while the leaf TDS has the least amount of change throughout the simulation (Fig. 5.27c). Each TDS increases with height as the vortex intensifies, though the metal sheet TDS has the highest TDS height. This means that ρ_{hv} values at higher heights in the TDS are more likely to be dominated by lighter debris types.

For the Z_H values, they are remarkably similar at the beginning of the simulation (Fig. 5.27b). The values slightly decrease with height, though they do not change by more than 3 dBZ. At the end of the simulation, Z_H decreases more with height for each debris type (Fig. 5.27d). There is also more distinction between debris types in the Z_H values near the ground, though the difference is still small. The woodboards

Figure 5.27: Vertical distribution of polarimetric statistics for 10th percentile ρ_{hv} at (a) 143 s and (c) 401 s and 90th percentile Z_H at (b) 143 s and (d) 401 s for each debris type in the weaker tornadogenesis simulation.
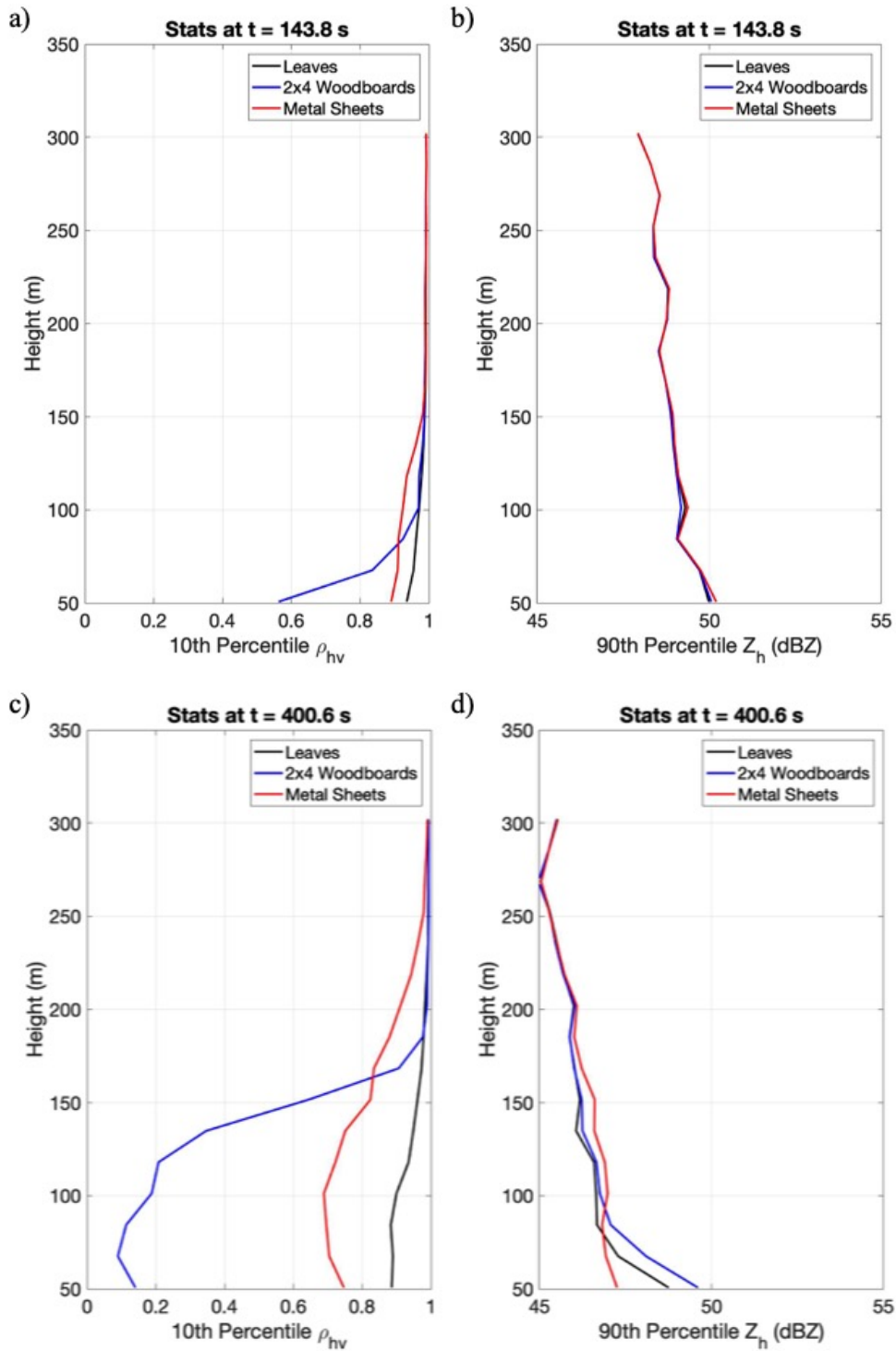
have the largest Z_H values at the surface with the metal sheets having the smallest values. The metal sheet TDS also experiences the least amount of change in Z_H with height at the end of the simulation. Overall, this trend of consistent Z_H values across debris types was also seen in the horizontal evolution of 90th percentile Z_H for each TDS, meaning that Z_H does not change drastically in the vertical or horizontal for different debris types.

Visually, the evolution of the vertical statistics of the TDS over time is given in Figs. 5.28, 5.29, and 5.30. Starting with the leaf TDS, ρ_{hv} drops to about 0.85 (Fig. 5.28a). The Z_H values generally decrease with height, though the values do not change by more than about 5 dBZ throughout the entire simulation (Fig. 5.28b). There is an apparent "gradient" in Z_H between 125 s and 170 s. It is unknown why this "gradient" occurs, though it should be noted that Z_H does not change by more than 3 dBZ during this time interval. The same sharp change in Z_H is also seen in Figs. 5.2, 5.4, and 5.6 in the first third of the simulation. Finally, Z_{DR} values are mostly 1.0 with little change across height and time (Fig. 5.28c).

The woodboard TDS has very low values of ρ_{hv} near the ground (Fig. 5.29a). Somewhat surprisingly, the height of the woodboard and leaf TDS seem to be similar, with the leaf TDS height being slightly larger. The similarity in TDS height is likely due to the weak vertical velocities in this tornadogenesis simulation. The Z_{DR} values for the woodboard TDS reach lower, positive values where ρ_{hv} is at or less than 0.2 (Fig. 5.29c). Again, Z_H is very similar between the leaf and woodboard TDS aside from the very lowest height where Z_H is higher for the woodboards (Fig. 5.29b).
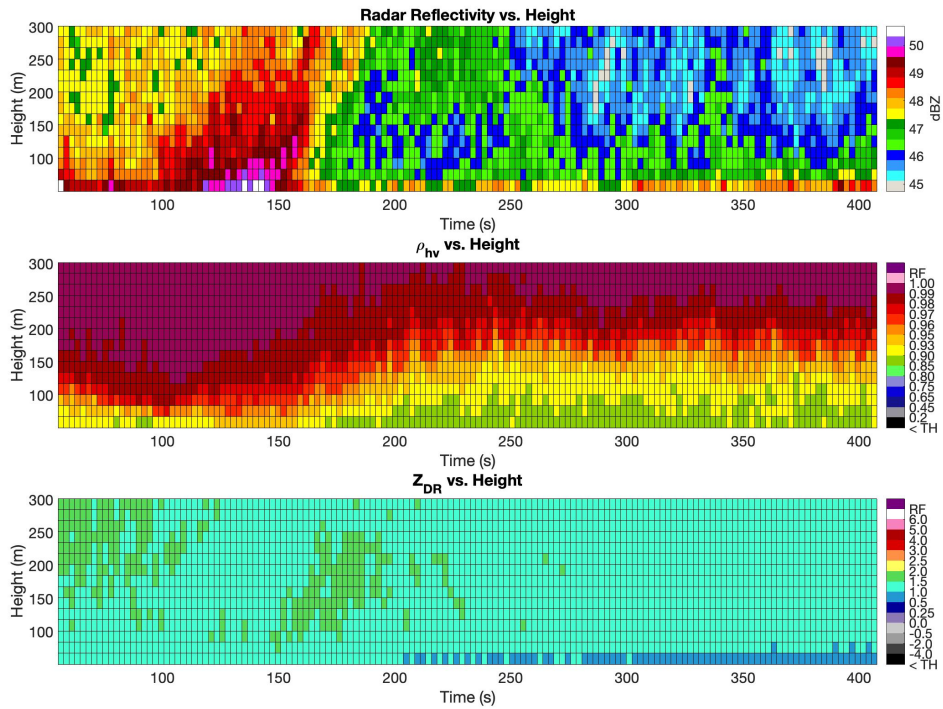
Figure 5.28: Time versus height plot of the vertical statistics of (a) Z_H, (b) ρ_{hv}, and (c) Z_{DR} for the weaker tornadogenesis simulation for leaves.

The metal sheet TDS reaches the highest height with ρ_{hv} values lower than the leaf TDS but higher than the woodboard TDS (Fig. 5.30a). For each TDS, the height remains constant from 200 s to the end of the simulation. Thus, the TDS height seems to have the most variance during the beginning of tornadogenesis. Similar to the leaf TDS, Z_{DR} values are mostly 1.0, with slightly lower values towards the end of the simulation at the lowest heights (Fig. 5.30c).

5.3.2 Strong Tornadogenesis

Compared to the weaker tornadogenesis simulation, the TDS in the stronger tornadogenesis simulation does not form until much later into the simulation (at about 290
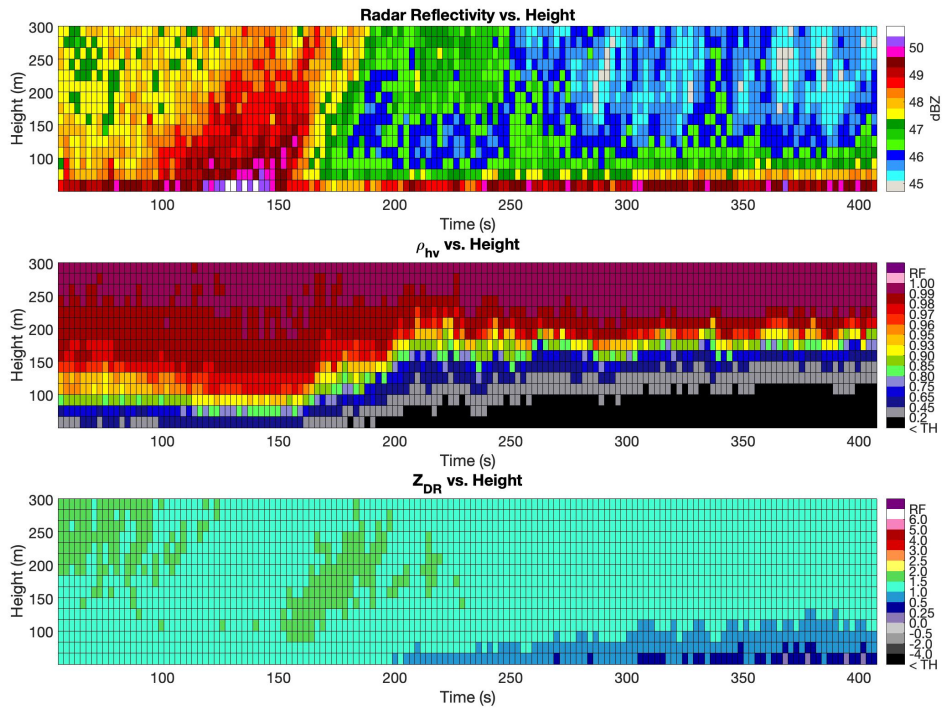
Figure 5.29: Same as in Fig. 5.28, but for woodboards.

s). At 328 s into the simulation, the TDS width is bounded by the 10 ms^{-1} W and 40 ms^{-1} V_h contours (Figs. 5.31a and 5.31b). Debris is being lofted by the higher than the rest of the TDS at the center of the domain by the 70 ms^{-1} updraft. Once lofted, debris traverses to the right of the TDS, as hinted at by the lower values of ρ_{hv} coming off of the right of the TDS. Looking at the TDS at the same time, but now along the y-axis, we see debris falling to the south of the TDS (Figs. 5.32a and 5.32b). This is the opposite side of the TDS as the maximum in W.

At 381 s, the TDS has widened and grown as W as intensified and a central downdraft begins to be induced (Figs. 5.31c and 5.32c). Along the x-axis, there are now hints of the debris arch, with higher values of ρ_{hv} near the center of the domain
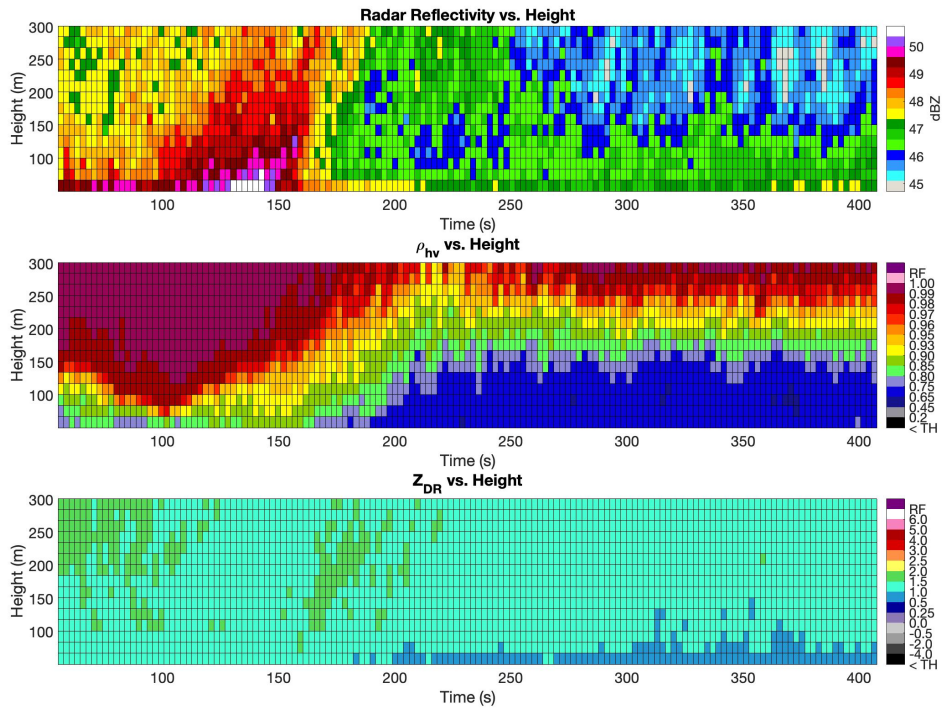
Figure 5.30: Same as in Fig. 5.28, but for metal sheets.

near the ground with an arch of lower ρ_{hv} over this region of higher ρ_{hv}. This region of higher values of ρ_{hv} is co-located with the maximum in W, indicating that the strong updraft near the surface is lofting debris into this arch-like formation. Along the y-axis, the maximum in W (the 80 ms^{-1} contour) is not located in the column of higher ρ_{hv} values (Fig. 5.32c). This column of higher ρ_{hv} values continues to grow. In fact, the arch-like structure in ρ_{hv} has exceeded the top of the domain at which data was collected.

Near the end of the simulation, the arch-like structure appears more prominently along the x-axis (Figs. 5.31e and 5.31f). Looking along both the x- and y-axis, the fallout from the TDS is more eastward and southward (Figs. 5.31d and 5.32d). At the
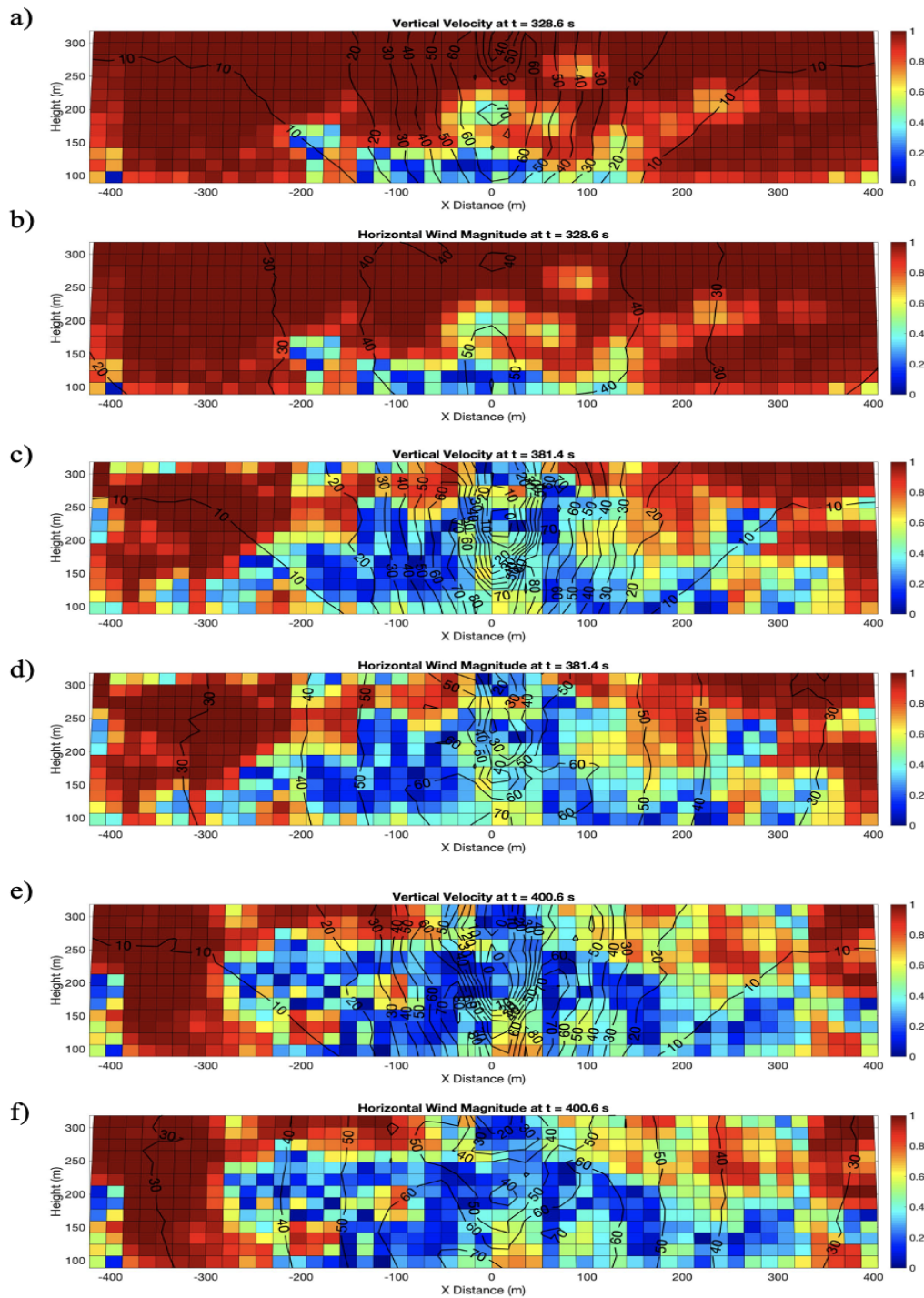
Figure 5.31: Vertical cross sections through the center of the vortex along the x-axis. The debris type plotted is woodboards at (a) and (b) 329 s, (c) and (d) 381 s, and (e) and (f) 401 s. Black contours are values of (a), (c), and (e) vertical velocity in ms^{-1} and (b), (d), and (f) horizontal wind speed in ms^{-1}.

eastern edge of the higher ρ_{hv} column is the downdraft. This arch-like structure has been seen in observations by Wakimoto et al. (2015). In their paper, they referred to this debris arch as a "debris overhang" with a notch of higher ρ_{hv} that was co-located with the tornado's updraft. Wakimoto et al. (2015) hypothesized that the updraft was lofting small debris to produce this overhang.

Looking at the vertical distribution of 10th percentile ρ_{hv} and 90th percentile Z_H, we see that at 290 s, ρ_{hv} looks very similar to the latter end of the weaker tornado-genesis simulation (Fig. 5.33a). Values of ρ_{hv} increase with height while Z_H values are relatively constant (Figs. 5.33a and 5.33b). As the simulation progresses, the vertical profile of ρ_{hv} no longer converges at a value of 1 at higher heights. Instead, ρ_{hv} decreases throughout the entire profile (Fig. 5.33c). Values of Z_H are higher at the surface, though are still relatively consistent past a height of 150 m (Fig. 5.33d). Finally, near the end of the simulation, the entire profile homogenizes as ρ_{hv} values are consistently low throughout the profile (Fig. 5.33e). Meanwhile, Z_H decreases with height (Fig. 5.33f).

Looking at Fig. 5.34, the evolution of the vertical statistics of the TDS across the entire simulation is shown. The updraft begins to increase around 200 s (see Fig. 5.8). About 50 seconds afterwards, the 90th percentile ρ_{hv} begins to decrease more with height (Fig. 5.34b). The height of the TDS is much larger compared to the woodboard TDS in the weaker tornadogenesis simulation. The Z_H values also reach slightly higher values than the weaker tornadogenesis case, though this could be due to the increase in debris concentration from 10000 to 100000 rather than the stronger updraft (Fig. 5.34a).
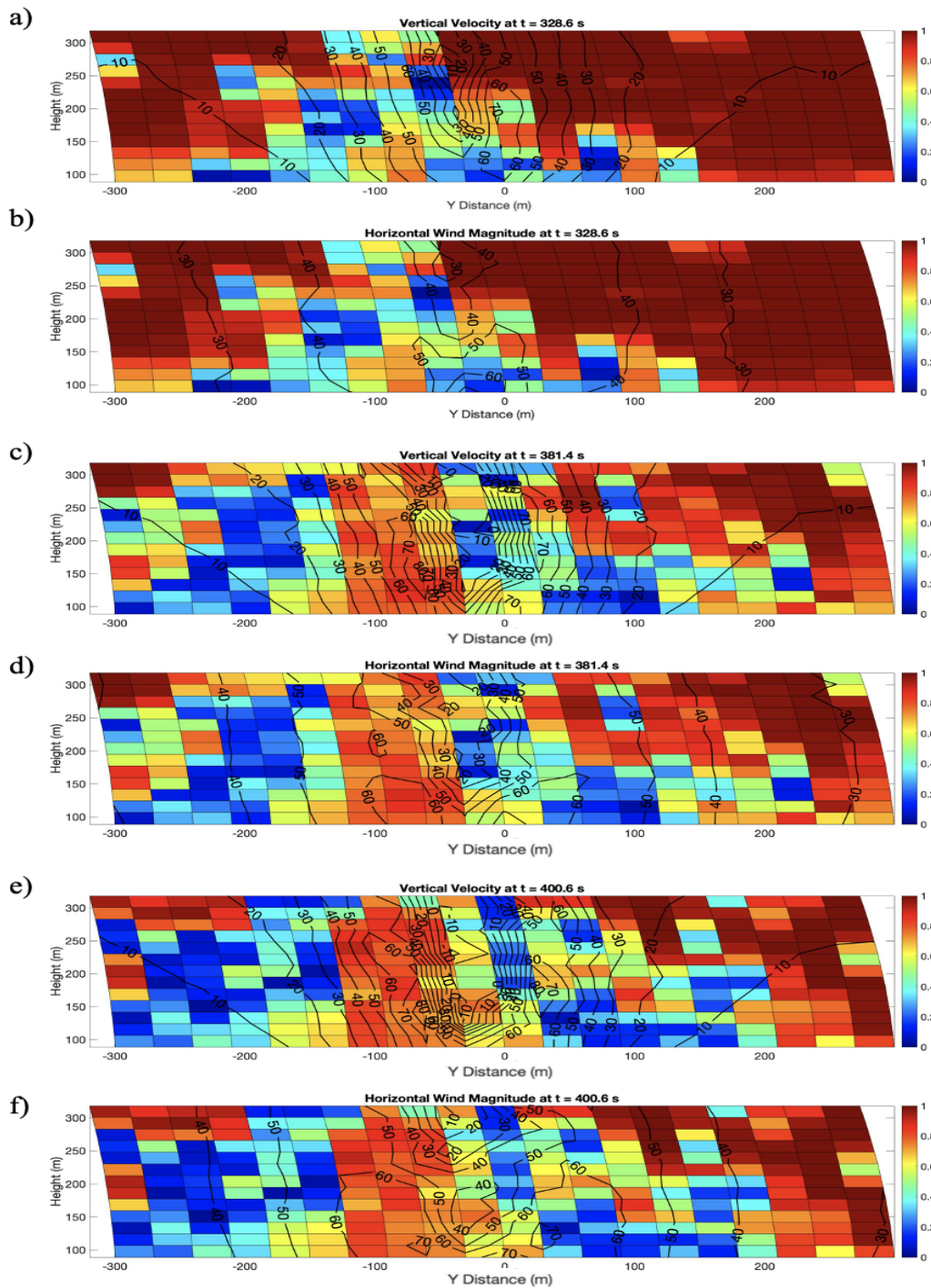
Figure 5.32: Same as in Fig. 5.31, but cross sections are taken along the y-axis.
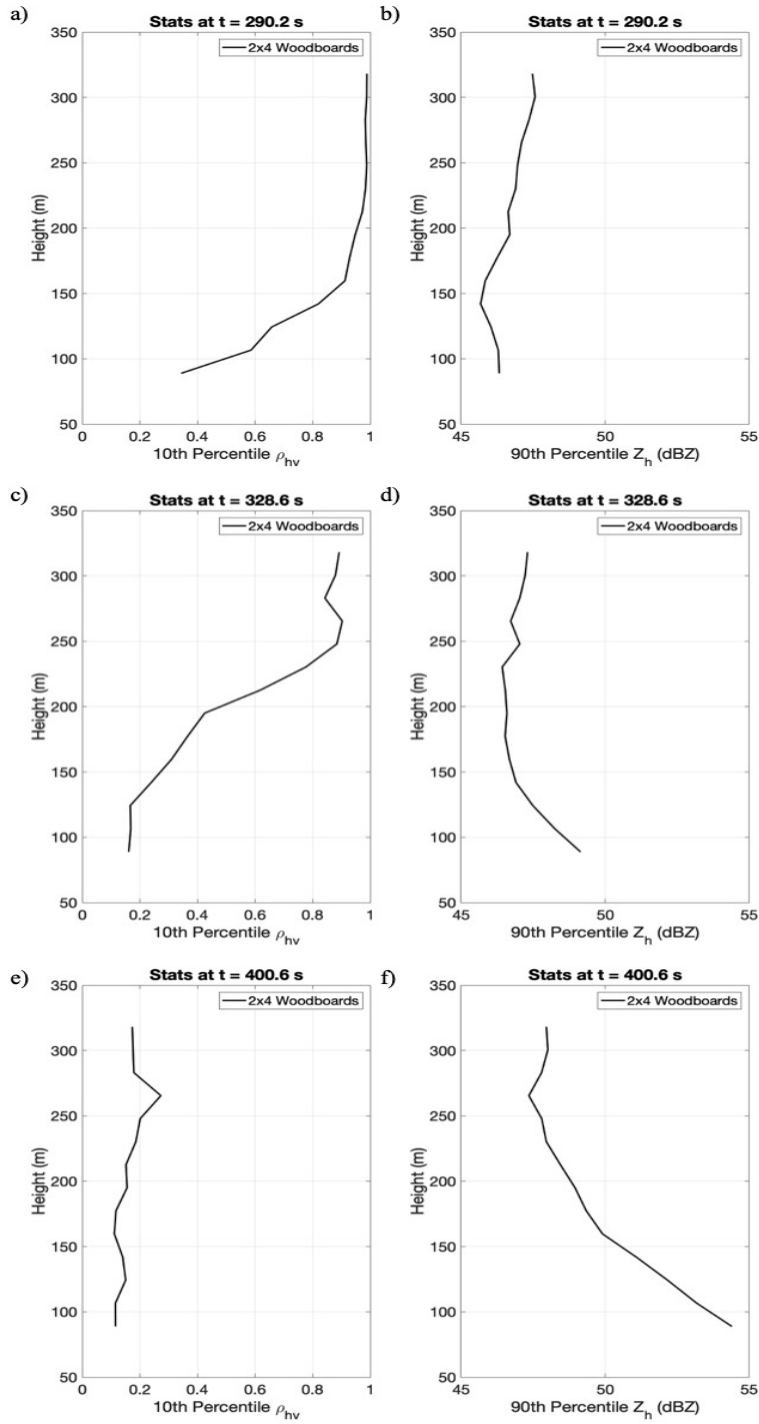
Figure 5.33: Vertical distribution of polarimetric statistics for 10th percentile ρ_{hv} at (a) 290 s, (c) 328 s and (e) 401 s and 90th percentile Z_H at (b) 290 s, (d) 328 s and (f) 401 s for woodboards in the stronger tornadogenesis simulation.
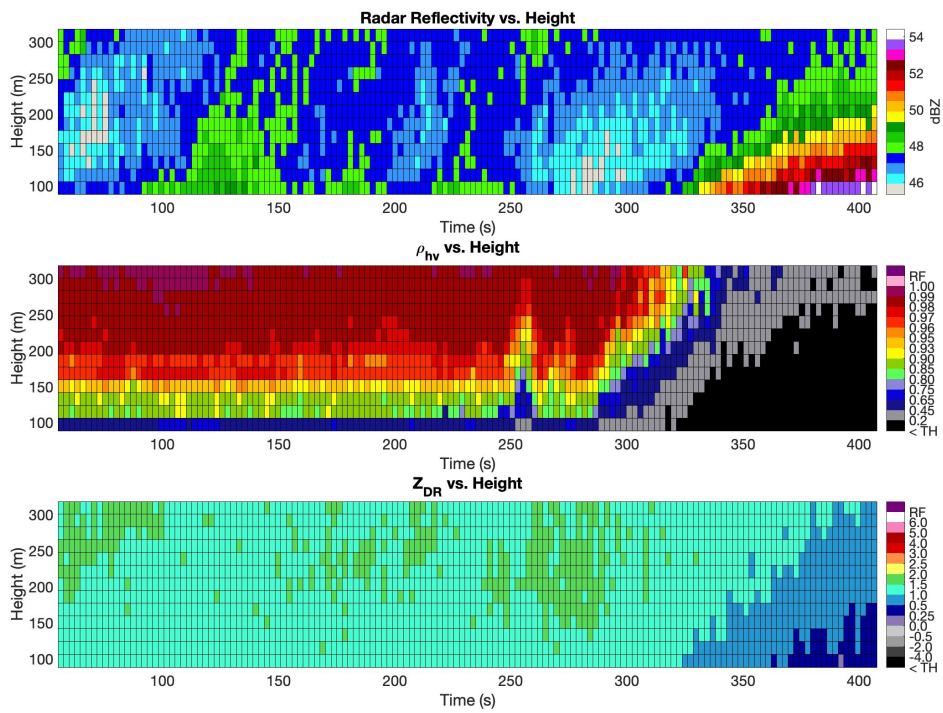
Figure 5.34: Time versus height plot of the vertical statistics of (a) Z_H, (b) ρ_{hv}, and (c) Z_{DR} for the stronger tornadogenesis simulation for woodboards.

Chapter 6

Conclusion and Future Work

Since the TDS provides both confirmation of the presence of a tornado and information about the damage that is occurring, it is a feature on radar that provides useful information to forecasters. In this project, relationships between debris characteristics, such as debris size, type, and concentration, polarimetric variables, and the three-dimensional tornadic wind field were analyzed using both a single volume emulator and a dual-polarimetric radar simulator called SimRadar. Using this simulation-based framework, past hypotheses about the TDS were analyzed using different debris types, sizes, and concentrations. A list of these hypothesises and whether or not they were confirmed by the results of this study are given in Table 6.1.

Table 6.1: Table of TDS hypotheses from past work and whether or not the results of this study support these past theories. Results that are strongly supported are seen across different debris types and/or simulations while results that are conditionally supported are seen only in certain debris types and/or simulations.

TDS Hypotheses	Findings
As debris size increases, ρ_{hv} will decrease	Conditionally Supported
As debris size increases, Z_H will increase	Strongly Supported
As debris concentration increases, ρ_{hv} will decrease	Conditionally Supported
As debris concentration increases, Z_H will increase	Strongly Supported
As a tornado intensifies, ρ_{hv} will decrease	Strongly Supported
As a tornado intensifies, Z_H will increase	Conditionally Supported
As a tornado intensifies, the TDS area will increase	Strongly Supported
As a tornado intensifies, the TDS height will increase	Conditionally Supported

It has been hypothesized that, as debris size increases, ρ_{hv} will decrease and Z_H will increase (Bodine et al. 2014; Bodine et al. 2016b; Ryzhkov et al. 2005). This is true for woodboards, though the relationship between ρ_{hv} and size in other debris types depends on the scattering regime. This was seen with the rocks which had a sharp decrease of ρ_{hv} values with increasing size when transitioning between the Rayleigh and Mie scattering Regimes. The amount by which ρ_{hv} decreases with size also depends on the debris type, with woodboards experiencing the largest change and leaves experiencing much smaller changes in ρ_{hv} with increasing debris size. Thus, even though both debris types are in the Mie scattering regime, the woodboards still have lower ρ_{hv}. This difference in the change of ρ_{hv} is explained by the axis ratio results, which showed that debris with a lower axis ratio produced lower values of ρ_{hv}. This is because debris with lower axis ratios are more likely to have large variations in backscatter differential phase, similarly to larger debris (Bodine et al. 2014). This larger variation is what produces the lower values of ρ_{hv} seen in this study. Therefore, we generally note that larger debris tend to have lower ρ_{hv} than smaller debris. However, this is primarily true in a broad sense and many other factors affect ρ_{hv} such as debris composition and aspect ratio. This results is thus conditionally supported, as shown in Table 6.1.

Meanwhile, Z_H values for each debris type increases with increasing debris size. This makes since given the fact that the equation for Z_H (Equation 2.1) is directly proportional to the debris diameter to the 6th power. Since each debris type showed this increasing trend, this finding is strongly supported. Also, the range of values for

Z_H differs across debris types, with rocks having the lowest values and woodboards the highest.

It has also been hypothesized that, as debris concentration increases, ρ_{hv} will decrease and Z_H will increase (Bodine et al. 2014). This hypothesis is supported, but only over a limited range of debris concentrations where increasing diversity of debris orientations decreases ρ_{hv}. For each debris type, values of ρ_{hv} decreased with increasing debris concentration until about 1000 pieces of debris per resolution volume. For a resolution volume size of 10^6 m^3, anything more than 1000 pieces of debris merely saturates the signal, resulting in no change in ρ_{hv}. There is also more decrease in ρ_{hv} across debris concentration for larger debris pieces and a consistent increase in Z_H with increasing debris concentration regardless of the debris type.

Past studies have hypothesized that TDSs are related to tornado wind speeds since stronger winds should generate and loft more debris (Bodine et al. 2013; Wakimoto et al. 2020). To examine this in a controlled setting, SimRadar simulations were used to document the relationship between TDSs and 3D winds. These SimRadar simulations showed that 10$^\text{th}$ percentile ρ_{hv} decreases (increases) with increasing (decreasing) values of 99$^\text{th}$ percentile vertical velocity, horizontal wind magnitude, and vertical vorticity. This result is thus strongly supported since all debris types and both tornadogenesis simulations had a decreasing trend in ρ_{hv} with an intensifying tornado. That being said, there were differences across debris types, the two main distinctions being (1) the time at which ρ_{hv} began to decrease and (2) the range of ρ_{hv} values throughout the simulation. Heavier debris types like the woodboards took longer to be lofted to the same height as lighter debris types like the leaves and metal

sheets. This indicates that lighter debris is more sensitive to changes in W. Meanwhile, Z_H values were very similar across all debris types, meaning ρ_{hv} is the better discriminator between debris types. It should be noted that the background rain in SimRadar, which is similar to what is found in high precipitation supercells, could be contributing to the lack of change in Z_H across debris types. Finally, changes in ρ_{hv} are a good indicator of tornadic intensification and dissipation while Z_H only showed an increasing trend in very strong tornadoes and a decreasing trend in the dissipation case.

For all debris types, the TDS area increased (decreased) as the tornado intensified (weakened). For tornado dissipation, the TDS area became more variable for the heavier debris types (the woodboards). This is due to heavier debris falling out of the vortex faster, thus causing the area calculations performed at lower elevation angles to increase. This increase in the TDS area during tornado dissipation has also been seen in Bodine et al. (2013) and Houser et al. (2017). The TDS height was significantly higher for the stronger tornadogenesis case compared to the weaker tornadogenesis as shown by both the vertical cross-sections and the vertical profile of ρ_{hv} for both simulations. The TDS height also increased for all debris types as the tornado strengthened in both the weak and strong tornadogenesis simulations. The structure of the TDS was also very different in the stronger case compared to the weaker tornadogenesis case. While all three debris types in the weaker case showed a v-like shape indicative of centrifuging of debris with height, this was not seen in the stronger case. Rather, the TDS formed a dome-like shape with higher ρ_{hv} values in the bottom and center of the vortex and lower ρ_{hv} encasing these higher values,

similar to the debris overhang seen in Wakimoto et al. (2015). The difference in shape between the two tornadogenesis cases could be attributed to both the stronger updraft and the multiple vorticies present in the weaker case.

From this analysis done in this study, the change in 10th percentile ρ_{hv}, TDS height, and TDS area are all good indicators of tornado intensification. Values of Z_H only increase in the presence of a stronger vortex. However, low values of ρ_{hv} do not indicate the strength of the vortex as some debris types, such as leaves, can have very high values of ρ_{hv} even in the presence of a strong updraft. Thus, it is the change in ρ_{hv} that is indicative of TDS strength while the range of values reached can be indicative of the debris types that have been lofted. This is relevant for operational forecasters as the TDS response to a tornado's intensity will depend on what the tornado strikes. If there are no heavy or appreciable debris to loft in the region, there may not be a strong TDS signature on radar even though the tornadic winds are intense. Of course, the range of ρ_{hv} values are also dependent on the availability of debris types. For example, a tornado that passes through a wheat field could be very intense, but might not have a prominent TDS due to the lack of large debris that would lower the ρ_{hv} values. However, in reality there are often a wide range of debris sizes and types for the tornado to loft, so this caveat is more the exception than the norm.

While this project was able to confirm multiple past hypotheses about the TDS, there were some features this analysis was unable to explain. These are generally related to some of the smaller scale details of the TDS that may be related to more subtle or localized interactions between the tornado's flow and debris. For example,

99

it is unknown why in every simulation the TDS shifted to the south of the domain. Future analysis such as calculating and plotting debris trajectories and looking at the radial and tangential wind could provide insight into why this occurred. Also, when looking at the PPIs of the TDS at 2.5°, contours of the radial and tangential wind might be more insightful into why each TDS took on a different shape rather than the horizontal wind magnitude. Furthermore, since the stronger tornadogenesis case produced a much more complex debris structure, future analysis should include vertical data for all debris types rather than the just woodboards. This would provide extra information about the evolution of both the TDS height and structure across different debris types in the presence of a stronger updraft.

Finally, the simulations used in this study have their limitations. For example, the vortex is removed from the parent supercell, meaning there is no influence of storm-scale boundaries and flow on the TDS. Especially in the case of the structure of the TDS, this limits the "realness" of the data as, for example, past studies have found that debris ejection has been associated with storm-scale features such as the rear-flank gust front surges (Kurdzo et al. 2015; Houser et al. 2017). It follows that the next step in this project is to pair these simulations with observations of tornadoes using rapid-scan mobile radars such as RaXPoL to account for these other phenomena. The wind field data from mobile radars such as RaXPoL can also be used to run various LES simulations to model a real-life tornadogeneis case. Other work with upcoming mobile radars such as the Polarimetric Atmospheric Imaging Radar (PAIR) would also provide real-time volumetric data of the TDS, which would allow for the comparison of the vertical structure of the TDS across simulations and

observations. Using SimRadar with high-resolution, tornado-resolving simulations could also help answer questions about the storm-scale TDS signatures.

Bibliography

Bluestein, H. B., 2013: Chapter 6: Tornadoes. *Severe Convective Storms and Tornadoes*, Springer, 307 – 416.

Bluestein, H. B., M. M. French, R. L. Tanamachi, S. Frasier, K. Hardwick, F. Junyent, and A. Pazmany, 2007a: Close-range observations of tornadoes in supercells made with a dual-polarization, X-band, mobile Doppler radar. *Mon. Wea. Rev.*, **135**, 1522–1543.

Bluestein, H. B., C. C. Weiss, M. M. French, E. M. Holthaus, R. L. Tanamachi, S. Frasier, and A. L. Pazmany, 2007b: The structure of tornadoes near Attica, Kansas, on 12 May 2004: High-resolution mobile, Doppler radar observations. *Mon. Wea. Rev.*, **135**, 475–506.

Bodine, D., M. R. Kumjian, R. D. Palmer, P. L. Heinselman, and A. V. Ryzhkov, 2013: Tornado damage estimation using polarimetric radar. *Wea. Forecasting*, **28**, 139–158.

Bodine, D., M. R. Kumjian, A. J. Smith, R. D. Palmer, A. V. Ryzhkov, and P. L. Heinselman, 2011: High-resolution polarimetric observations of an EF-4 tornado on 10 May 2010 from OU-PRIME. *35th Conf. on Radar Meteorology*, 3B.4, Amer. Meteor. Soc.

Bodine, D. J., T. Maruyama, R. D. Palmer, C. J. Fulton, H. B. Bluestein, and D. C. Lewellen, 2016a: Sensitivity of tornado dynamics to debris loading. *J. Atmos. Sci.*, **73**, 2783 – 2801.

Bodine, D. J., R. D. Palmer, T. Maruyama, C. J. Fulton, Y. Zhu, and B. L. Cheong, 2016b: Simulated frequency dependence of radar observations of tornadoes. *J. Atmos. Oceanic Technol.*, **33 (9)**, 1825–1842, http://dx.doi.org/10.1175/JTECH-D-15-0120.1.

Bodine, D. J., R. D. Palmer, and G. Zhang, 2014: Dual-wavelength polarimetric radar analyses of tornadic debris signatures. *J. Appl. Meteor. Climatol.*, **53**, 242–261.

Bukovcic, P., D. Zrnic, and G. Zhang, 2017: Winter precipitation liquid–ice phase transitions revealed with polarimetric radar and 2dvd observations in central oklahoma. *J. Appl. Meteor.*, **56**, 1345 – 1363.

Cheong, B. L., D. J. Bodine, C. J. Fulton, S. M. Torres, T. Maruyama, and R. D. Palmer, 2017: SimRadar: A polarimetric radar time-series simulator for tornadic debris studies. *IEEE Trans. Geosci. Remote Sensi.*, **55**, 2858 – 2870.

Dowell, D. C., C. R. Alexander, J. M. Wurman, and L. J. Wicker, 2005: Centrifuging of hydrometeors and debris in tornadoes: Radar-reflectivity patterns and wind-measurement errors. *Mon. Wea. Rev.*, **133**, 1501–1524.

Griffin, C. B., D. J. Bodine, J. M. Kurdzo, A. Mahre, and R. D. Palmer, 2020: High-temporal resolution observations of the 27 May 2015 Canadian, Texas tornado using the Atmospheric Imaging Radar. *Mon. Wea. Rev.*, **147**, 873 – 891, doi:https://doi.org/10.1175/MWR-D-18-0297.1.

Griffin, C. B., D. J. Bodine, and R. D. Palmer, 2017: Kinematic and polarimetric radar observations of the 10 May 2010, Moore-Choctaw, Oklahoma tornadic debris signature. *Mon. Wea. Rev.*, **in press**.

Houser, J. L., H. B. Bluestein, and J. C. Snyder, 2017: A fine-scale radar examination of the tornadic debris signature and weak-echo reflectivity band associated with a large, violent tornado. *Mon. Wea. Rev.*, **144**, 4101 – 4130.

Kumjian, M., 2011: Precipitation properties of supercell hook echoes. *E. Journal Severe Storms Meteor.*, **6 (5)**.

Kumjian, M. R., 2013: Principles and applications of dual-polarization weather radar. Part I: Description of the polarimetric radar variables. *J. Operational Meteor.*, **1**, 226 – 242.

Kumjian, M. R., and A. V. Ryzhkov, 2008: Polarimetric signatures in supercell thunderstorms. *J. Appl. Meteor. Climatol.*, **48**, 1940–1961.

Kurdzo, J. M., D. J. Bodine, B. L. Cheong, and R. D. Palmer, 2015: High-temporal resolution polarimetric X-band Doppler radar observations of the 20 May 2013 Moore, Oklahoma tornado. *Mon. Wea. Rev.*, **143**, 2711 – 2735.

Lewellen, D. C., W. S. Lewellen, and J. Xia, 2000: The influence of a local swirl ratio on tornado intensification near the surface. *J. Atmos. Sci.*, **57**, 527–544.

Lewellen, W. S., 1976: Session 2: Theoretical Models of the Tornado Vortex. *Proceedings of the Symposium on Tornadoes: Assessment of Knowledge and Implications for Man*, R. E. Peterson, Ed., Texas Tech University, 107 – 143.

Magsig, M. A., and J. T. Snow, 1998: Long-distance debris transport by tornadic thunderstorms. Part I: The 7 May 1995 supercell thunderstorm. *Mon. Wea. Rev.*, **126**, 1430–1449.

Maruyama, T., 2011: Simulation of flying debris using a numerically generated tornado-like vortex. *J. Wind Eng. Ind. Aerodynamics*, **99**, 249–256.

Mischenko, M. I., 2000: Calculation of the amplitude matrix for a nonspherical particle in a fixed orientation. *Appl. Optics*, **39**, 1026–1031.

Mischenko, M. I., L. D. Travis, and D. W. Mackowski, 1996: T-matrix computations of light scattering by nonspherical particles: A review. *J. Quant. Spectrosc. Radiat. Transfer*, **55**, 535–575.

Palmer, R. D., and Coauthors, 2011: The 10 May 2010 tornado outbreak in central Oklahoma: Potential for new science with high-resolution polarimetric radar. *Bull. Amer. Meteor. Soc.*, **92**, 871–891.

Payne, C. D., T. J. Schuur, D. R. MacGorman, M. I. Biggerstaff, K. M. Kuhlman, and W. D. Rust, 2010: Polarimetric and electrical characteristics of a lightning ring in a supercell storm. *Mon. Wea. Rev.*, **138**, 2405–2425.

Rankine, W. J. M., and W. J. Miller, 1888: *A Manual of Applied Mechanics*. London: William John Macquorn Rankine, C. Griffin and Co.

Rotunno, R., 1979: A study in tornado-like vortex dynamics. *J. Atmos. Sci.*, **36**, 140–155.

Ryzhkov, A. V., T. J. Schuur, D. W. Burgess, and D. S. Zrnić, 2005: Polarimetric tornado detection. *J. Appl. Meteor.*, **44**, 557–570.

Schultz, C. J., and Coauthors, 2012a: Dual-polarization tornadic debris signatures Part I: Examples and utility in an operational setting. *Electronic J. Operational Meteor.*, **13**, 120 – 137.

Schultz, C. J., and Coauthors, 2012b: Dual-polarization tornadic debris signatures Part II: Comparisons and caveats. *Electronic J. Operational Meteor.*, **13**, 138–158.

Senior, T. B., K. Sarabandi, and F. T. Ulaby, 1987: Measuring and modeling the backscattering cross section of a leaf. *Radio Sci.*, **22**, 1109 – 1116.

Snyder, J. C., H. B. Bluestein, V. Venkatesh, and S. J. Frasier, 2013: Observations of polarimetric signatures in supercells by an X-band mobile Doppler radar. *Mon. Wea. Rev*, **141**, 3 – 29.

Snyder, J. C., H. B. Bluestein, G. Zhang, and S. J. Frasier, 2010: Attenuation correction and hydrometeor classification of high-resolution, X-band, dual-polarized mobile radar measurements in severe convective storms. *J. Atmos. Oceanic Technol.*, **27**, 1979–2001.

Tanamachi, R. L., H. B. Bluestein, J. B. Houser, S. J. Frasier, and K. M. Hardwick, 2012: Mobile X-band, polarimetric Doppler radar observations of the 4 May 2007 Greensburg, Kansas, tornadic supercell. *Mon. Wea. Rev.*, **140**, 2103–2125.

Ulaby, F. T., T. Bengal, J. East, M. C. Dobson, J. Garvin, and D. Evans, 1988: Chapter 4: Measured Data. *Microwave dielectric spectrum of rocks*, University of Michigan, 33.

Umeyama, A., B. L. Cheong, S. Torres, and D. Bodine, 2018: Orientation analysis of simulated tornadic debris. *J. Atmos. Ocean. Tech.*, **35**, 993 – 1010, doi: https://doi.org/10.1175/JTECH-D-17-0140.1.

Van Den Broeke, M. S., 2015: Polarimetric tornadic debris signature variability and debris fallout signatures. *J. Appl. Meteor. Climatol.*, **54**, 2389 – 2405.

Van Den Broeke, M. S., 2017: Polarimetric radar metrics related to tornado life cycles and intensity in supercell storms. *Mon. Wea. Rev.*, **145**, 3671 – 3686.

Van Den Broeke, M. S., and S. T. Jauernic, 2014: Spatial and temporal characteristics of polarimetric tornadic debris signatures. *J. Appl. Meteor. Climatol.*, **53 (10)**, 2217–2231.

Wakimoto, R. M., N. T. Atkins, K. M. Butler, H. B. Bluestein, K. Thiem, J. Snyder, and J. Houser, 2015: Photogrammetric analysis of the 2013 El Reno tornado combined with mobile X-band polarimetric radar data. *Mon. Wea. Rev.*, **143**, 2657 – 2683.

Wakimoto, R. M., Z. Wienhoff, H. B. Bluestein, and D. Reif, 2018: The Dodge City tornadoes on 24 May 2016: damage survey, photogrammetric analysis combined with mobile polarimetric radar data. *Mon. Wea. Rev.*, **146**, 3735–3771.

Wakimoto, R. M., Z. B. Wienhoff, H. B. Bluestein, D. J. Bodine, and J. M. Kurdzo, 2020: Mobile radar observations of the evolving debris field compared with a damage survey of the Shawnee, Oklahoma tornado of 19 May 2013. *Mon. Wea. Rev.*, **148**, 1779 – 1803, doi:10.1175/MWR-D-19-0215.1.

Wakimoto, R. M., and Coauthors, 2016: Aerial damage survey of the 2013 El Reno tornado combined with mobile radar data. *Mon. Wea. Rev.*, **144**, 1749 – 1776.

White, F. M., 1991: *Viscous Fluid Flow*. McGraw-Hill.